STUDIES ON GRANULATION, DRYING AND TRIBOCHARGING BEHAVIOUR OF PHARMACEUTICAL POWDERS IN A FLUIDIZED BED DRYER

A Thesis Submitted to the
College of Graduate and Postdoctoral Studies
In Partial Fulfillment of the Requirements
For the Degree of Doctor of Philosophy
In the Department of Chemical and Biological Engineering
University of Saskatchewan
Saskatoon

By

Chen Li

PERMISSION TO USE

In presenting this thesis/dissertation in partial fulfillment of the requirements for a Postgraduate degree from the University of Saskatchewan, I agree that the Libraries of this University may make it freely available for inspection. I further agree that permission for copying of this thesis/dissertation in any manner, in whole or in part, for scholarly purposes may be granted by the professor or professors who supervised my thesis/dissertation work or, in their absence, by the Head of the Department or the Dean of the College in which my thesis work was done. It is understood that any copying or publication or use of this thesis/dissertation or parts thereof for financial gain shall not be allowed without my written permission. It is also understood that due recognition shall be given to me and to the University of Saskatchewan in any scholarly use which may be made of any material in my thesis/dissertation.

Requests for permission to copy or to make other uses of materials in this thesis/dissertation in whole or part should be addressed to:

Head of the Department of Chemical and Biological Engineering
57 Campus Drive
University of Saskatchewan
Saskatoon, Saskatchewan S7N 5A9 Canada
OR
Dean
College of Graduate and Postdoctoral Studies
University of Saskatchewan
116 Thorvaldson Building, 110 Science Place
Saskatoon, Saskatchewan S7N 5C9 Canada

ABSTRACT

Wet granulation and drying are two crucial unit operations in the pharmaceutical industry. The two operations can be conducted in one piece of equipment, namely a fluidized bed. Fluidized beds have the advantages of excellent mixing, large contact area, and superior heat and mass transfer. Drying is typically operated at bubbling and turbulent regions. Despite the wide applications of fluidized beds in wet granulation and drying, there still remain challenges.

Observation and measuring the dynamic granulation process are challenging with conventional experimental methods due to the opaque nature of pharmaceutical powders and the complex interaction between powders and liquid taking place in a short period of time. In this study, the dynamic granulation process was, for the first time, captured with synchrotron-based X-ray imaging techniques. The dynamic interaction between the pharmaceutical powders and the liquid binder was captured by high-resolution X-ray images. Results show that pharmaceutical powder properties, including particle size, hydrophilicity, and morphology, have significant influences on the dynamic granulation process and the final granular product.

After wet granulation, the presence of high moisture content within pharmaceutical granules results in considerable cohesiveness. Agglomeration, channeling, defluidization, caused by the strong inter-particle forces, pose significant challenges to fluidization and drying, particularly at the beginning of the drying process. In this work, the drying performance of pharmaceutical granules was investigated in a pulsation-assisted fluidized bed dryer. It was found that pulsed airflow is effective in eliminating channeling and enhancing the drying rate at higher superficial gas velocity. Lower pulsation frequency is more favoured to improve the drying rate. Two typical drying stages were observed during the drying process, the constant rate period and the falling rate period. During the constant rate period, energy efficiency is between 60% to 45% for the drying process. The energy efficiency falls to 10% during the falling rate period. Nine thin-layer drying models were examined to predict the drying curve of the pharmaceutical granules. It was found that the Midilli and Kucuk model provided the best agreement between the experimental results

and the predicted values.

The pharmaceutical granules can be easily charged because of repeated collision and separation between particles and between particles and wall. The tribocharging behaviour of the pharmaceutical granules in a conventional FBD and a PFBD was investigated by varying operating conditions such as superficial gas velocity, inlet air temperature, pulsation frequency, and pulsed air ratio.

It was found that the specific charge of the pharmaceutical granules remained lower than 0.2 μC/kg during the constant rate period. When the moisture content was reduced to a critical moisture content, namely 10%, the specific charge increased sharply regardless of the superficial gas velocity and inlet air temperature. Then, the increase in the specific charge continued before it reached an equilibrium value during the falling rate period. The equilibrium specific charge is influenced by the superficial gas velocity and pulsation frequency. Higher superficial gas velocity and lower pulsed frequency resulted in a higher specific charge. When the superficial gas velocity is low, there is no noticeable difference between the conventional FBD and the PFBD at different pulsation frequencies. The inlet air temperature and pulsed air ratio did not show an impact on the equilibrium specific charge value.

ACKNOWLEDGMENTS

I would like to thank my family, my parents in particular, for their patience, dedication and emotional support. The unconditional love and encouragement accompanied me every single day in the past few years. What I received from them made all that I have received possible.

Professor Lifeng Zhang has continuously supported me during my Ph.D. research with his patience, motivation, enthusiasm, and immense knowledge. His insights, perseverance, guidance, and encouragement were a great source of success in the formulation of this thesis.

My sincere thanks also go to Dr. Kwangseok Choi from the National Institute of Occupational Safety and Health in Japan, Dr. Ning Zhu from Canadian Light Source, and Professor Heather N. Emady from Arizona State University for their guidance, support and advice. I am very grateful for all their assistance in this project.

Special thanks are also due to the technical staff at the Department of Chemical and Biological Engineering. Thanks to Richard Blondin, Kevin Carter, and RLee Prokopishyn for their helpful consultations and assistance in building the equipment.

I owe a great deal to my colleagues and friends, Paria Rahimian, Tolu Emiola-Sadiq, Shuang Liu, Ming Teng, Xianming Luo, Yuchen Si, Yingjie Yang, Carter Blocka, Yuzhou Zhang, who gave help and shared their experiences. Life is enjoyable with all of you during the past few years.

TABLE OF CONTENTS

LIST OF FIGURES

LIST OF TABLES

NOMENCLATURE

Notation	Description
ΔH_{vap}	Latent heat of water vaporization, 2260 kJ/kg
ΔM	Weight of water removed (g)
Δp	Peak pressure drop (kPa)
a	Coefficient in drying model
A	Cross-section area (m^2)
Bo_g	Bond number
Bo_g^*	Modified Bond number
c	Coefficient in drying model
C	Capillary constant
C_p	Specific heat capacity of air, 1.00 kJ/kg·K
d	Capillary tube diameter (m)
d_{50}	Cumulative 50% point of powder diameter (μm)
D_a	Projected area equivalent diameter (mm)
d_d	Droplet diameter (mm)
d_g	Granule diameter (mm)
D_{max}	Maximum final granule diameter (mm)
D_{min}	Minimum final granule diameter (mm)
ds	Surface mean diameter (μm)
e	Coefficient in drying model
f	Pulsation frequency (Hz)
g	Coefficient in drying model
g	Gravitational acceleration constant, 9.8 m/s^2
HAR	D_{max}/D_{min}
h_d	Droplet height (mm)

h_g	Granule height (mm)
H_g	Final granule height (mm)
i	Sample order
k	Coefficient in drying model
L	Capillary tube length (m)
m	Mass of sample (g)
M	Mass of moisture per unit weight (g/kg)
$\dot{m}$	Drying rate (g/kg/min)
$MR_{exp,i}$	Experimental moisture ratio
$MR_{pre,i}$	Predicted moisture ratio
n	Coefficient in drying model
N	Total number of samples
p	Average pressure drop (kPa)
q	Specific charge q (μC/kg)
Q	Total charge (μC)
r	Pulsed air ratio
RH	Relative humidity (%)
r_m	Overall movement ratio
t	Total drying time (min)
t’	Penetrating time (s)
T_{in}	Inlet gas temperature (°C)
T_{out}	Outlet gas temperature (°C)
U	Superficial gas velocity (m/s)
u_0'	Derivative of the liquid velocity at the capillary tube boundary (m/s)
U_{mf}	Minimum fluidizaiton velocity (m/s)

VAR	D_a/H_g
X	Moisture content of pharmaceutical granules (%)
X_0	Initial moisture content of pharmaceutical granules (%)

Greek letters

γ	Liquid surface tension (mN/m)
η	liquid viscosity (mPa·s)
η_e	Energy efficiency (%)
θ	Contact angle (°)
ρ	liquid density (g/cm^3)
ρ_{air}	Air density (g/cm^3)
ρ_{bed}	Particle bulk density (g/cm^3)
ρ_p	Particle skeletal density (g/cm^3)
σ	Standard deviation of pressure (kPa)

ABBREVIATIONS

Abbreviation	Meaning
APAP	Acetaminophen
API	Active pharmaceutical ingredients
BMIT	Biomedical Imaging and Therapy Facility
CCS	Croscarmellose sodium
CLS	Canadian Light Source
CT	Computed tomography
FBD	Fluidized bed dryer
FOV	Field of view
FPS	Frames per second
HAR	Horizontal aspect ratio
IBU	Ibuprofen
LMH	Lactose monohydrate
LMHF	Fine lactose monohydrate
MCC	Microcrystalline cellulose
MCCF	Fine microcrystalline cellulose
PFBD	Pulsed fluidized bed dryer
WCR	Washburn capillary rise

CHAPTER 1. INTRODUCTION

1.1 Project motivation and knowledge gap

Wet granulation and drying operations are two important unit operations in the pharmaceutical industry. Wet granulation aims to combine fine powders to form larger granules. Due to the complexity of the granulation process taking place in a short time, observing the interaction between liquid binders and solid and measuring the size and shape of the granules and droplets during this dynamic process are challenging with conventional experimental methods such as optical approaches and conventional CT techniques.

After granulation, the moisture needs to be removed. Fluidized bed drying has been extensively used due to its excellent mixing, large contact area, high heat and mass transfer rate. At the beginning of the drying process, the high moisture content and cohesive nature have a negative impact on the fluidization. The channeling phenomenon may occur. The air moves through the bed layer through channels. The granules around the channeling regions get over-dried while the granules in other areas are still wet. Increasing superficial gas velocity is commonly used to overcome the channeling. However, this method also results in excessive entrainment and high energy cost. Pulsed fluidized bed drying (PFBD) is a promising solution to eliminate channeling and to decrease energy cost. PFBD has successfully been applied in biomass and food processes. However, very limited efforts have been placed on the application of PFBD in the pharmaceutical industry. There is a dearth of knowledge about how important operating parameters, such as superficial gas velocity, air temperature, pulsation frequency, and pulsed air ratio, influence the drying behaviour and energy efficiency in pulsed fluidized bed dryers.

With a decrease in the moisture content, electrostatic charges start to accumulate quickly in pharmaceutical powders. In typical pharmaceutical manufacturing processes, repeated particle-particle and particle-wall contact, as well as the high volume resistivity of most pharmaceutical compounds, can result in adhesion, agglomeration, electrostatic discharge. The electrostatic discharge could even lead to explosion. Current studies on the tribocharging phenomenon are quite limited, and most studies have been conducted on a dry basis with an individual component. In actual pharmaceutical production, the granules usually contain a noticeable amount of active pharmaceutical ingredients (APIs). Therefore, an advanced understanding of the tribocharging phenomenon in fluidized bed drying of pharmaceutical granules containing APIs is still needed, particularly when pulsed airflow is added.

1.2 Objectives

Based on the knowledge gaps identified above, the objectives of this project were to:

1. Employ synchrotron-based X-ray imaging techniques to understand the dynamic granulation processes of pharmaceutical powders and explore the internal structure and final granules;
2. Investigate effects of operating parameters, including pulsed flow at pulsation frequency (1.5, 3.0, 6.0 Hz), superficial gas velocity (1.0, 1.4, 1.8 m/s), inlet gas temperature (40, 50, 60 ℃), and pulsed air ratio (0, 10%, 20%, 30%, 40%, 50%,) on the drying performance;
3. Study the effects of important operating parameters on the energy efficiency of a PFBD and conventional FBD; and
4. Investigate the tribocharging behaviour of pharmaceutical granules during the fluidized bed drying process.

1.3 Hypothesis

Based on the objectives and literature review, the hypotheses are:

1. Synchrotron-based X-ray radiographic imaging techniques will enable the visualization of the dynamic wet granulation process due to high temporal and spatial resolutions;

2. Pulsed airflow will decrease the drying time and increase the drying rate compared with continuous airflow; Lower pulsation frequency, higher superficial gas velocity, higher inlet air temperature, and higher pulsed air ratio can eliminate channeling and increasing the drying rate;

3. A PFBD has higher energy efficiency than a conventional FBD;

4. The pharmaceutical granules are more likely to gain more charge in a PFBD than a conventional FBD due to the added pulsation.

1.4 Thesis organization

This study focuses on the two crucial processes during the pharmaceutical tablet manufacturing process: wet granulation and fluidized bed drying. Chapter 1 of this thesis is the introduction, which includes project motivation, knowledge gaps, objectives, and hypotheses.

Chapter 2 provides an overview of current studies on three topics relevant to this thesis, including wet granulation in the pharmaceutical industry, fluidized bed drying, and tribocharging behaviour of powders. This chapter discusses the progress of these three areas and reveals the novelty of this study.

Chapter 3 discusses the characterization of the internal structure and morphology of the pharmaceutical granules using optical camera and synchrotron-based X-ray computed tomography (CT) techniques. This chapter provides a good understanding of the final granules after wet granulation and shows great promise of using synchrotron X-ray computed tomography techniques to study micro-scale to milli-scale granules with high resolution.

Chapter 4 describes using in-situ synchrotron X-ray computed tomography (CT) techniques to visualize the dynamic wet granulation process. The effects of wet granulation operating parameters, including liquid binder type, release height of liquid binder droplet, liquid droplet volume, and particle size, have been discussed.

After the wet granulation operation, the moisture within the granules needs to be removed. Chapters 5 and 6 explore the drying and tribocharging behaviour of pharmaceutical granules in a pulsation-assisted fluidized bed dryer. The effects of operating conditions, such as superficial gas velocity, inlet air temperature, pulsation frequency, and pulsed air ratio, have been explored. The drying models and energy efficiency have been studied in these two chapters.

Chapters 7 and 8 summarize the research results obtained from this thesis and present conclusions and recommendations for future work. The Appendix includes the images of the dynamic granulation process of individual components, minimum fluidization velocity measurements and work function measurement.

CHAPTER 2. LITERATURE REVIEW

2.1 Wet granulation in the pharmaceutical industry

2.1.1 Wet granulation

Granulation is an important unit operation in chemical and pharmaceutical industries [1]. Fine particles usually pose great difficulties on unit operations due to the strong inter-particle force, cohesive nature, low flowability, and entrainment. Granulation operation allows for agglomeration of fine particles into larger granules with desired properties, such as mechanical strength, porosity, flowability, bulk density, and particle size distribution. The granulation operation also enables easier material handling, uniformity of APIs and excipients, controlled disintegration, and dissolution profiles [2, 3].

Based on binders used to form agglomerates, there are three types of granulation techniques: wet granulation, dry granulation, and direct compression. Compared with the other two alternatives, wet granulation has the advantages of low equipment cost, better control of drug content uniformity at low drug concentrations, more desired product bulk density and compactibility [4, 5]. Unlike wet granulation, the solid binder is used during dry granulation. Dry granulation is more desirable when handling moisture-sensitive and heat-sensitive pharmaceutical materials as it is free from liquid binder solvents, and no subsequent drying operation is needed [6]. Direct compression has a high requirement for flowability and cohesiveness, which limits its wide applications [7].

During the wet granulation process, wetting and nucleation, consolidation and growth, and breakage and attrition are the main processes that produce granules. The wetting and nucleation process usually finishes within a few seconds. The liquid binder droplet is brought in contact with a dry powder bed and distributed through the bed to form nuclei granules. Consolidation and growth are the periods where collisions between two granules, granules and feed powder, or a granule and the equipment lead to granule compaction and growth. Attrition and breakage are when granules break due to continuous impact, wear, or compaction [8].

There are many types of granulators, such as fluidized bed granulators, low-shear granulators, high shear granulators, and extruders. The granulators can also be classified based on the operation modes, including batch and continuous operation. Fluidized beds and high shear mixers are the two main types of wet granulation equipment. The main difference between the two techniques is the solid agitation mode and granule growth. A high-shear granulator can only be operated in a batch mode. Fluidized bed granulation can be operated in both batch and continuous modes. The batch operation can be monitored with a conventional off-line instrument. The continuous operation requires online control and testing systems, thereby more initial investment needed. However, continuous operation mode usually has the advantages of high production efficiency, low operation cost, high production capability, and stable product quality [9].

During high-shear granulation, the powders are kept agitated with an impeller sealed in a vessel. A liquid binder is sprayed from the top of the granulator. Liquid bridges combine fine powders together to form nuclei when the liquid binder contacts the powers. The agitation with high-shear force, continuous mixing, and spraying densify the nuclei and surrounded powders to form larger granules [10].

During the fluidized bed granulation process, the liquid binder solution is sprayed from the top of the freeboard. Air is injected from the bottom of the powder bed. Granules form when the liquid binder droplet impacts the bed surface [11].

The variables affecting wet granulation can be classified into two categories, namely, material parameters and granulation conditions. The critical material parameters include particle size, particle size distribution, the contact angle between the powder and liquid binder, solid solubility, swelling ratio of the powder in the liquid binder, and liquid binder concentration and liquid binder viscosity [12-14]. For the high-shear mixer granulation, the important operation conditions are mixing generation level, process time, fill level, liquid spray rate, and operating temperature [11]. For the fluidized bed granulation, the important operating conditions include spray droplet size, spraying surface and rate, the quantity of solvent, air flow rate, inlet air temperature and relative humidity (RH), equilibrium temperature, and process time [4].

2.1.2 Wet granulation process characterization techniques

The visualization of the dynamic wet granulation can be used to study the granulation mechanism and the end point of wet granulation. Various online testing techniques have been applied and their advantages and disadvantages are discussed below.

High-speed cameras were employed to observe the dynamic process [15, 16]. The main limitation of this method is the failure to investigate the internal interaction beneath the bed surface and the low image resolution. Capacitance sensor and electrical capacitance tomography (ECT) can measure the changes in moisture content and pharmaceutical material bulk density by monitoring the electrical current during wet granulation. The main advantage of the ECT technique is the non-invasive nature, while the disadvantage is the low resolution and complexity of electrode installation, especially for three-dimensional (3D) image capture [5, 17]. Microwave measurement can only be used to monitor the initial moisture content. The changes in bulk density during granulation and temperature have significant impacts on the sensitivity. Near-infrared (NIR) spectroscopy technique can be used to monitor moisture content, but it requires extensive calibration and a stable operating environment. Raman spectroscopy can be used to identify components in granules. However, most of these techniques discussed above can only monitor macroscale parameters, such as moisture content and density.

The opaque nature and the complex interaction between powder and liquid occurring in a short time and micro-scale area make experimental studies challenging. X-ray imaging and high-speed camera techniques are the two main experimental methods that have been used to investigate the granulation process [18, 19]. However, the dynamic granulation process happening in a short period cannot be captured by lab-based X-ray imaging techniques due to the low photon flux generated from conventional X-ray sources. High-speed cameras are mostly applied to capture images from the top view [20].

2.2 Fluidized bed drying

2.2.1 Fluidized bed drying process

Fluidization is the fluid-like status of solid particles when fluid moves through a static bed of solid particles. Two-phase fluidization can be classified into liquid-solid and gas-solid fluidization based on the fluid used. In fluidized beds, flow regimes can be classified into fixed bed, bubbling bed, turbulent bed, fast bed, and pneumatic conveying with increasing the superficial gas velocity. Based on the fluidization characteristics and material properties, particles are classified into four groups: Geldart Groups aeratable (A), sand-like (B), cohesive (C), and spoutable (D) particles [21]. The selection of the operating regime is based on the particle properties and product requirements. Concerning the application of fluidized beds in pharmaceutical powder drying, it requires a large heat transfer area, enough gas-solid contacting time to remove bound water, and proper methods to control the granule size.

The fluidized bed dryers can be operated in four different modes: batch drying, totally mixed drying, plug flow drying, and two-stage flow drying. The capacities of fluidized bed dryers in the pharmaceutical industry are ranging from 400 g to 1200 kg [22]. The drying process takes 20 to 40 minutes for large batch operation.

Advantages of using fluidized beds to dry pharmaceutical tablets production are as follows:

1. Short drying time and minimized heat challenge to thermal-sensitive materials [23].

2. The fluidized state of the bed ensures that drying occurs from the surface of all the individual particles. Hence, most of the drying processes have a constant drying rate [24].

3. Uniform temperature distribution in the fluidized bed as a result of good mixing. Thus, the temperature can be controlled precisely [25].

4. The turbulence in a fluidized bed causes some attrition to the surface of the granule. This produces a more spherical free-flowing product [26].

5. The free movement of individual particles reduces the risk of soluble materials migrating during drying [27].

6. Keeping the granules separated during drying also eliminates the problems of aggregation [28].

7. The fluidized granules can be mobile, making handling and movement around the production area simple, thus reducing labour costs [29].

8. Shorter drying time mean that the unit has a high production output from a small floor space.

Some disadvantages of fluidized bed drying are as follows:

1. The turbulence of a fluidized state may cause excessive attrition of some materials, with damage to some granules and the production of excessive dust [30].

2. Fine particles may become entrained in the fluidizing air and must be collected by bag filters [31].

3. The vigorous movement of particles in hot and dry air can lead to the generation of tribocharging. Precaution must be taken. A mixture of air with fine organic materials such as starch and lactose can explode if ignited by sparking caused by static charges. The explosion risks are further increased if the fluidized material contains a volatile solvent. Adequate electrical earthing is essential [22].

It is hard to fluidize the particles with wide particle size distributions, low particle strength, high stickiness, thermoplasticity, or high moisture content. Common methods to assist fluidization include vibration, pulsation, and soundwave [32].

2.2.2 Effect of operating parameters on fluidized bed drying

The drying air velocity has dominant effects on removing unbound water. One previous study from our group [33] shows that an increase in the drying air velocity decreases the drying time. However, increasing the air velocity does not show any impact on the equilibrium moisture content. Higher air velocity improves the rate to remove unbound water at the initial constant drying period. When removing bound water, increasing the gas velocity has no significant effect. This probably is because the high internal water transfer resistance controls the drying rate [34].

The drying air temperature also has an impact on the drying process. The research conducted by Milad Taghavivand [33] shows that when increasing the air temperature, the drying rate increased significantly. When air temperature increased from 38 °C to 75 °C, the drying time was reduced from 120 minutes to 60 minutes to reach the same moisture content of 0.2. The higher temperature of drying air changes the equilibrium moisture content and results in a higher moisture diffusion rate [35].

For materials with a high content of unbound water, most unbound water will be removed at the distributing area. Thus, the drying rate does not change when increasing the bed height beyond a particular value (such as 0.5 m in pharmaceutical granule drying) [36]. For materials with a high content of bound water or low mobility, increasing the bed height decreases the drying rate [36].

2.2.3 Fluidized bed drying models

Fluidized bed drying is a complex process involving multiphase flow, phase change, heat, and mass transfer. Therefore, the mathematical description of fluidized bed drying becomes difficult. This process may also be coupled with physical and chemical changes. Researchers have placed great efforts to link drying experimental results with mathematical models to predict the drying process in fluidized beds. Different modeling approaches can be classified into computational fluid dynamics (CFD) models [37, 38], two-phases models [39, 40], and semi-theoretical models [41, 42].

The CFD modelling approach applies momentum equations, constitutive relations and closure laws to have detailed information of the fields in the fluidized bed dryer. The CFD models can help to explore the details of process information such as temperature, velocity, and moisture content distribution in the dryer [37]. However, it is time-consuming to get an explicit solution, and the uncertainty of parameters in closure relations limits the application of this method.

The two-phase models simplify the gas and particles into emulsion and bubble phases. Semi-empirical relations were used to describe gas and solid flow instead of solving the momentum equation. The solid and gas concentration and temperature distribution can be calculated. The two-phase model approach is a compromise of precision and numerical complication, which can be used for engineering scale-up and industrial-scale applications. The main disadvantage of this method is that the flow pattern is assumed, which might constrain its applications.

The semi-theoretical models are important tools in mathematical modelling fluidized bed drying processes. Most semi-theoretical models simplify the particle as a thin layer, and the prediction can give practical and sufficiently good results. When particles are assumed as one thin layer of slices, the temperature distribution can be assumed as uniform. The main advantage of thin layer models is their ease of use and less computational effort required than CFD and two-phase models. The thin layer models can be roughly classified into two major categories. One is derived from the Fick's second law of diffusion. The other category is established from the Newton's law of cooling.

2.3 Tribocharging behaviour of powders in fluidized beds

The electrostatic phenomenon in fluidized beds was first studied as early as the 1940s when researchers reported the adhesion of particles to vessel walls [43]. Electrostatic charges are generated due to repeated contacts and separation between particles and particle-wall. The electrostatic phenomenon can cause problems such as particle-wall cohesion, particle agglomeration, electrostatic discharge, and even explosion. Particles adhered to the column wall need to be cleaned frequently. Otherwise, the particle layer on the wall can interfere with sample ports and the measurement instruments. The heat and mass transfer rate between the particle and wall can also be negatively affected. The particles with the opposite charge have the tendency to form inter-particle agglomerates. The agglomerates change the particle size distribution and fluidization conditions. Most organic particles become readily charged when even handled and processed in metallic and grounded equipment [44]. The electrostatic discharge is caused by the ionization of the surrounding air when the electrostatic field builds up. The discharge channel at hot plasma status can ignite the flammable dust.

When the voltage is high enough to overcome the resistance caused by air, discharge occurs, which may lead to electrical shock to operating personnel, negatively influencing sensors and instrumentation, low product quality, fire, and even explosions. It has been reported that about one dust explosion occurs each day in Germany, and every tenth explosion is caused by static electricity [44]. According to Japanese statistics, electrostatic discharge caused around 70% of 153 accidents from 1961 to 2011 in the Japanese industry [43]. Therefore, it is important to eliminate electrostatic charge build-up.

Materials are typically neutral in natural status [45]. Based on the electron transfer mechanism, when two different solid materials physically contact each other, the electron transfer occurs, leading to differently charged materials. It is usually believed that the contact between particles and particle-wall contact causes the electrostatic phenomenon in fluidized beds [46]. The contact electrostatic charging mechanism is not fully understood [47]. The main explanations are the surface energy difference and Fermi level difference between the contacting particles [43, 48-50]. Cross reported that charge of particles with medium resistivity, namely 10^{12} Ωm, during sieving operation is within 10^{-3}-10^{-5} μC/kg, during pouring operation is within 10^{-1}-10^{-3} μC/kg, during grinding operation is within 1-10^{-1} μC/kg, during micronizing operation is within 10^{2}-10^{-1} μC/kg [43].

The charge generation mechanisms during solid powder processing within fluidized beds are complex, which include triboelectrification, frictional charging, thermionic emission, and ion collection. Triboelectrification is also known as tribocharging. The rubbing between materials generates charge transfer. The frictional charging is caused by the friction among gas, particles, and column walls. When the particles are exposed to a high temperature ($T > 1000$ K), the emission of electrons emission occurs [51, 52].

Although the statistic charge phenomenon has been reported for decades, experimental methods to study this phenomenon are still very limited. The experimental methods include two types, namely Faraday cups and electrostatic probes. The Faraday cup can be employed to measure the accumulated average net charge of particles based on electrostatic induction. In general, a

Faraday cup consists of two insulated coaxial concentric vessels, as shown in Figure 2.1. The modified Faraday cup technique can be installed to measure the electrostatic charge inside fluidized beds directly [53-55]. However, when employing Faraday cups, an additional charge may be introduced. The Faraday cup set-up also disturbs the internal flow [56].

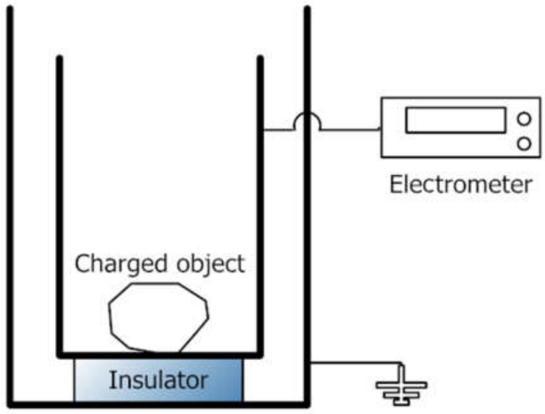

Figure 2. 1 Faraday cup.

Electrostatics probes also can be used to measure the voltage or current online in the fluidized bed [57-61]. Based on the measuring mechanism, electrostatics probes can be divided into three types: triboelectric sensor, electrodynamic sensor, and electrostatic sensor [62-64].

CHAPTER 3. CHARACTERIZATION OF INTERNAL STRUCTURE AND MORPHOLOGY OF THE PHARMACEUTICAL GRANULES

The content of this chapter has been published in International Journal of Pharmaceutics. 2019; 572. https://doi.org/10.1016/j.ijpharm.2019.118797

Contribution of the Ph.D. student:

The granulation experiments were designed and performed by Chen Li. Lifeng Zhang supervised and provided consultation during the experiment preparation, conduction, data analyzing, image reconstruction, and thesis preparation. Ning Zhu and Heather N. Emady offered technical support during experiment design, set-up construction, and image reconstruction. The writing of the manuscript was done by Chen Li, with Lifeng Zhang providing editorial guidance.

Contribution of this chapter to the overall study

This chapter provides a good understanding of the critical physical properties of the pharmaceutical powders used in the overall study. The internal structure of the pharmaceutical granule was studied with synchrotron-based X-ray computed tomographic techniques. The final granule size and morphology were analyzed with the optical method. These findings are of great importance to understand the fluidization and drying performance of pharmaceutical granules containing APIs.

3.1 Abstract

Wet granulation of powders is a crucial unit operation in the pharmaceutical industry. Due to the complexity of the granulation process taking place in a short time, observing and measuring the internal structure is challenging with conventional experimental methods. In this study, synchrotron-based X-ray imaging techniques were employed to study the international structure with a single drop impacting method in pharmaceutical powder beds. The final granule size and

morphology were studied with five common pharmaceutical excipients, two active pharmaceutical ingredients (APIs) and their mixtures. The internal structure of the granule structure was observed with high-resolution X-ray images. Results show that powders with higher hydrophilicity (smaller contact angle) are more likely to form granules with lower sphericity (plate-shaped), and lower hydrophilicity (higher contact angle) will result in more spherical granules. The porosity of the granule decreases from the top part to the bottom part of the granule.

3.2 Introduction

Wet granulation is an important unit operation in the chemical and pharmaceutical industries. During the wet granulation process, wetting and nucleation, consolidation and growth, and breakage and attrition are the main processes to produce granules. Wetting and nucleation is the stage where the liquid binder contacts with a dry powder bed, and nuclei granules form as liquid distribute through the bed layer. Consolidation and growth are defined as the stage of granules compaction and growth due to the collision between two granules, granules and feed powder, or a granule and the equipment. Breakage and attrition are the stage where the granules break due to impact, wear and compaction during granule product handling [65].

Liquid droplets wet fine powders to form granules in wet granulation. The wetting and nucleation process usually finishes within a few seconds. Key factors influencing granule formation are drop penetration time, dimensionless spray flux, Bond number, and Stokes deformation number [20]. Recent research efforts have been placed on the wetting and nucleation regime of single droplet granulation, which can enhance the control of preferred granule properties [66]. Granule properties such as granule size and size distribution have attracted the most attention. However, other important parameters, including granule shape internal structure and porosity, are rarely investigated since these parameters are difficult to measure [67]. Visualization of the final granule product is important to understand the granulation mechanisms, which is still challenging [20, 68, 69]. The typical size of pharmaceutical granules for tablet manufacturing ranges between 0.1 and 0.2 mm [70]. Thus, the resolution of the images obtained should be high enough to capture the details of the granule. Commercial medical X-ray tomography systems have low spatial resolutions at the sub-millimetre level. Therefore, an instrument with several orders of improvement in resolution with high image capture speed is needed to observe the microstructure of granule materials. Typical image acquisition time in walk-in cabinet systems with a 16-bit flat-panel detector is from a few hundred milliseconds (ms) to up to several seconds (s) per image [71]. For moving objects, lab-based computed tomography can capture high resolution images at extremely low speeds because of their relatively low photon flux.

In recent years, synchrotron-based X-ray imaging techniques have been employed in granulation studies: Yamada et al. [72] developed a quantitative synchrotron X-ray powder diffraction method. Small amounts of crystalline drug substances in pharmaceutical tablets (a limit of detection of 0.02% for fenoprofen calcium dehydrate) can be detected by analyzing the intensity of the diffracted X-ray; Noguchi et al. [73] investigated internal structures of fine granules using synchrotron-based X-ray micro-CT, where tomographic reconstruction images were 1920 × 1920 pixel with each pixel equivalent to 0.444 m × 0.444 m; Liu et al. [74] applied synchrotron-based X-ray micro-CT to study the mixing and segregation of binary pharmaceutical granules, and Buléon et al. [75] observed crystalline ultra-structures of starch granules with synchrotron-based X-ray micro-CT. However, most of these studies focused on the final granulation products that have a low resolution. The high energy flux of the synchrotron-based X-ray radiographic imaging techniques makes it possible to capture the details of the granules. Therefore, the objective of this study was to employ synchrotron-based X-ray radiographic imaging techniques to understand the internal structure of the granules.

3.3 Materials and methods

3.3.1 Materials characterization

The formulations of the pharmaceutical powder mixtures are given in Tables 3.1 and 3.2. The pharmaceutical powders were sieved through a 2.00 mm sieve. Each powder mixture was well mixed with an Inversina mixer (Bioengineering, Wald, Switzerland) at speed level 3 for 5 min.

Then the powders were loaded into sample vessels with a height of 3.5 cm and an inner diameter of 1 cm, with a powder bed height of 3 cm.

Microcrystalline cellulose (MCC) and Croscarmellose sodium (CCS) were provided by FMC BioPolymers. Lactose monohydrate (LMH) was ordered from Foremost Farms. Acetaminophen (APAP) and Ibuprofen (IBU) were purchased from Hebei Jiheng Pharmaceutical and Lichun Biological, respectively. The contact angles with water for formulation 1 with 20% APAP and Formulation 2 with 20% IBU are 71.6±1.0° and 68.3±7.2°, respectively.

Table 3.1 Mass percentage of pharmaceutical powders in formulation 1

Component	Function	Percentage by mass (dry basis)
APAP	API	0-20%
LMH	Filler	41-49%
MCC	Filler	37-43%
CCS	Disintegrant	2%

Table 3.2 Mass percentage of pharmaceutical powders in formulation 2

Component	Function	Percentage by mass (dry basis)
IBU	API	0-20%
LMH	Filler	41-49%
MCC	Filler	37-43%
CCS	Disintegrant	2%

The median particle size and surface mean diameter were measured with a Malvern 2000 Mastersizer S (Malvern Instruments, UK). Particle skeletal density was obtained by an Ultrapycnometer 1000 (Quantachrome Instruments, Austria)

Deionized water was used as the liquid binder. The surface tension of deionized water is 72.0 mN/m [76], and the viscosity is 0.89 mPa·s [77]. The contact angle of the pharmaceutical powders with water was measured with the Washburn capillary rise (WCR) method [78]. The WCR equation is given as follows:

$$\theta = \cos^{-1}\left(\frac{2\eta}{C\rho^2\gamma} \times \frac{\mathrm{d}m^2}{\mathrm{d}t'}\right) \tag{3.1}$$

where η is the liquid viscosity, γ is the liquid surface tension, ρ is the liquid density, C is the capillary constant, m is the mass of the liquid penetrating the packed powders, and t' is the penetrating time. A glass tube with a height of 6 cm and an inner diameter of 1 cm was packed with pharmaceutical powders to a height of 5 cm, with the top open to the atmosphere. The WCR setup is shown in Figure 3.1. The powders were loaded into the glass tube with a straw, and then the tube was sufficiently tapped to ensure no bubbles were present in the packed powders. The bottom of the glass tube was plugged with a fabric membrane, which allowed the liquid to move into the packed powders and prevented the powders from leaking into the liquid. Then test liquid was injected slowly into a petri-dish until the top of the liquid surface just touched the bottom of the tube. The mass gain of the powder bed equals mass loss of liquid in the container. The mass gain of the powder bed and the contacting time were recorded using a digital camera (Nikon 1 J1, Nikon, Japan) and a balance (ME4002TE, Mettler Toledo, USA). The contact angle of hexane with solid particles is 90°, so hexane was used as the test liquid to determine the capillary constant, C. Then, deionized water was used to determine the contact angle.

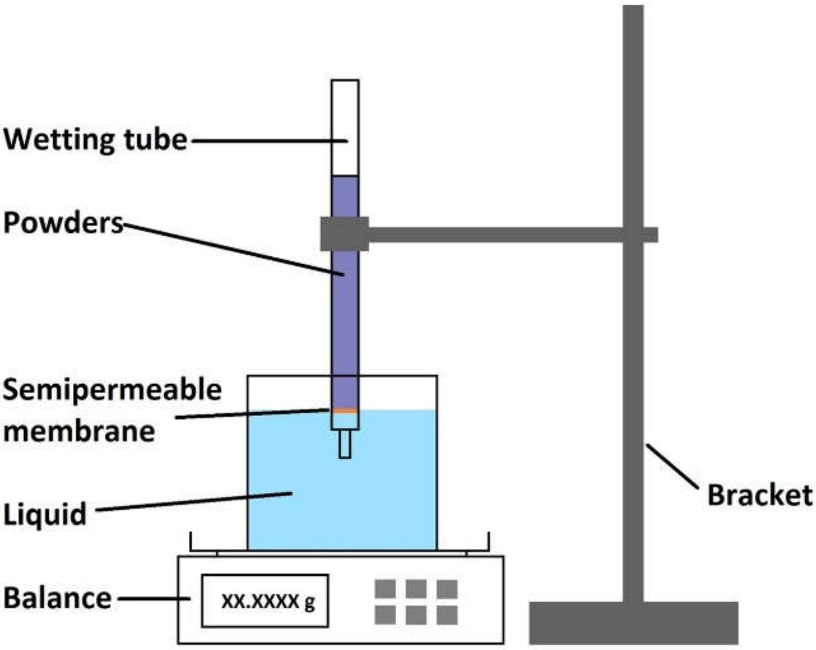

Figure 3.1 Washburn capillary rise experimental setup.

Two formulations were investigated with two different APIs (acetaminophen and ibuprofen). A modified particle Bond number is calculated, as shown in Table 3.3, based on the following equation to describe the liquid-particle interaction [79].

$$Bo_g^* = \frac{\gamma \cos\theta}{d_s^2 \rho_{bed} g} \tag{3.2}$$

where γ is the liquid surface tension, θ is the powder-liquid contact angle, d_s is the surface mean particle diameter, ρ_{bed} is the particle bulk density, and g is the gravitational acceleration constant. Emady et al. [79] used apparent particle density to calculate Bo_g^*, but the particle bulk density is used to replace apparent particle density. This results in larger Bo_g^*'s.

Using bulk particle density to modify the Bond number can measure the influence of powder bed packing on the granulation process, whereas the apparent particle density cannot. Compared with tightly packed powder beds, when using loosely packed powder beds, the bulk particle density will decrease, and the modified Bond number will increase. Thus, the liquid-solid interfacial area will increase. The liquid-solid interaction will be stronger due to larger capillary forces, where powders are more likely to attach to the droplet's surface. The granulation is a function of bed porosity, Bond number, and droplet release height. The droplet release height in this study is set at 2.5 cm, much lower than the boundary between the crater formation and spreading mechanism (15 cm). Here, the powder bed is in a static rather than fluidized state. Thus, only two granulation mechanisms may occur in this study, namely spreading or tunneling. However, Bo_g^*'s of the pharmaceutical powders used in this study are within the range of 16.8 to 493.8 and are thus all in the spreading regime [79], which is far from the boundary between the spreading and tunneling regimes (Bo_g^*=65,000). Thus, using particle bulk density does not have a significant influence on Bo_g^* and the corresponding granule formation regime in this study.

3.3.2 Synchrotron X-ray computed tomography setup

The experiments were conducted at the 05B1-1 beamline Biomedical Imaging and Therapy Facility (BMIT) at the Canadian Light Source (CLS), which is a 2.9 GeV third-generation synchrotron. A white beam (polychromatic beam) was used for imaging water droplet dynamics, and the position of the beam is shown in Figure 3.2.

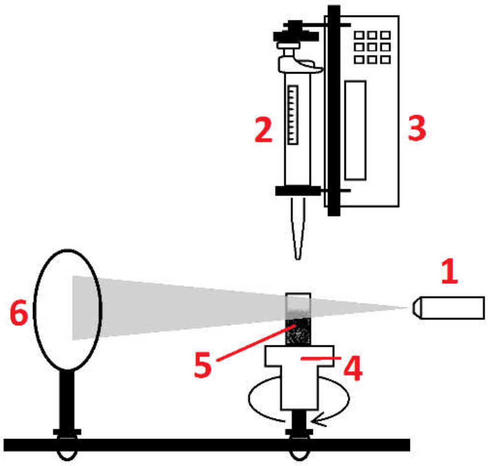

Figure 3.2 Single drop experimental setup: 1) beam source, 2) micropipettor, 3) syringe pump, 4) high precision motorized rotation stage, 5) sample vessel, and 6) beam camera.

Samples were placed at 25 m from the light source with 50 cm of the sample-to-detector distance. The images obtained from the BMIT include both X-ray absorption contrast and phase contrast. The projected images were captured by a beam monitor AA-40 (10 µm GSO scintillator, Hamamatsu, Japan) and a camera (Hamamatsu ORCA Flash 4.0, Japan). The field of the window was 6.66 x 4.50 mm^2 with an effective pixel size of 6.5 µm. Raw image sequences were composed of 16-bit images. Flat field and dark field images were collected for each scan, and the backgrounds were corrected utilizing ImageJ software [80]. To observe the details beneath the bed surface, the last image before the droplet moved into the window was subtracted from all of the following raw image sequences. The exposure time of each image was 20 ms. The scanning interval, defined as the interval between the start of the first image and the start of the following image, was 25 ms.

3.3.3 Granule morphology

An example of final granule shape measurements is illustrated in Figure 3.3. For the final granules, the projected area equivalent diameter (D_a), projected area maximum diameter (D_{max}), projected area minimum diameter (D_{min}) and projected area equivalent height (H_g) were used to describe size. The yellow outline in Figure 3a shows the projected area of the granule, which can be obtained by binarization processing in ImageJ. Then the projected area equivalent diameter (D_a) can be calculated based on this projected area. The horizontal aspect ratio ($HAR=D_{max}/D_{min}$) and vertical aspect ratio ($VAR=D_a/H_g$) were employed to characterize the shape

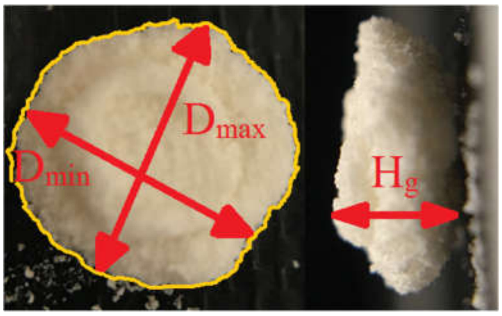

(a) (b)

Figure 3.3 Illustration of granule morphology measurements: (a) top view and (b) side view of the resultant granule.

The internal structure of the final granule was visualized by using a synchrotron-based X-ray CT scan system at the Canadian Light Source BMIT line. As shown in Figure 3. 2, the sample was seated on a high precision motorized rotation stage. The sample was rotated 180° to collect projected images. Afterwards, the projected images were reconstructed to form slices with ImageJ software. Contrast enhancement and a despeckle filter were applied to remove noise signals. Thresholds were set to form binary images for porosity calculation. Avizo (Version 9.5, Thermo Fisher Scientific) was applied for 3D visualization.

3.3.4 Single drop granulation setup

Single drop granulation experiments were conducted to investigate liquid drop impact with powder beds consisting of pharmaceutical ingredients. The powder bed was levelled with a metal panel to ensure a smooth surface. The setup is shown in Figure 3.2. A micropipette, filled with deionized water as the liquid binder, was held 2.5 cm above the powder bed surface. The resulting impact velocity of the droplet was about 0.7 m/s. The powders were placed in a small cylindrical vessel with an inner diameter of 1 cm and a height of 3 cm. A syringe pump was used to control the release of liquid droplets. In this work, droplets with a volume of 15 µL were investigated.

3.3.5 Uncertainty analysis

The contact angle measurement using the Washburn capillary rise method was repeated three times. The standard deviations of the contact angle were within 8.3%. The granules morphology measurement was repeated three times. The standard deviation of the maximum final granule diameter, D_{max}, is within 5.4%. The standard deviation of the minimum final granule diameter, D_{min}, is within 8.3%, and that of the projected area equivalent diameter H_g is 7.4%. That of the final granule height, D_a, is within 3.2%.

3.4 Results and discussion

3.4.1 Physical properties and contact angles of pharmaceutical powders

The characterization of the powder materials, including median particle size, surface mean diameter, contact angle with water, particle skeletal density, and modified particle Bond number, used in this study is presented in Table 3.3. IBU has the largest particle size (195 µm), and CCS has the smallest particle size (41 µm) among the powders used in this research. Wettability is an important property to measure the interaction between powder and liquid during granulation and is quantified via the contact angle. The contact angles of all the powders are smaller than 90°, which means they are all hydrophilic.

Table 3.3 Particle size and density of the pharmaceutical powders

Abbreviation	Median particle size, d_{50} (µm)	Particle skeletal density, ρ_p (g/cm^3)	Particle bulk density, ρ_{bed} (g/cm^3)	Surface mean diameter, d_s (µm)
MCC	128	1.61	0.358	164.0
LMH	70	1.52	0.558	96.9
CCS	41	1.62	0.542	71.4
APAP	96	1.72	0.566	167.8
IBU	195	1.38	0.608	278.4

Table 3.4 Contact angle and modified Bond number of the pharmaceutical powders

Component	Abbreviation	Contact angle, θ (°)	Modified Bond number Bo_g^*
Microcrystalline cellulose	MCC	49.6±0.2	493.8
Lactose monohydrate	LMH	79.6±6.6	252.8
Croscarmellose sodium	CCS	84.9±0.6	236.1
Acetaminophen	APAP	82.9±3.1	56.8
Ibuprofen	IBU	83.8±2.1	16.8

3.4.2 Final granule size and morphology

For three excipients (LMH, CCS, and MCC), two APIs (APAP and IBU), and their mixtures with different API loading (see Tables 3.1 and 3.2), images of the final granules and their corresponding shape parameters are presented in Figure 3.4 and Table 3.5, respectively.

(a) APAP 20%　(b) APAP 15%　(c) APAP 10%

(d) APAP 5%　(e) APAP 0%　(f) IBU 20%

(g) IBU 15%　(h) IBU 10%　(i) IBU 5%

(j) IBU 0%　(k) LMH　(l) CCS

(m) MCC　(n) APAP only　(o) IBU only

Figure 3.4 Final granules produced using single drop granulation method.

Table 3.5 Size and shape parameters of final granule

Component	D_{max}, (mm)	D_{min}, (mm)	H_g, (mm)	D_a, (mm)	HAR	VAR
APAP 20%	7.23±0.21	6.09±0.03	3.47±0.07	6.82±0.06	1.19	1.97
APAP 15%	6.85±0.13	6.23±0.24	3.94±0.12	6.42±0.03	1.10	1.63
APAP 10%	7.32±0.14	6.12±0.05	3.10±0.02	6.74±0.10	1.15	2.17
APAP 5%	8.19±0.09	6.21±0.05	3.26±0.11	7.38±0.03	1.32	2.27
APAP 0%	8.22±0.18	6.21±0.07	2.24±0.12	7.42±0.07	1.34	3.31
IBU 20%	7.04±0.21	6.24±0.11	3.57±0.09	6.55±0.08	1.13	1.83
IBU 15%	6.35±0.20	5.64±0.21	3.11±0.11	5.99±0.04	1.13	1.93
IBU 10%	5.59±0.07	4.90±0.10	3.08±0.02	5.24±0.11	1.14	1.70
IBU 5%	6.54±0.16	5.47±0.17	3.18±0.07	6.02±0.05	1.20	1.89
IBU 0%	6.40±0.08	5.65±0.09	3.06±0.07	6.01±0.10	1.13	1.96
LMH	N/A	N/A	N/A	N/A	N/A	N/A
CCS	2.41±0.13	2.18±0.18	1.88±0.14	2.21±0.07	1.11	1.17
MCC	4.80±0.08	3.25±0.15	1.67±0.06	3.97±0.05	1.48	2.38
APAP	7.08±0.09	6.43±0.04	4.97±0.17	6.74±0.06	1.10	1.36
IBU	9.89±0.16	8.64±0.11	7.69±0.03	9.30±0.08	1.14	1.21

The final granule size was measured five times. The measurements were conducted on one sample of each individual component and pharmaceutical mixture. The relative deviation was found to be small (within 8.3%). Figures 3.4a-e show that, in general, an increase in the APAP concentration results in more round granules (*VAR* and *HAR* closer to 1). The granule of low APAP loading has a disk-like shape, which is similar to that obtained from pure MCC powders (see Figure 3.4m). Decreasing the APAP loading in the mixture changes the granule shape from round to plate. For another formulation, using IBU as the API, increasing the IBU concentration does not show a significant impact on the granule size, as shown in Figures 3.4f-i.

The granules of each individual ingredient are shown in Figures 3.4k-o. The gradual changes of granule size and morphology, as shown in Figures 3.4a-e (formulation 1 mixture) and Figures 3.4f-j (formulation 2 mixture), were not observed for the individual pure ingredients. The physical and chemical powder property differences result in significant granule differences. In general, powders with higher hydrophilicity (smaller contact angle) are more likely to form granules with lower sphericity, and those with lower hydrophilicity (higher contact angle) will result in more spherical granules. For the LMH granule, Figure 3.4k displays the top part of the whole granule. Since the LMH granule embedded in the powder bed layer firmly, the LMH granule size was not measurable. The CCS granule (see Figure 3.4l) has the highest sphericity and smallest size (see Table 3.5). As most of the water was sealed in the CCS shell, the size and shape of the granule are similar to those of the droplet. MCC powders have a relatively low contact angle (49.6°), which means higher hydrophilicity. The MCC granule (see Figure 3.4m) has a disk-like shape. For APAP (see Figure 3.4n) and IBU (see Figure 3.4o) granules, the HAR and VAR are closer to 1 (see Table 3.5). This is due to the lower hydrophilicity (contact angles of 82.9° and 83.8°, respectively). In Figure 3.4o, it is observed that there is a spherical core on the top of the granule. This may be related to the IBU powders' natural tendency to be cohesive and form agglomerates.

3.4.3 Granule internal structure

X-ray computed tomography (CT) was used to study the internal structure of the 20% APAP granule, and the results are shown in Figures 3.5a-g. The images of each slice were binarized using ImageJ to calculate the porosity. The porosity of each slice is shown in Figure 3.6. The reconstructed image from the CT scan and the locations of the slices for porosity studies are shown in Figure 3.5h. The granule was not removed from the powder bed during the CT scan to prevent potential destruction of the sample. From the top view (Figure 3.5b) and the side view of the granule (Figure 3.5h), there is a gap region that separates the granule and the rest of the powder bed. Three regions can be found in Figure 3.5h, including the gap region, the top region and the bottom region, based on the internal structure differences. The gap region has the highest porosity, as shown in Figure 3.6, and the top region has a higher porosity than the bottom region, which is consistent with the trend in Figures 3.5a-g.

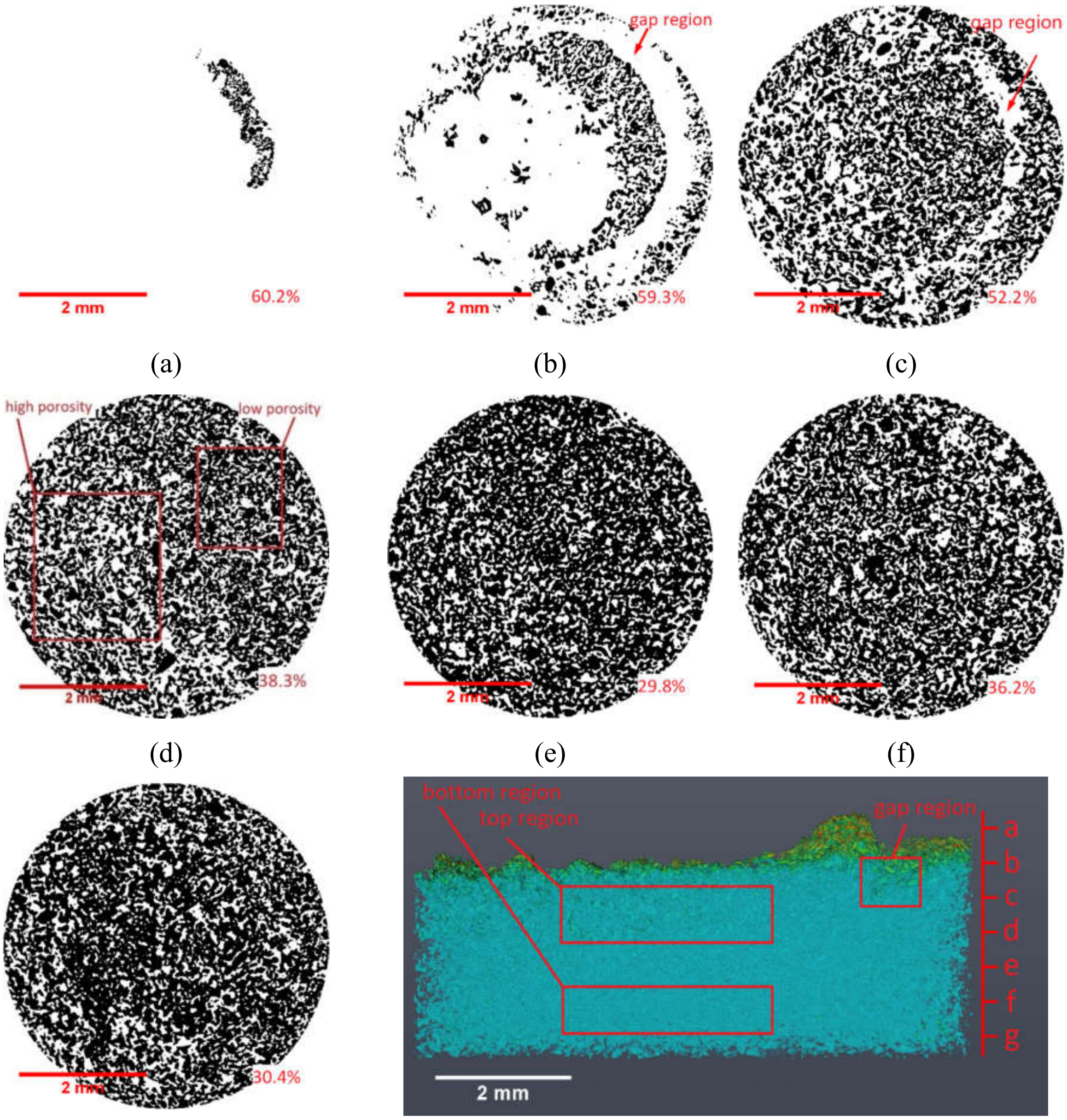

(a) (b) (c)

(d) (e) (f)

(g) (h)

Figure 3.5 Internal morphology results of the 20 % APAP granule: (a)-(g) slices of the granule, and (h) side view of the resultant granule.

In Figure 3.5d, two regions with different porosities can be observed. Similar results were reported by Gao et al. [81]. This may be due to the natural tendency for the finer powders to be cohesive and form agglomerates. This property also results in the gap regions in Figures 3.5b-c and the high porosity region in Figure 3.5d. In general, the porosity of the granule top region (Figures 3.5a-c) is higher than that of the bottom (Figures 3.5d-g). Similar porosity distributions are shown in Figures 3.5e-g. After the initial droplet distortion stage, the main driving force of the water movement in the powder bed is the capillary force, which results in a relatively even porosity distribution in the bottom part of the resultant granule. The porosity of Figure 3.5f is 5.8% to 6.4% higher than that of Figure 3.5e and Figure 3.5g. As shown in Figure 3.5a and Figure 3.5b, there is a crown embedded on the top of the granule. This crown structure results in the gap region and the noncontinuity of the porosity, as shown in Figure 3.6.

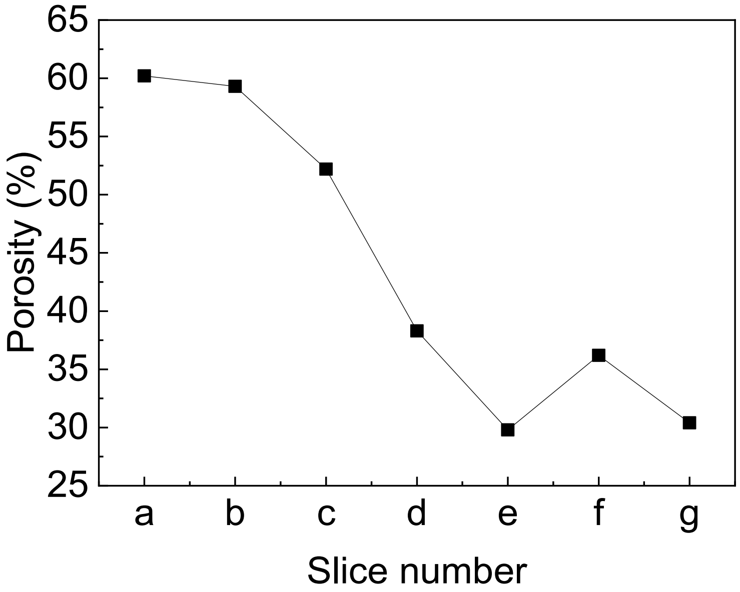

Figure 3.6 Porosity of each X-ray CT slice of the 20 % APAP granule.

3.5 Conclusions

Powders with higher hydrophilicity (smaller contact angle) are more likely to form granules with lower sphericity (plate-shaped), and lower hydrophilicity (higher contact angle) will result in more spherical granules.

In general, the porosity of the granule decreases from the top part to the bottom part of the granule. Three regions can be found in the granule, including the gap region, the top region and the bottom region, based on the internal structure differences.

CHAPTER 4. EXPERIMENTAL INVESTIGATION OF WET PHARMACEUTICAL GRANULATION USING IN-SITU SYNCHROTRON X-RAY IMAGING

The content of this chapter has been published in Powder Technology. 2021; 378. https://doi.org/10.1016/j.powtec.2020.09.063.

Contribution of the Ph.D. student:

The experiments were planned and performed by Chen Li. Lifeng Zhang supervised and provided consultation during the experiment preparation, data analyzing, image reconstruction, and thesis preparation. Ning Zhu and Heather N. Emady offered technical support during experiment design, set-up construction, and CT image reconstruction. Yuzhou Zhang provided assistance during the experiment result collection. The writing of the manuscript was done by Chen Li, with Lifeng Zhang providing editorial guidance.

Contribution of this chapter to the overall study

This chapter provides an advanced understanding of the effect of liquid binder, droplet release height, droplet volume, as well as particle size on the dynamic wet granulation process. For the first time, in-situ X-ray imaging techniques with high temporal and special resolutions were utilized to visualize the dynamic wet granulation. The interaction between pharmaceutical powders and movement of beneath bed surface were quantitively studied. These results are critical for understanding the classification of the wet granulation mechanism and the effects of critical operating conditions, including liquid binder, release height of the liquid binder, droplet volume, particle size on the wet granulation process.

4.1 Abstract

Observing the dynamic wet granulation processes and measuring the size and shape of droplet

and granules of pharmaceutical powders are challenging with conventional experimental methods due to their opacity and the complex interaction that happens in a short time. In this study, the synchrotron in-situ imaging technique was, for the first time, employed to capture the dynamic granulation process with the single drop impacting method. Two common pharmaceutical excipients and an active pharmaceutical ingredient (API) were used as the powder beds. Three liquids were used as binders. A new parameter, overall movement ratio, r_m, is introduced to quantitatively describe the movement of the liquid binders in the powder beds. The dynamic interactions between the liquid binder and solid powders were captured via high temporal and spatial resolution X-ray images.

Results show that particles with smaller sizes have the tunneling mechanism, and the spreading mechanism occurs with larger particles, as expected. Liquid binder properties, including viscosity and contact angle, and operation parameters including droplet release height and volume show significant impacts on the dynamic granulation process. This study demonstrates the potential of using in-situ synchrotron X-ray imaging technique to quantitatively study the dynamic wet granulation process.

4.2 Introduction

Wet granulation is an important unit operation in the chemical and pharmaceutical industries. Fine particles can be bonded with a liquid binder to form powder agglomerates during wet granulation. There are three main stages during the wet granulation process, namely wetting and nucleation, consolidation and growth, and breakage and attrition [82]. Due to the opaque nature of powders and the complex interaction between the liquid binder and powders, most research efforts have been placed on final granule properties such as granule size, size distribution, granule shape and internal structure [65, 69, 83, 84]. Despite the success in the visualization of final granules with traditional methods, including optical cameras and lab-based X-ray imaging techniques, observing the dynamic granulation process is still challenging. Visualization of the dynamic wet granulation process is vital to understanding granulation mechanism, granule size control, and scaling-up [11].

The key factors influencing the granulation process are the content, viscosity, and surface tension of binder and particle size [65]. Increasing the viscosity of a liquid binder can decrease the consolidation rate generally due to the increased viscous force [85, 86]. Decreasing the surface tension of a liquid binder will decrease the capillary forces, which can hold powders together [87]. Reducing the particle size can decrease the rate of the granulation process [88]. Smaller particles will decrease the particle bulk density and increase the average pore size in the packed powder beds. These two factors constrain the liquid binder movement within the powder beds. Most of these studies are limited to qualitative analysis; however, quantitative studies of the effects of the above key parameters are important to gain a better understanding of granulation.

In the literature, the high-speed camera technique is the main optical experimental method used to observe the dynamic granulation process [89-91]. This is a traditional method investigating wet granulation from the top view. The three typical granule formation mechanisms, "tunneling," "spreading," and "crater formation," can be identified with this method [20, 92]. A particle Bond number was used to classify the three different granulation mechanisms [92, 93]. The modified particle Bond number can be calculated as:

$$Bo_g^* = \frac{\gamma \cos\theta}{d_s^2 \rho_{bed} g} \tag{4.1}$$

where γ is the liquid surface tension, θ is the powder-liquid contact angle, d_s is the surface mean particle diameter, ρ_{bed} is the particle bulk density, and g is the gravitational acceleration constant.

The main limit of the high-speed camera technique is that the granulation process can only be approximated from the perspective of the powder bed surface using this method, whereas the movement of the liquid beneath the powder bed surface cannot be observed directly.

X-ray imaging techniques are considered to be promising methods to be deployed to study the granulation process. The main advantage of the X-ray imaging techniques over optical methods is the non-invasive nature and the ability to investigate the internal structures of granules [94]. Due to the low energy flux of lab-based X-ray computerized tomography (CT), it is mostly applied to study the internal structures of granules with particle sizes larger than 1 mm. In recent years, synchrotron-based X-ray imaging has attracted more attention in granulation studies. Synchrotron-based X-ray imaging, with higher photon flux than conventional X-ray sources, has the ability to capture high-resolution images within a field of view (FOV) smaller than 1 mm^2 and dynamic images with high resolution. Chen et al. [95] studied the dynamic granulation process and the internal structures of granules with synchrotron-based X-ray imaging. It was found that the granule porosity decreases from the top part to the bottom part of the granule. Lu et al. [96] studied the internal structure of and fractal dimensions of three types of traditional Chinese medicine granules. Two fractal dimension parameters, namely, the volume matrix and the surface matrix, were used to characterize granules with irregular structures and evaluate the effects of production processes on the structures of granules. Alain et al. [97] compared the images obtained from synchrotron radiation micro-diffraction and electron diffraction. Compared with electrons, X-rays can more easily penetrate the 1−100 μm thickness of any starch granule with a higher spatial resolution. Steven et al. [98] described the particle, binder, and air volume distributions in granules produced from glass ballotini particles and aqueous PVP binder using X-ray micro-tomography. Shuji et al. [99] studied the internal structure of fine granules that were 200–300 μm. The different visualization properties of the ingredients under X-ray were used to analyze the coating layer with high talc-content in a granule. Hajime et al. [100] deployed synchrotron X-ray CT to investigate the granule internal structure during the drug release process. The particle sizes of the granules used were from 250 to 350 μm. The shape of the void space in the central part of the granules was found not to change even after 50% drug release. Ranjit et al. [101] investigated the effect of screw length on granule porosity in a twin screw granulator with a synchrotron X-ray CT. Liu et al. [102] studied the mixing and segregation of binary pharmaceutical granules after granulation using synchrotron X-ray CT techniques. However, most of these studies were focused on the final granulation products.

The dynamic granulation process has not been investigated with high-resolution in-situ imaging methods. E. Gallucci et al. [103] studied the microstructure of cementitious materials with in situ synchrotron X-ray microtomography at the Swiss Light Source. The porosity evolution of the hydration process of cement materials over time (0-65 days) was investigated at a pixel resolution of 0.6835 μm. Results show synchrotron-based X-ray CT is the only non-invasive in situ imaging technique to study cement materials. Cai et al. [104] used high-speed synchrotron X-ray tomographic microscopy to quantitatively analyze the compressive deformation of a semi-solid Al-15 wt.% Cu alloy containing 30% liquid. Yoshiharu et al. [105] monitored the phase transition process of native starch granules with in-situ synchrotron x-ray diffraction. Moritz-Caspar et al. [106] applied time-resolved synchrotron X-ray diffraction to observe the dynamic hydration processes during the first seconds of cement hydration. The early formation of ettringite and the interaction of polycarboxylate ethers with cement particle surfaces were investigated. Cheng et al. [107] investigated the micro-scale mechanical behaviour of granular soils under shear with an in–situ synchrotron X-ray. Me et al. [108] observed the mechanical behavior of partially solidified Al–Cu alloys with an in-situ synchrotron X-ray to assess the influence of mushy zone deformation on hot tearing. From the literature, it can be seen that the high photon flux of the synchrotron-based X-ray radiographic imaging techniques makes it possible to capture the details of the granulation process at a fast image capture rate (14-40 FPS). Therefore, this study attempts to apply synchrotron-based X-ray radiographic imaging techniques to understand the influence of liquid binders, droplet release heights, droplet volumes, and particle sizes on the dynamic granulation processes of pharmaceutical powders.

4.3 Materials and methods

4.3.1 Materials characterization

Two common excipients, microcrystalline cellulose (MCC) and lactose monohydrate (LMH), and an API, acetaminophen (APAP), were selected as pharmaceutical powders. All of the materials were sieved through a 2.00 mm sieve to remove oversized powders and aggregates. MCC and

LMH powders were sieved through a sieve with a 38 μm opening size after the preliminary sieving to obtain fine microcrystalline cellulose (MCCF) and fine lactose monohydrate (LMHF) powders. Regular and fine MCC and LMH powders were used to study the effect of particle size on the wet granulation process. Then powders were loaded into sample cuvettes with a powder bed height of about 3 cm. The cuvettes have a square cross-sectional area with a side length of 1 cm and a height of 4 cm. The powder beds were levelled with a metal panel to ensure a smooth surface.

The characterization of the powder materials used in this study includes median particle size, surface mean diameter, particle bulk density, particle skeletal density, and modified particle Bond number [18]. The median particle size and surface mean diameter were measured with a Malvern 2000 Mastersizer S (Malvern Instruments, UK). The bulk density was calculated as the mass per unit volume after loading 100 g of powder into a 200 ml graduated cylinder and measuring the volume of the powder. The particle skeletal density was obtained by a Ultrapycnometer 1000 (Quantachrome Instruments, Austria).

Deionized water, isopropanol, and ethanol were used separately as liquid binders. The ethanol and isopropanol were purchased from Thermo Fisher Scientific. The contact angle of the liquid binders with MCC, MCCF, LMH, LMHF, and APAP was determined with the Washburn capillary rise (WCR) method [18].

4.3.2 Synchrotron radiography projection setup

The experiments were conducted at the Biomedical Imaging and Therapy Facility (BMIT) 05B1-1 beamline at the Canadian Light Source (CLS). The synchrotron radiography setup with a white beam (polychromatic beam) used for visualizing the wet granulation dynamics is shown in Figure 4.1 [95]. Sample cuvettes were placed at 25 m from the beam source with 50 cm of the sample-to-detector distance.

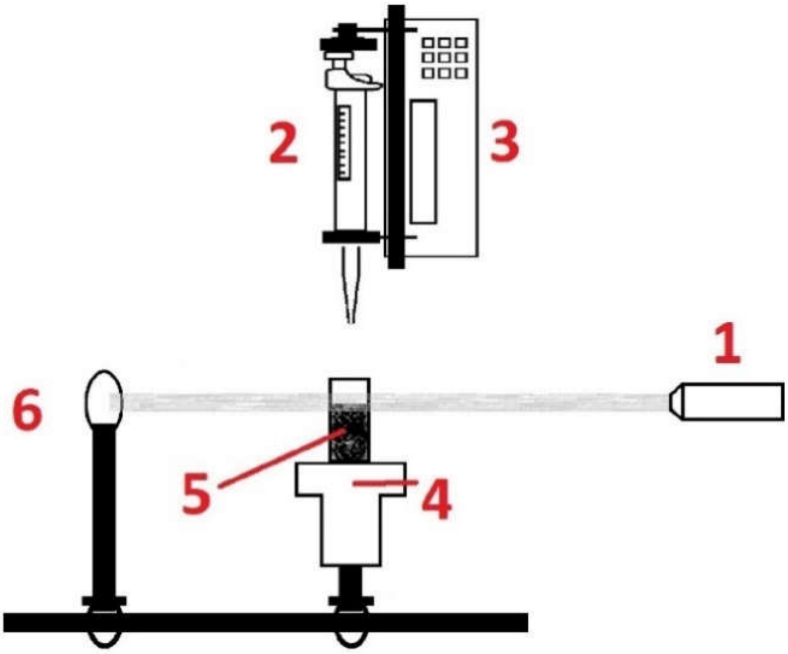

Figure 4.1 Single drop experimental setup: 1) synchrotron light source, 2) micropipettor, 3) syringe pump, 4) high precision motorized stage, 5) sample vessel, and 6) detector.

The images obtained from the BMIT include both the X-ray absorption contrast and the phase contrast. The projected images were captured by a beam monitor AA-40 (Hamamatsu, Japan) and a camera (Hamamatsu ORCA Flash 4.0, Japan). The field of the window was 6.66 x 4.50 mm^2 with an effective pixel size of 6.5 μm and a bit depth of 16-bit. The backgrounds were corrected utilizing ImageJ software with flat and dark field images collected during each scan [80]. The last image before the droplet moved into the window was subtracted from all of the following raw image sequences to observe the details beneath the bed surface. Sequences of images were captured during the process with a scan rate of 14.7 frames per second (FPS), namely, a 68 ms time interval between two images.

4.3.3 Granule morphology

An example of granule shape measurements taken during the dynamic granulation process is illustrated in Figure 4.2. The modified Bond number can be used to classify the granulation mechanisms (spreading, tunneling, crater formation), but cannot be used to directly describe the dynamic liquid movement during the wet granulation process. This classification is based on the ratio of the capillary force on a particle and the gravitational force acting on the particle, which measures the relative magnitude of the cohesive force acting on the particle due to liquid bridges [92]. Therefore, in this work, a new parameter, the overall movement ratio r_m, is introduced to characterize the dynamic process and is defined as:

$$r_m = v_v / v_r \tag{4.2}$$

where v_v is the water movement velocity in the vertical direction, and v_r is the water movement velocity in the radial direction. v_v and v_r can be calculated with the following equations:

$$v_v = \frac{\mathrm{d}h_g}{\mathrm{d}t} \tag{4.3}$$

$$v_r = \frac{\mathrm{d}d_g}{\mathrm{d}t} \tag{4.4}$$

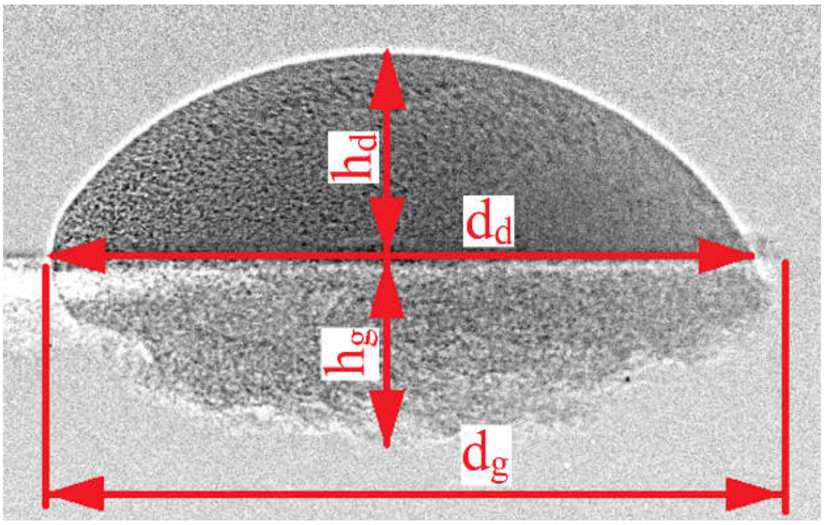

Figure 4.2 Illustration of granule morphology measurements taken during the dynamic granulation process (h_d: droplet height, d_d: droplet diameter, h_g: granule height under the bed surface, d_g: granule diameter).

When the overall movement ratio, r_m, is larger than 1, liquid mainly moves vertically, which is also defined as the tunneling (or penetration) granulation mechanism [20]. When r_m is smaller than 1, liquid mainly moves radially, which is also defined as the spreading granulation mechanism.

4.3.4 Uncertainty analysis

The contact angles between pharmaceutical powders and liquid binders were measured three times to calculate the mean values and standard deviations. The standard deviations of the contact angles are within 13.6%.

The granule and droplet sizes of LMH powders with water as a liquid binder released from 2.5 cm at a volume of 15 μl were measured five times, and mean values of droplet height, droplet diameter, granule height under the bed surface, and granule diameter were used. The standard deviations were between 0.006 mm to 0.020 mm, which means 1 to 3 pixels. The standard deviations are within 1.0% of the mean value.

4.4 Results and discussion

4.4.1 Physical properties of pharmaceutical powders and liquid blinders

The results of the physical properties of the pharmaceutical powders used in this work are presented in Table 4.1. MCC has the largest surface mean diameter (164.0 μm). After screening through a sieve with the 38 μm opening size, the surface mean diameter of MCCF decreased to 29.8 μm. LMHF has the smallest surface mean diameter (26.5 μm) among the powders used in this project. The particle skeletal density of all of the powders is within a narrow range of 1.52-1.72 g/cm^3.

Table 4.1 Physical properties of pharmaceutical powders

Component	Abbreviation	Median particle size, d_{50} (µm)	Particle skeletal density, ρ_p (g/cm3)	Particle bulk density, ρ_{bed} (g/cm3)	Surface mean diameter, d_s (µm)
Microcrystalline cellulose	MCC	128	1.61	0.358	164
Microcrystalline cellulose (fine)	MCCF	27	1.65	0.488	30
Lactose monohydrate	LMH	70	1.52	0.558	97
Lactose monohydrate (fine)	LMHF	22	1.55	0.597	27
Acetaminophen	APAP	96	1.72	0.566	168

The liquid binder properties are given in Table 4.2. Ethanol and isopropanol are usually mixed with water to adjust the surface tension of the liquid binder mixture [109]. The surface tension and viscosity of the two organic liquid binders are close to each other, but very different from that of deionized water. The contact angles between all of the liquid binders and pharmaceutical powders used in this study are smaller than 90°, which means the powders are all hydrophilic, although many of the contact angles are close to 90°.

Table 4.2 Physical properties of liquid binders

Liquid	Density, (g/cm^3)	Surface tension (mN/m)	Viscosity (mPa·s)	θ with MCC, (°)	θ with MCCF, (°)	θ with LMH, (°)	θ with LMHF, (°)*	θ with APAP, (°)*
Deionized Water	0.997	72.0 [76]	0.89 [77]	45.6 ±1.2	47.2± 6.4	82.7 ±0.4	85.3± 2.7	84.2±0.3
Ethanol	0.788	22.0	1.35	80.3 ±1.5	55.8± 4.7	87.9 ±0.6	87.6± 3.4	88.6± 0.6
Isopropanol	0.785	23.0	2.27	82.2 ±1.8	57.9± 3.9	88.4 ±0.3	88.4± 1.8	87.5± 0.4

The modified Bond numbers, Bo_g^*'s, between all of the liquid binders and powders are shown in Table 4.3. The modified Bond numbers of deionized water with all powders are noticeably higher than those of ethanol and isopropanol. MCCF powders have the highest Bo_g^*, and APAP powders have the lowest Bo_g^* among all of the powders investigated in the present work. Decreasing the particle size results in a larger Bo_g^*. Even though Bo_g^*'s have a wide range of 3.4 to 12000, they are still within the range of the spreading mechanism as defined by Emady et al., who note that the boundary between spreading and tunneling is $Bo_g^{*}=100000$ [92].

Table 4.3 Modified Bond number, Bo_g^*

Liquid	MCC	MCCF	LMH	LMHF	APAP
Deionized Water	530	12000	180	1400	47
Ethanol	39	2900	15	220	3.4
Isopropanol	33	2900	13	160	6

4.4.2 Effect of the liquid binder

The granulation process of LMH and MCC powders with three liquid binders (deionized water, ethanol, and isopropanol) was studied at a drop height of 2.5 cm with a droplet volume of 15 µl. The granulation process of LMH powder is illustrated in Figure 4.3. For all of the liquid binders, the observed granulation process includes three stages: impaction, attaching and penetration. As shown in Figures 4.3 a1, b1 and c1, the shape of the droplet changes dramatically in a short period of time (less than 68 ms) during impaction. The time interval between two images is 68 ms, which means that if the droplet changes drastically within a time shorter than 68 ms, the changes cannot be observed directly, and thus the changes can be estimated as happening in under 68 ms. The isopropanol droplet rolls and deforms in the horizontal direction when it reaches the bed surface, as shown in Figures 4.3 b1 and b2.

During the following attaching stage, the powders attach to the droplet surface, and the shapes of the droplet remain stable, as shown in Figures 4.3 b2 and c2. The attaching stage of the LMH powder with water is shorter than that for isopropanol and ethanol. Figure 4.3 a1 displays the end of the attaching stage and the beginning of the third stage with water, while the granulation processes with isopropanol and ethanol are still at the attaching stage in the first 200 ms. The last stage can be classified into two types according to the movement direction of the liquid within the powder bed, namely spreading and penetration. Spreading is defined as the stage when the liquid mainly moves radially, while penetration is the stage when the liquid primarily moves vertically. The movement of the liquid in the powder bed layer is mainly in the vertical direction, as displayed in Figures 4.3 a3-4, b3-4, c3-4, which is penetration.

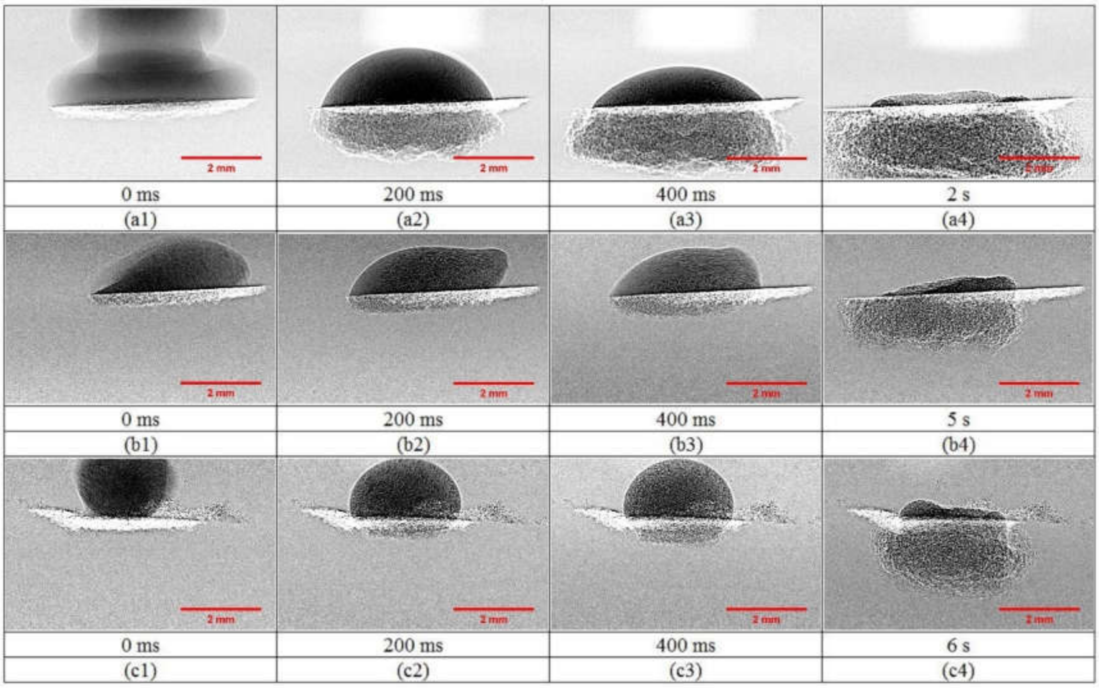

Figure 4.3 Time sequence X-ray images of the granulation process for LMH powder with (a1-a4) water; (b1-b4) isopropanol; and (c1-c4) ethanol, as a liquid binder with a drop height of 2.5 cm and a droplet volume of 15 μl.

The size of the LMH granule during the granulation process is shown in Figure 4.4. The duration of the impaction stage can be described by the droplet diameter (d_d) and the droplet height (h_d), as illustrated in Figure 4.4a. The impaction stage is mainly influenced by the surface tension of the liquid binders, which means that the higher the surface tension, the shorter the impaction stage. The droplets do not show significant variation in the first few points, which means that the impaction stage is shorter than the scan interval of 68 ms. The following attaching stage is mainly influenced by the powder and droplet size difference and contact angle. Attaching only occurs when the droplet size far exceeds the particle size and the surface tension force can overcome the gravity force of the individual powders.

If the gravity force of the liquid binder is ignored, the movement of the liquid in the powder bed is driven by the surface tension force (or capillary force) minus the resistance force, namely the viscosity force. The powder bed can be classified as a porous medium, which includes multiple capillary tubes in all directions. For a single capillary tube, the component force in the axial direction of the capillary force can be calculated as:

$$F_c = \pi d \gamma cos\theta \tag{4.5}$$

where d is the capillary tube diameter, γ is the surface tension force, and θ is the contact angle.

The capillary tube diameter, surface tension force, and contact angle are assumed to be constant during the granulation process. Thus, the capillary force is dominated by the number of capillary tubes, which means that a powder bed with a smaller particle size tends to have a larger total capillary force. This results in the tunneling mechanism and rounder final granule product. When the granule diameter increases, the contact surface and total capillary force increase at a rate proportional to the granule diameter squared.

The viscosity force of the same capillary tube is:

$$F_v = \pi d L u_0{}' \tag{4.6}$$

where L is the capillary tube length and $u_0{}'$ is the derivative of the liquid velocity at the capillary tube boundary. The viscosity force is dependent upon the total inner wall surface area of all of the capillary tubes. When the granule diameter increases, the total viscosity force increases at a rate proportional to the granule diameter cubed (d_g^3).

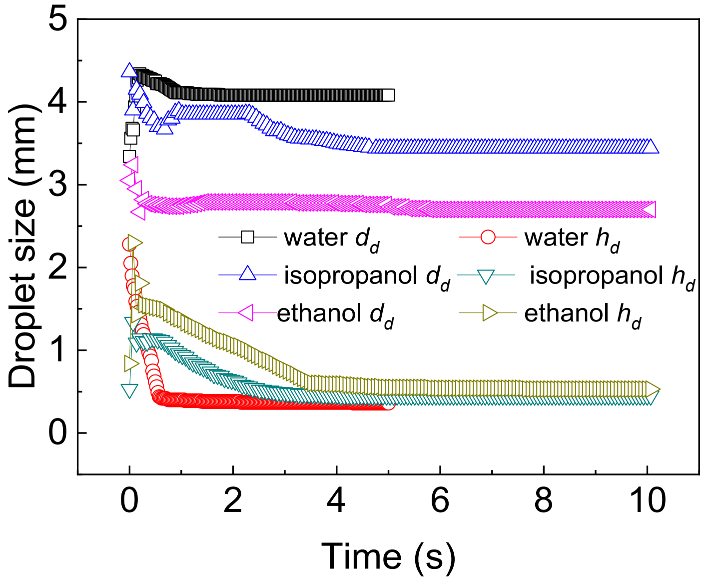

(a)

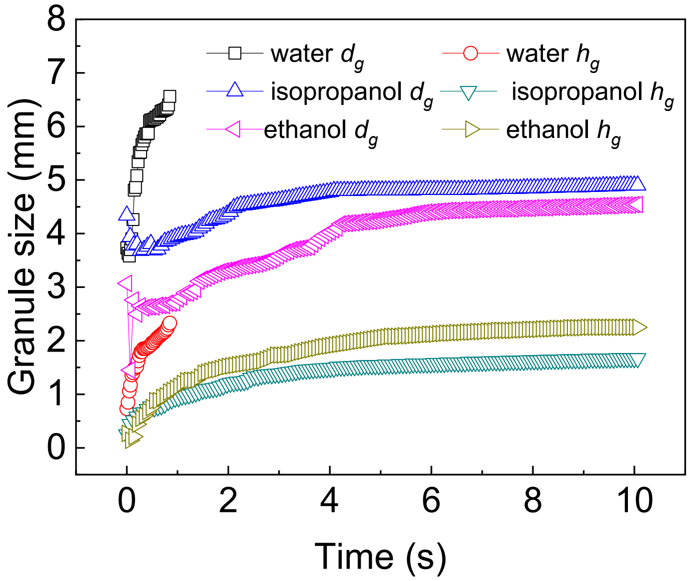

(b)

Figure 4.4 Size of the LMH granule with water, isopropanol, and ethanol as a liquid binder with a drop height of 2.5 cm and a droplet volume of 15 µl: (a) droplet size, and (b) granule size.

The viscosity force is smaller than the capillary force when the droplet just contacts the powder bed, but the viscosity force increases at a higher rate. The difference between the capillary force and the viscosity force decreases with the granule growth. When the capillary force equals the viscosity force, the granulation process ends, and the granule stops growing. The impaction and attaching stages should be surface tension dominated, and the following stages, spreading and penetration, should be dominated by both viscosity and surface tension.

The granule size is shown in Figure 4.4b. Water penetrates and spreads through the powder bed within 2 s, much shorter than isopropanol (5 s) and ethanol (6 s). The final granule formed with water has a diameter over 6.5 mm and a height over 2.5 mm. The diameter of the final granule formed with isopropanol is 5 mm and the height is 1.5 mm. The granule formed with ethanol has a smaller size and longer penetration, which is due to the low surface tension of ethanol.

The overall movement ratio, r_m, is shown in Figure 4.5. During the first 200 ms, r_m is negative, which is related to the distortion of the droplet when bouncing during impact onto the powder beds. These points are not shown in Figure 4.5 because of the logarithmic format of the figure. For the granulation processes with all the three liquid binders, r_m remains 1 after 5 s as the liquid movement in the powder beds almost stops, and the granule shape remains stable. The mean value of r_m with water as the liquid binder is 1.20, that with isopropanol is 0.83, and that with ethanol is 1.58. This means that water and ethanol move faster in the vertical direction, while isopropanol moves faster in the radial direction within LMH powder.

When using water as the liquid binder, as shown in Figure 4.5a, water first mainly moves radially (r_m <1) before 0.35 s. Afterwards, water starts to move vertically (r_m >1) during the period from 0.35-1 s. For the granulation process with isopropanol, which is shown in Figure 4.5b, it is found that most of the values are below 1, which means that isopropanol tends to move radially. This is due to the relatively high contact angle (88.4°) between isopropanol and LMH powder, which means higher hydrophobicity. From Figure 4.5c, it can be found that when using ethanol as the liquid binder, the liquid movement mainly has two stages; the first stage is from 0 to 1 s, when the liquid mainly moves vertically (r_m >1), followed by radial movement (r_m <1) from 1 to 5 s.

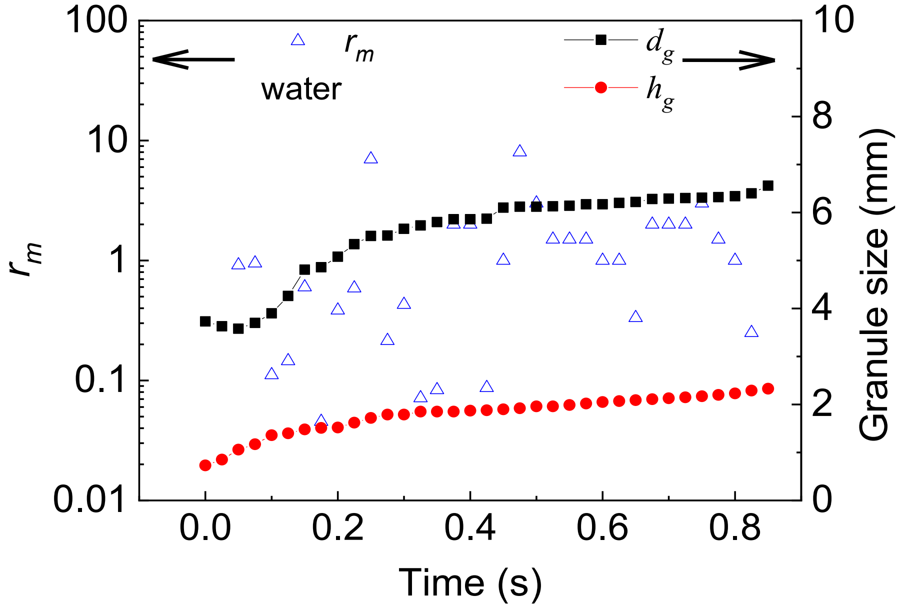

(a)

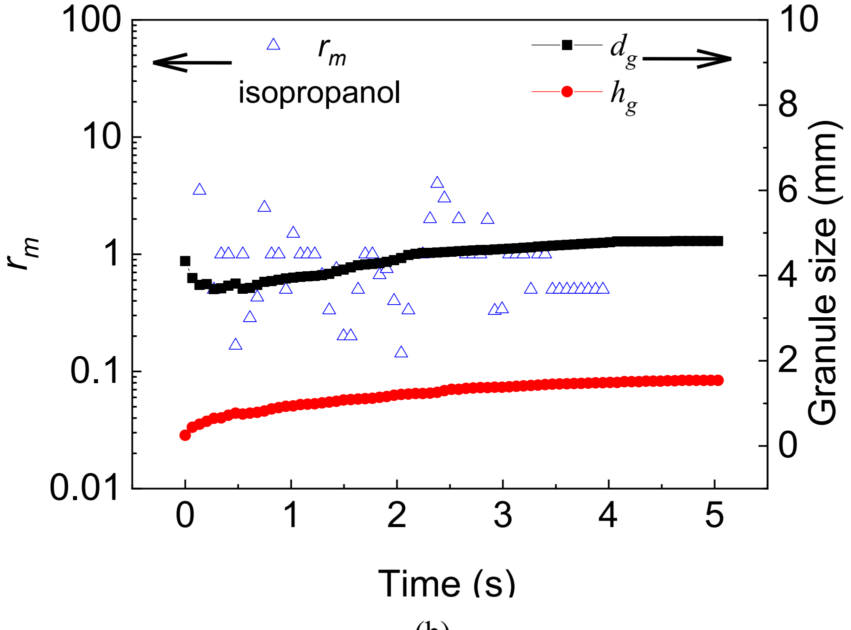

(b)

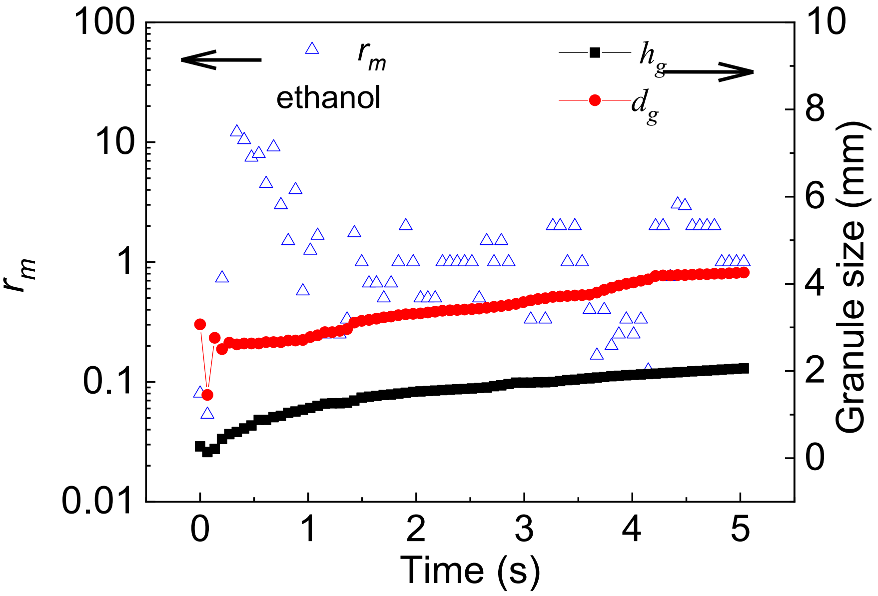

(c)

Figure 4.5 Overall movement ratio and granule size with (a) water, (b) isopropanol, and (c) ethanol as liquid binder with a drop height of 2.5 cm and a droplet volume of 15 µl.

The granulation process of the MCC powder is illustrated in Figure 4.6. Due to the low contact angle (45.6° with water) of the MCC powder, the impaction, attaching and spreading stages were significantly shorter when compared with the LMH powder. This is due to the smaller contact angle of the MCC powder with water (45.6°) compared that with isopropanol (82.2°) and ethanol (80.3°). This caused the water to move mainly radially, so spreading is the last stage of granulation of the MCC powder with all liquid binders, as shown in Figures 4.6a2-4, b2-4, and c2-4.

The granulation process of the MCC powder with isopropanol is shown in Figure 4.6b1-4, and that with ethanol is shown in Figure 4.6c1-4. Both processes are the spreading mechanism. The granulation process with isopropanol and ethanol has a shorter granulation time (less than 200 ms) and a smaller final granule size than that with water. Using the "image calculator" function in ImageJ software to subtract one image from another, the moving track of the liquid within the powder bed during the time interval between the two images can be obtained. The liquid movements of water, isopropanol, and ethanol in the vertical direction during the first 68 ms are 0.22 mm, 0.55 mm and 0.40 mm. The size of the final granule, $d_g * h_g$, formed with water is over 6.6 mm * 2.1 mm, which is larger than that with isopropanol (4.7 mm * 1.3 mm) and ethanol (4.9 mm * 1.4 mm) when comparing Figure 4.6a4, b4, and c4. This is mainly due to the differences in surface tension and viscosity. Increasing the surface tension and decreasing viscosity can shorten the granulation time and decrease the final granule size.

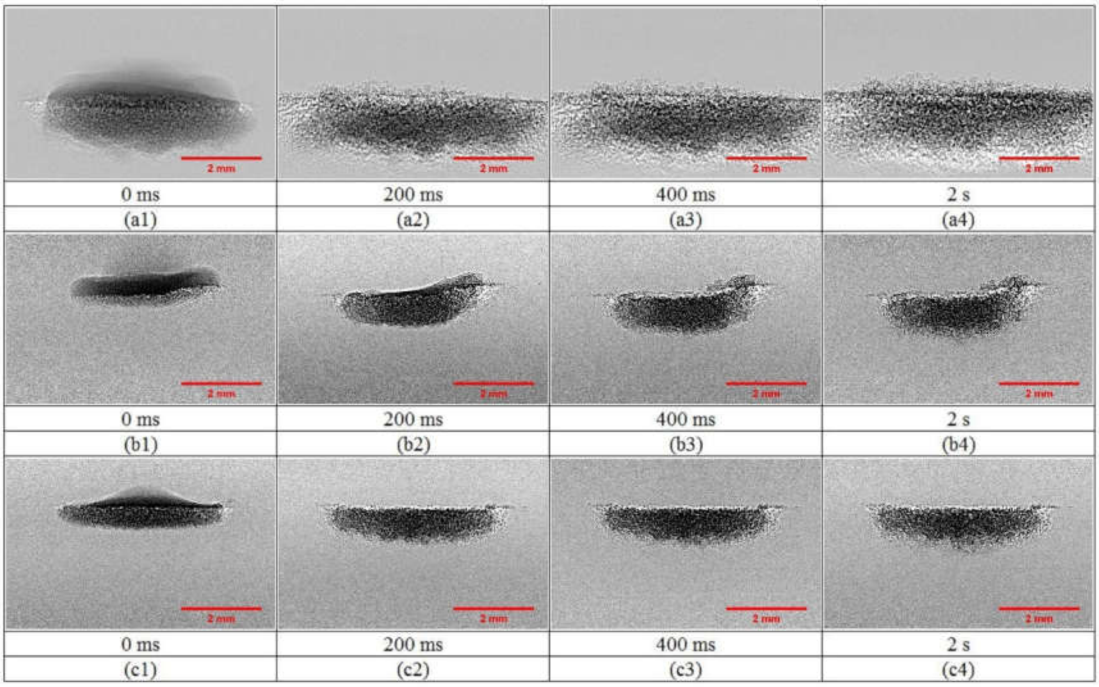

Figure 4.6 Time sequence X-ray images of the granulation process for MCC powder with (a1-a4) water, (b1-b4) isopropanol, (c1-c4) ethanol, as a liquid binder with a drop height of 2.5 cm and a droplet volume of 15 μl.

4.4.3 Effect of droplet release height

The effect of the droplet release height on the granulation process is different with LMH and MCC powders. For the LMH powder (d_s=90 μm), a droplet released from a higher height, 15 cm, experienced a drastic impaction stage, which formed a shield of powder on the droplet surface. Comparing Figure 4.7a1 and 4.7b1, it can be found that the contact area of the water droplet, when released from a height of 15 cm (Figure 4.7b1), is 67% larger than the area in Figure 4.7a1. The shield of attached powders prevents further contact between the water and the powders in the bed, which makes the penetration stage last longer compared with a droplet release height of 2.5 cm. For the MCC powder (d_s=164 μm), the granulation process with a droplet released from 15 cm follows a crater formation mechanism.

The granulation process of the LMH powder is shown in Figure 4.7. The granulation process with a 2.5 cm droplet release height follows the spreading granule formation mechanism, and that at a 15 cm droplet release height follows the crater formation granule formation mechanism [20]. During the granulation processes at both droplet release heights, the first stage is impaction. The droplet experiences a more significant distortion when released from a height of 15 cm than when released from 2.5 cm, as can be seen in Figures 4.7a1 and 4.7b1. LMH powders attach thoroughly, and all of the droplet surfaces are covered with a shield of powder when the droplet distorts drastically with the powder bed. This shield prevents further contact between the liquid and external powder, as can be seen from Figures 4.7b2-4.

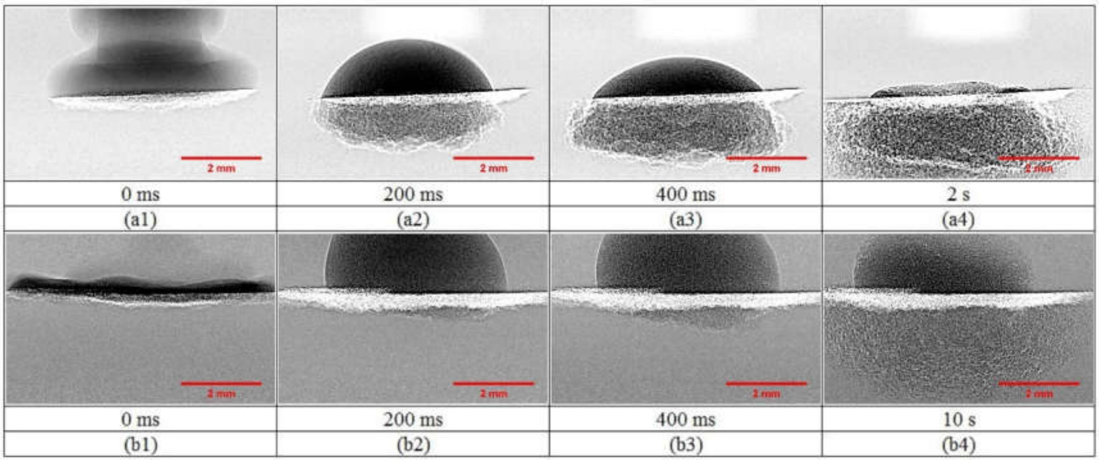

0 ms (a1) 200 ms (a2) 400 ms (a3) 2 s (a4)

0 ms (b1) 200 ms (b2) 400 ms (b3) 10 s (b4)

Figure 4.7 Time sequence X-ray images of the dynamic wetting and nucleation process of LMH powder with a water droplet volume of 15 µl and release heights of (a1-a4) 2.5 cm and (b1-b4) 15 cm.

The LMH granule size is shown in Figure 4.8. The droplet diameter, d_d, increases dramatically from 0 to 25 ms, followed by a slow decrease in the size. For droplets released from a height of 2.5 cm, the decreasing time of d_d (25 to 2000 ms) is shorter than that of the 15 cm release height (25 to 7500 ms). The droplet height, h_d, decreases gradually for droplets with a release height of

2.5 cm. The droplet released from 15 cm remains almost stationary after the impaction stage, meaning the shield of powder on the droplet surface negatively influences the liquid-external powder contact. The external boundary of the droplet was not measured after 125 ms because the droplet exceeded the FOV of the camera. The relatively small particle size (d_s=97 μm) and relatively low hydrophilicity (contact angle θ=82.7° with water) of LMH powder result in a larger amount of powder attached to the droplet surface.

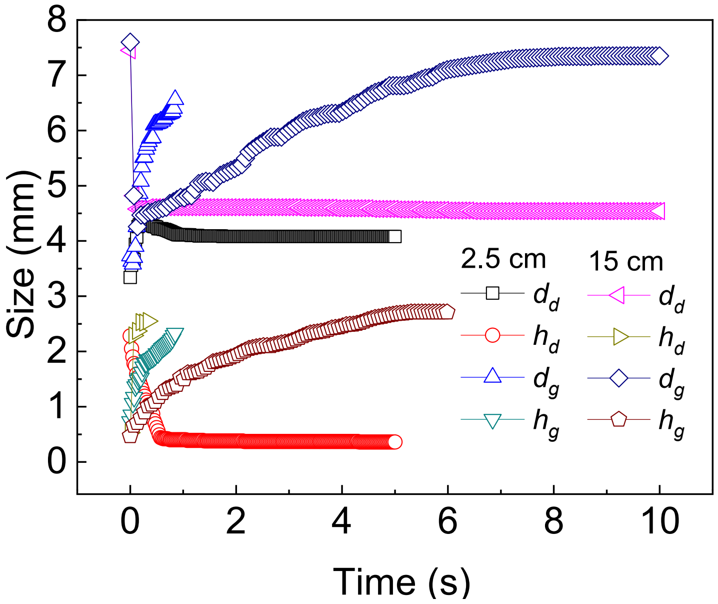

Figure 4.8 The size of the LMH granule with water as liquid binder and a 15 μl droplet volume.

The dynamic granulation process of MCC powder with water as a liquid binder at different droplet release heights is displayed in Figure 4.9. It can be noticed from Figure 4.9b2 that when the droplet is released from a height of 15 cm, the droplet with higher kinetic energy (estimated impact velocity of 1.7 m/s) forms a crater. On the other hand, when the height is at 2.5 cm, the water mainly moves radially and forms a flat-shaped granule, as shown in Figures 4.9a1-4. These observations are consistent with the spreading and crater formation mechanisms introduced by

Emady et al. [20].

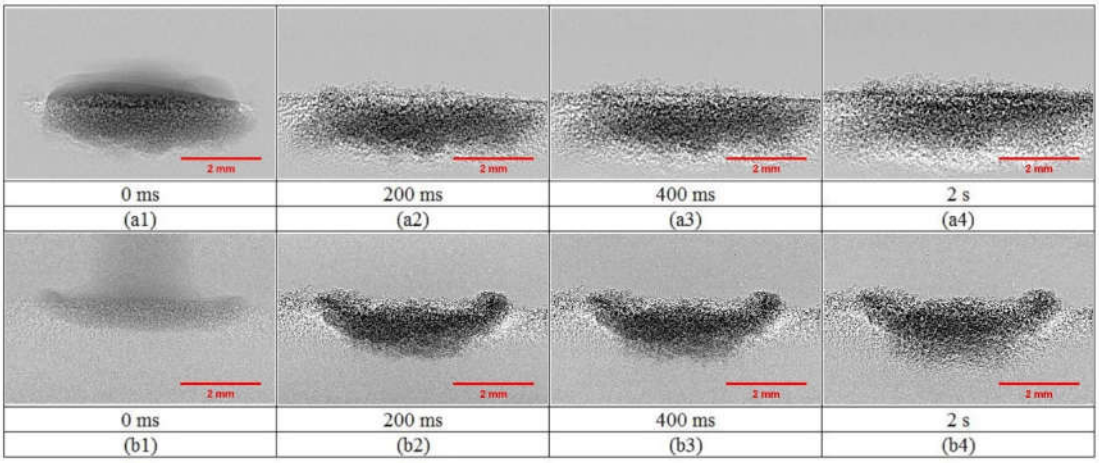

Figure 4.9 The time sequence X-ray images of the dynamic wetting and nucleation process of MCC powder with a water droplet volume of 15 µl and release heights of (a1-a4) 2.5 cm and (b1-b4) 15 cm.

4.4.4 Effect of droplet volume

In order to investigate the effect of the droplet volume on the granulation process, liquid water was employed as a liquid binder, and a drop release height was fixed at 2.5 cm. Figure 4.10 illustrates the wetting and nucleation process of the LMH powder. It can be seen that the attaching and penetration stages are much longer when the droplet volume is 10 µl. The smaller the droplet volume, the smaller the difference between the droplet diameter and the particle size, and the slower it takes for the powders to attach. This effect can be explained by the forces on the droplet. Before impaction, the droplet shape remains unchanged due to the balance between the surface tension and gravity forces. When the droplet comes into contact with the powder bed, the capillary force acts on the liquid at the contact surface. When the surface tension cannot overcome the gravity and capillary forces, the liquid starts to move into the powder bed. Considering the surface tension force can only act on the surface of the droplet, the smaller the droplet, the higher the surface force per unit mass. Therefore, the smaller droplet usually results in a slower granulation process; for example, the time of the LMH powder granulation process increases from 2000 ms to 6000 ms when going from a droplet volume of 15 µl to 10 µl.

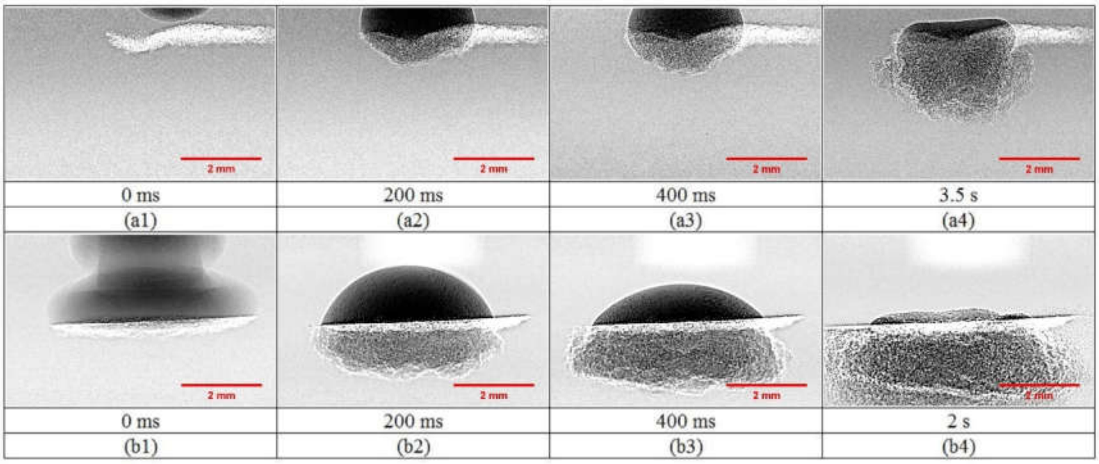

Figure 4.10 The time sequence X-ray images of the granulation process of LMH powder with water as a liquid binder released from 2.5 cm at volumes of (a1-a4) 10 µl and (b1-b4) 15 µl.

The granulation process of MCC powder with water as a liquid binder, released from 2.5 cm at volumes of 10 µl and 15 µl, is illustrated in Figure 4.11. The three stages, namely impaction, attaching, and spreading, are very short. The granulation process for both cases is completed within 2000 ms. The difference of time between the two processes is not very obvious, considering the image capture interval is 68 ms. Due to this powder having the largest particle size (d_s=164 µm) and the smallest contact angle (θ=45.6°), the effect of droplet volume on granulation is not as significant as it is for smaller particles with a larger contact angle.

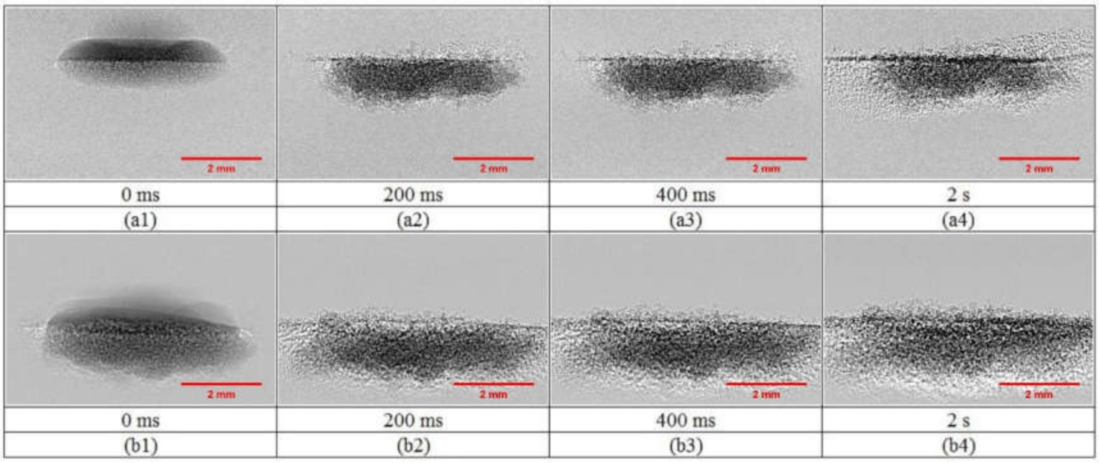

Figure 4.11 The time sequence X-ray images of the granulation process of MCC powder with water as a liquid binder released from 2.5 cm at volumes of (a1-a4) 10 µl and (b1-b4) 15 µl.

The granulation process of APAP powder with different droplet volumes is shown in Figure 4.12. APAP powder has the largest surface mean diameter (167.8 µm) and a relatively small median particle size (96 µm), which means low sphericity and a high surface area. APAP powder (contact angle of 84.2° with water) is less hydrophilic than MCC (contact angle of 45.6°) and slightly less hydrophilic than LMH (contact angle of 82.7°) powders. This results in a longer granulation process; for example, the impaction stage for APAP lasts for 130 ms, the attaching stage is from 130 ms to 1000 ms, and the spreading stage is from 950 ms to 3000 ms. Thus, the duration of the three stages for APAP is significantly longer than that for the LMH and MCC powders, as discussed earlier in this section.

The time-extension effect of the droplet volume on granulation of the APAP powder is more obvious than that of the LMH and MCC powders. As illustrated in Figure 4.12a3-4, the droplet remains stable for more than 6000 ms during the attaching stage when the droplet volume is 10 µl. When the droplet volume increased to 15 µl, the attaching stage is shortened to around 1000 ms.

The overall effect of the droplet volume on the granulation is that the smaller the droplet is, the longer the impaction and attaching stages are.

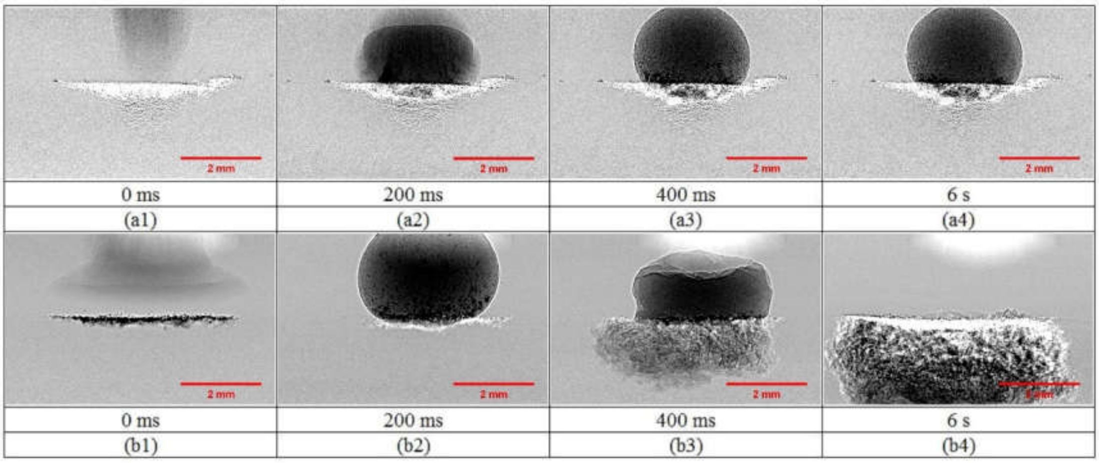

0 ms (a1) 200 ms (a2) 400 ms (a3) 6 s (a4)

0 ms (b1) 200 ms (b2) 400 ms (b3) 6 s (b4)

Figure 4.12 Time sequence X-ray images of the granulation process for APAP powder with water as a liquid binder released from 2.5 cm at volumes of (a1-a4) 10 µl and (b1-b4) 15 µl.

4.4.5 Effect of particle size

Particle size is one of the most important parameters in many powder processing operations. The effect of the particle size on granulation mainly reflects in the contact area and the weight of a single particle. This effect was studied with two droplet release heights of 15 cm and 2.5 cm. As expected, decreasing the particle size will increase the contact surface between particles. For example, the contact surface area of the MCCF powder is around 4.6 times of that for the MCC powder with the same unit mass, and the contact surface area of the LMHF powder is around 3.1 times of that for the LMH powder. Larger contact surface area results in the capillary force increasing at the same scale [93]. Thus, when the particle size decreases, liquid tends to attach to the droplet surface and then gets sucked into the liquid in the initial stage, which is the tunneling mechanism. The mean value of the overall movement ratio, r_m, is 1.28 for the MCC powder and 0.24 for the MCCF powder during the time period from 0 ms to 400 ms, which suggests that the liquid tends to move more in the vertical direction within the MCC powder bed compared to within the MCCF powder bed.

The comparison of the granulation processes between MCC (d_s=164 μm) and MCCF (d_s=30 μm) powders with different particle sizes is shown in Figure 4.13. The granulation process of MCC powder is the spreading mechanism, and MCCF powder is the tunneling mechanism, as expected, based on their particle sizes [92]. Due to the small particle size of the MCCF powder, the capillary force is larger compared with that of the MCC powder when the droplet just contacts the powder bed. The MCCF powders are attached to the droplet surface and then sucked into the droplet. The droplet and MCCF granule then tunnels into the bed.

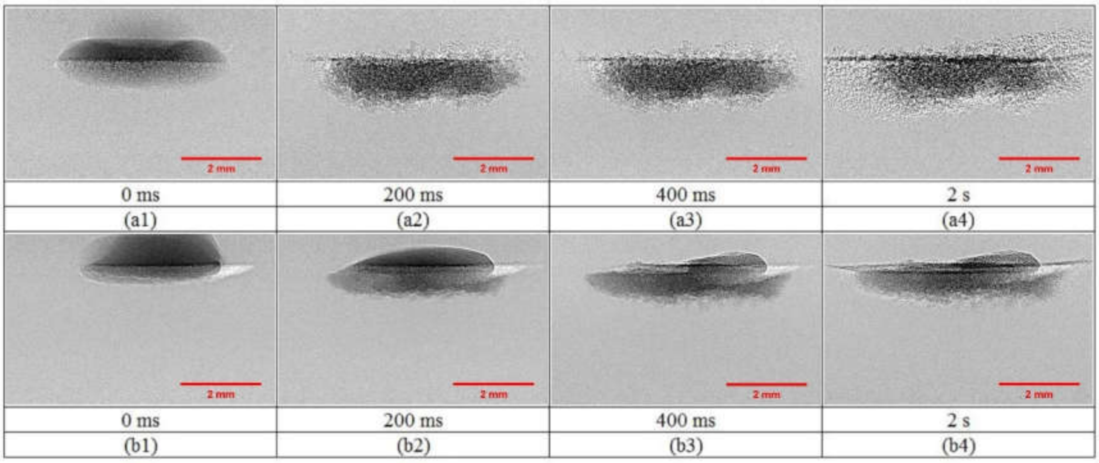

Figure 4.13 Time sequence X-ray images of the granulation process for MCC (a1-a4) and MCCF (b1-b4) powders with water as a liquid binder with 10 μl volume and 2.5 cm height.

Comparing Figures 4.13a1 with 13b1, it can be seen that during the impaction stage, the droplet with the MCC powder of a coarse particle size is flatter (d_d/h_d=7.3-17.0) than with MCCF powders (d_d/h_d=2.9-5.2). The attaching stage of the MCCF powder is longer than that of the MCC powder, as shown in Figures 4.13a2 and 13b2, due to the contact angle and particle size differences. The entire granulation process of the MCC powder is completed within 200 ms, and that of the MCCF powder finishes within 400 ms. The final granules, as shown in Figures 4.13a4 and 4.13b4, reveal that the final granule of the MCC powder (d_g/h_g=5.5) is flatter than the MCCF powder

($d_g/h_{g=}$3.8) with a smaller particle size.

When a droplet is released from 15 cm, the effect of the particle size on granulation is found to be different from that at a lower release height. The dynamic images of the granulation process of MCC and MCCF powders are shown in Figure 4.14. As can be seen from Figure 4.14a1, the droplet impacts on the MCC bed surface and rebounds within 68 ms. Then, the liquid droplet is covered with MCC powder and forms a crater, and a boat-shaped granule is formed, as shown in Figure 4.14 a4. For the MCCF powder, as shown in Figure 4.14b1, a crater is formed when droplet impacts on the MCCF powder bed. Then, the process can be classified as the tunneling mechanism [92]. The fine powders attach to the droplet surface and the whole droplet gradually penetrates the powder bed as a stable sphere shape from 68 to 400 ms (see Figures 4.14b2 and 14b3). The water starts spreading at the bottom of the granule around 400 ms, when the attaching stage ends, as can be seen in Figure 4.14b3.

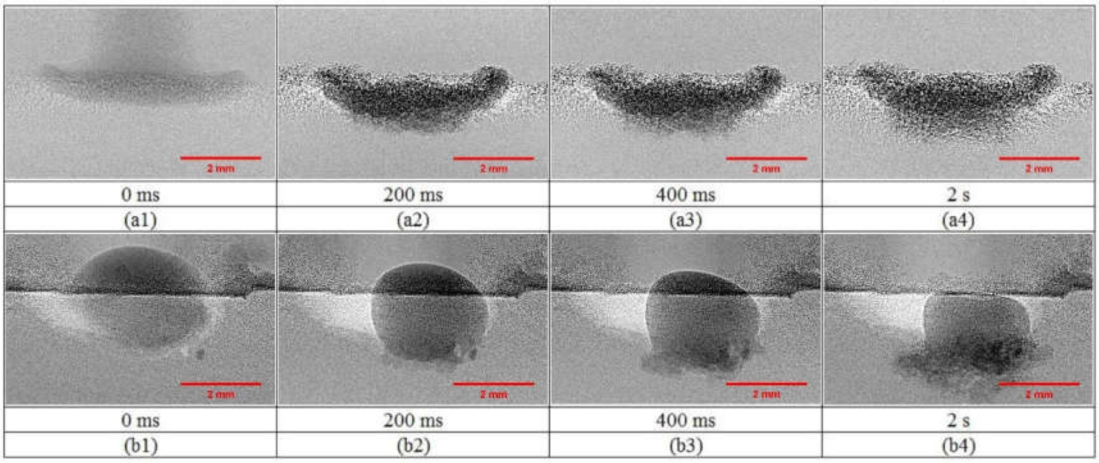

Figure 4.14 The time sequence X-ray images of the granulation process of MCC (a1-a4) and MCCF (b1-b4) powders with water as a liquid binder with 15 µl volume and 15 cm height.

4.5 Conclusions

The dynamic granulation process for pharmaceutical powders was experimentally studied through in-situ synchrotron-based X-ray imaging techniques. This study demonstrated the high potential of applying in-situ synchrotron X-ray imaging to quantitatively study the dynamic wet granulation process with a single drop impacting method. The liquid movement beneath the powder bed surface and the interaction between the pharmaceutical powders and liquid binder were observed with high speed and high-resolution images. The following conclusions can be drawn from the current experimental results:

The particle properties, including size and hydrophilicity, and liquid properties, including droplet volume and release height, have significant influences on the granulation process. For coarse powders, granulation processes with droplets released at a lower height result in the spreading mechanism, whereas the processes with higher droplet release heights result in the crater formation mechanism. Decreasing the particle size leads to the tunneling mechanism, and the resultant final granules are rounder than those generated with powders of a larger particle size. The pharmaceutical powder with low sphericity has larger median particle size, which results in spreading mechanism. Larger contact angle means higher hydrophobicity, which leads to a longer penetration and spreading time.

The overall movement ratio, r_m, was introduced to quantitatively describe the liquid movement during the granulation process. When the overall movement ratio, r_m, is larger than 1, the liquid moves faster in the vertical direction, and this can be described as penetration. When the overall movement ratio, r_m, is smaller than 1, the liquid moves faster in the radial direction, which is spreading.

CHAPTER 5. DRYING PERFORMANCE OF PHARMACEUTICAL GRANULES IN A PULSATION-ASSISTED FLUIDIZED BED DRYER

The content of this chapter will be submitted to a journal for publication.

Contribution of the Ph.D. student:

The experiments were planned and performed by Chen Li. Lifeng Zhang supervised and provided consultation during the experiment preparation, data analyzing, and thesis preparation. The writing of the thesis was done by Chen Li, with Lifeng Zhang providing editorial guidance.

Contribution of this chapter to the overall study

This chapter studies the drying process during the pharmaceutical tablet manufacturing process. Pulsed airflow was used to enhance fluidization and eliminate channeling. This study provides a good understanding of the effect of important operating conditions, including superficial gas velocity, air temperature, pulsation frequency, and pulsed air ratio on drying curve as well as energy efficiency. These results are essential for optimizing the pulsed fluidized bed drying process.

5.1 Abstract

Fluidized bed drying has been widely employed in pharmaceutical manufacturing processes. Due to considerable cohesiveness resulting from the presence of moisture within pharmaceutical granules, agglomeration and channeling phenomena pose significant challenges on fluidization and drying, particularly at the beginning of the drying process. In this work, the drying performance of pharmaceutical granules was investigated in a pulsation-assisted fluidized bed dryer. The drying rate and energy efficiency were investigated with representative pharmaceutical powders, including active pharmaceutical ingredients (APIs) and under pulsation frequency 1.5-6.0 Hz, superficial gas velocity 1.0-1.8 m/s, inlet gas temperature 40-60℃, and pulsed air ratio 0-50%.

It is found that the pulsed airflow is effective in eliminating channeling and enhancing the drying rate at higher superficial gas velocity. A lower pulsation frequency, namely 1.5 Hz, is more favourable to improve the drying rate. During the constant rate period, energy efficiency is between 60% to 45% for the drying process while the energy efficiency decreases to 10% during the falling rate period. A pulsed fluidized bed dryer has shown a higher energy efficiency than a conventional one with the constant gas flow. Among nine thin-layer drying models examined in this work, the Midilli and Kucuk model has shown the best agreement between the experimental data and the predicted results.

5.2 Introduction

Drying is an essential unit operation in the chemical, pharmaceutical and food industries [110]. It is commonly used to remove moisture in products to extend shelf life, decrease product weight, and ensure stability [42, 111]. Industrial drying of solids is one of the energy-intensive unit operations [112]. For example, energy consumed during the drying consists of up to 70% of the total energy in manufacturing most wood products, about 50% of finished textile fabrics, 27% of paper, and 33% of pulp production [113]. Optimization of the drying process operating conditions is needed to increase energy efficiency, thereby reducing the production costs. Fluidized bed drying is one of the most commonly used methods due to its large heat transfer area, relatively uniform bed temperature, ability to be operated at a relatively low temperature, and high heat transfer efficiency [114].

In the pharmaceutical industry, wet pharmaceutical powders have a strong tendency to form agglomerations [115]. The agglomerations pose significant challenges to fluidization, like channeling and by-passing [116, 117]. Several methods have been developed to improve fluidization quality and eliminate channeling during the drying process of wet or cohesive powders. In general, these methods can be classified into three categories, namely, gas stream relocation [118, 119], vibration of the bed layer [120, 121], and particle properties modification [122, 123]. The gas stream relocation can be generated by a rotating disk before a gas distributor or a valve that can be periodically open and close. The advantage of this method is that it can be easily modified on a conventional FBD and can be controlled during the drying process. Adding a vibratory base to fluidized beds is found effective in eliminating channeling. However, the vibration has a negative influence on the life of the equipment and may cause safety concerns in process scale-up. Modification of particle properties can enhance the fluidization mainly by adding particles with larger size to increase the average particle size of the mixture. In the pharmaceutical industry, which has strict ingredient requirements, adding additional particles is not acceptable.

A fluidized bed dryer (FBD) with inlet gas relocation is also known as a pulsed fluidized bed dryer (PFBD) [119]. Compared with an FBD with a constant gas flow, a PFBD has an intermittent gas flow, which leads to lower average flow rates and higher peak pressures [124]. A lower gas flow rate typically results in a slower drying rate [125]. However, pulsed air can help to break agglomerates, which increases the total contact area between drying air and wet particles [126]. For the drying processes dominated by contact surfaces between drying air and solid particles, the surface moisture evaporation is the primary drying step, and the drying rate is constant during this period. Pulsed airflow has a direct impact on the bubble size, with the average diameter of bubbles in a PFBD being found to be smaller than that of those in a conventional FBD. The smaller bubble size was attribute to the increased number of bubbles and the absence of coalescence due to the pulsating part of the fluidization gas [125, 127]. The smaller bubbles in a PFBD also have a longer residence time than that in a conventional FBD, which subsequently enhances heat and mass transfer rates [128]. A PFBD is also found to show a higher bed expansion ratio and a lower bed fluctuation ratio, which is defined as the maximum bed height to the minimum bed height [127]. In light of the advantages of superior heat and mass transfer, PFBDs have been increasingly employed as industrial drying operations, including sugar [129], rice [130], pharmaceutical granule [119, 131], and biomass [132, 133].

Most current studies of PFBDs placed emphasis on operating conditions of air temperature [124, 134, 135], flow rate [126, 136], and superficial gas velocity [137, 138]. Other critical parameters, including pulsation frequency and pulsed air ratio, and the effects of these key operating parameters on drying rate and energy efficiency have not been thoroughly investigated. In addition, most of the current studies of FBD for pharmaceutical powders used just excipients. Adding active pharmaceutical ingredients (APIs) to the mixtures might yield different granule characteristics such as granule size, granule shape, and granule density [95, 139]. Therefore, it is pivotal to understand the drying behaviour of pharmaceutical granules in a PFBD using representative mixtures, including APIs. Hence, the objectives of this study were to investigate the effects of important operating parameters, including superficial gas velocity, inlet air temperature, pulsation, and pulsed air ratio on the drying performance and energy efficiency of a PFBD.

5.3 Materials and methods

5.3.1 Material characterization and preparation

In the experiments, wet pharmaceutical granules were prepared based on pre-determined compositions of a typical formulation, as shown in Table 5.1. The initial moisture content was 31 ± 1 % on a wet basis (wb). The dry pharmaceutical powders were stored in a chamber with a constant temperature of 24 °C and relative humidity (RH) of 30% for 48 hours. Then, the dry pharmaceutical powders were sieved through a 2.00 mm sieve and mixed with a 250 W low-shear granulator (Kitchen-Aid classic mixer) for 2 minutes at the lowest speed (setting 1). Deionized water was gradually added at a flow rate of 59 mL/min for 5 minutes, then followed by a higher speed (setting 2) mixing. Afterward, the mixture was sieved through a screen with the size of an opening of 3.36 mm [140]. The wet granules were sealed in a bag and stored in the chamber (kept at 24 °C) for 1 hour to ensure uniformity of moisture content and temperature distribution.

Table 5.1 Mass percentage of pharmaceutical powders in the mixture

Component	Function	Percentage by mass (wet basis)
Acetaminophen (APAP)	API	13%
Lactose monohydrate (LMH)	Filler	28%
Microcrystalline cellulose (MCC)	Filler	25%
Hydroxypropyl methylcellulose (HPMC)	Binder	3%
Croscamellose sodium (CCS)	Disintegrant	1%
Water	Solution binder	30%

The characterization of the powder materials, including median particle size, skeletal particle density, and particle bulk density, used in this study is presented in Table 5.2. The median particle size was measured with a Malvern 2000 Mastersizer S (Malvern Instruments, UK). Particle skeletal density was determined by an Ultrapycnometer 1000 (Quantachrome Instruments, Austria).

Table 5.2 Physical properties of pharmaceutical powders

Component	Median particle size, d_{50} (μm)	Particle skeletal density, ρ_p (g/cm^3)	Particle bulk density, ρ_{bed} (g/cm^3)	Supplier
APAP	96	1.72	0.57	Hebei Jiheng Pharmaceutical
LMH	70	1.52	0.56	Foremost Farms
MCC	128	1.61	0.36	FMC BioPolymers
HPMC	82	1.56	0.52	DOW Chemical Company
CCS	41	1.62	0.54	FMC BioPolymers

5.3.2 Pulsed fluidized bed dryer setup

The schematic description of the experimental set-up is shown in Figure 5.1.

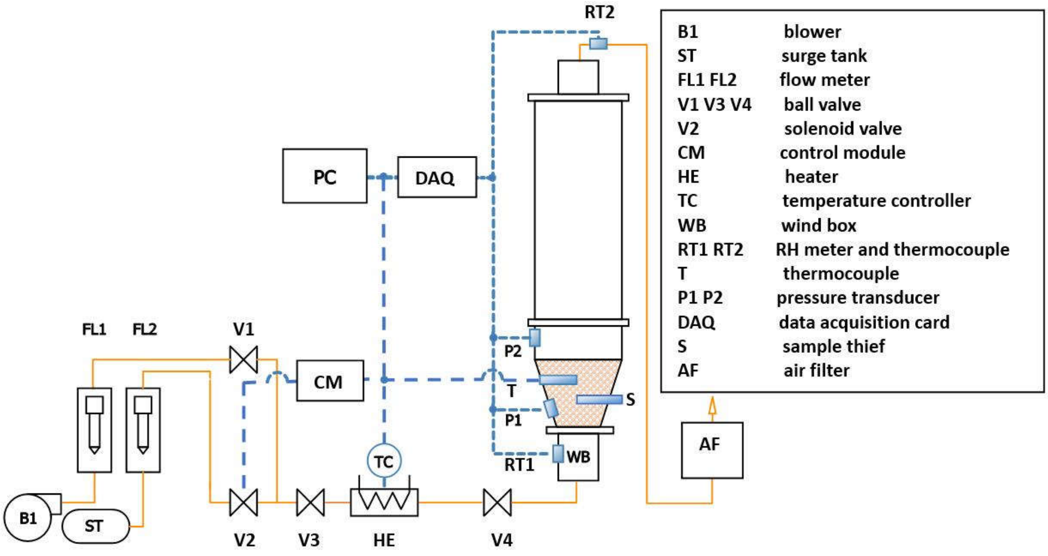

Figure 5.1 Schematic drawing of the pulsed fluidized bed dryer.

The whole fluidized bed dryer consists of two sections: a conical-shaped production bowl and a cylindrical freeboard section. The location of the sample thief and the dimension of the product bowl and sample are shown in Figure 5.2. The conical-shaped product bowl has an inclination angle of 25°. The top of the product bowl has a diameter of 25 cm, while the bottom has a diameter of 11.5 cm. The conical geometry enhances solid circulation and mixing. The solid can be transported upward in the central region, and solid can return to the bottom at the area close to the walls. The cylindrical freeboard section has a height of 1.53 m. The loading height with wet pharmaceutical granules in the production bowl was 22 cm, while the bed height of dry pharmaceutical granules was found to be 12 cm. The sample thief is made of Teflon (PTFE). The sample thief can load around 3 grams of pharmaceutical granules every time. The hole in the sample thief has a length of 4 cm, a width of 1 cm and a depth of 1 cm. The air distributor has an overall opening ratio of 5.6%.

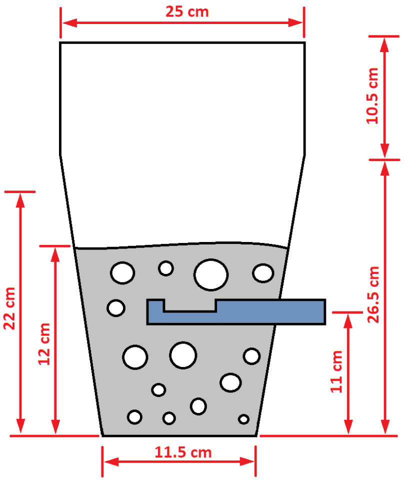

Figure 5.2 Dimensions of the product bowl and the location of the sample thief.

The continuous gas stream was provided by a rotary blower (SCL V4, Effepizela, Italy). The pulsed gas stream was supplied from building air, which contains a surge tank with compressed air. The airflow rate was controlled separately with ball valves (Midline ball valve, Everflow, USA). The pulsation was generated by a solenoid valve (8210, ASCO, USA). The response time of the solenoid valve from fully close to fully open is 50 to 75 ms. The actuation of the solenoid valve was controlled by a LabVIEW program. The "ON" and "OFF" statuses of the valve and the duration of the two statuses were controlled separately. The pulsation was set at frequencies of 1.5, 3.0, and 6.0 Hz. Pulsation frequency within this range was reported to be effective in enhancing the fluidization of granules with high moisture content [138, 141].

The drying air was heated by an electrical heater (BEN24G6S, Watlow, USA), and the air temperature was controlled by a temperature controller (CN7500, Omega, USA). The inlet air temperature was set at 40, 50, and 60°C. The temperature range (40 to 60 °C) was chosen to simulate industrial operating conditions for typical heat-sensitive materials.

The relative humidity (RH) and temperature of the air were monitored by RH meters, and thermocouples (HX93BDV2-RP1, Omega, USA) installed at the wind box and the outlet of the fluidized bed dryer. The differential pressure was measured with pressure transducers (PX137-

0.3DV, Omega, USA) installed at the product bowl and the freeboard section. The pressure transducers were calibrated before being installed. Two layers of fine stainless-steel mesh were attached to the pressure sampling ports to prevent fine powers from entering.

A data acquisition board (DT 9829, Data Transformation, USA) was used to collect and convert analog voltage signals collected from the pressure transducers, RH meters, and thermocouples. The sampling frequency was set at 200 Hz

5.3.3 Drying experiment procedure

Before each run, operating conditions in the PFBD was adjusted to reach pre-set operating conditions such as average superficial gas velocity (1.0, 1.4, and 1.8 m/s), gas temperature (40, 50, and 60℃), pulsed air ratio (0, 10, 20, 30, 40, and 50%), and pulsation frequency (1.5, 3.0 and 6.0 Hz) to shorten the preheat time. Then, 2.0 kg of wet pharmaceutical granules were loaded into the product bowl. One set of experiments were conducted five times with a superficial gas velocity of $5.6U_{mf}$, an air temperature of 50℃, a pulsation frequency of 1.5 Hz, and a pulsed air ratio of 20% to show reproducibility.

Approximately 3 g granules samples were taken from the central part of the product bowl every 5 minutes by a sampling thief. Moisture content was measured by a drying balance (HB43, Mettler-Toledo, USA). The presence of moisture in the pharmaceutical powders significantly affects the minimum fluidization velocity (U_{mf}). In this work, U_{mf} was measured based on standard pressure drop against superficial gas velocity method. U_{mf} at the initial moisture content 31 wt %. was found to be 0.45 m/s while U_{mf} at the final moisture content of 5 wt % was 0.08 m/s. An average value of 0.25 m/s was taken among values measured at four moisture contents as the minimum fluidization velocity. Two superficial gas velocities, 1.0 m/s (4.0 U_{mf}) and 1.4 m/s (5.6 U_{mf}) were employed in this work. The moisture content was normalized to have a moisture ratio (Φ), defined by

$$\Phi=X/X_0 \tag{5.1}$$

where X is the moisture content of pharmaceutical granules (wt %) at any instant and X_0 is the initial moisture content of pharmaceutical granules (wt %).

Drying rate is defined as grams of water removed per unit mass of dry pharmaceutical powder per minute.

$$\dot{m}=dM/dt \tag{5.2}$$

The water removed can be determined based on the moisture content measured. The net weight of the dry materials loaded into the product bowl was 1.40 kg. After the drying operation, the final dried materials were weighted from 1.30 to 1.32 kg. The subtle difference is due to mass losses from sampling and fine particle entrainment.

5.3.4 Energy efficiency

The energy efficiency of the drying process is defined as the ratio between the energy used for the evaporation of water and the input energy [142-144]. The energy efficiency can be evaluated by:

$$\eta = \frac{\triangle H_{vap} \triangle M}{C_p U A \rho_{air} (T_{in} - T_{out}) t} \tag{5.2}$$

where $\triangle H_{vap}$ is the latent heat of water vaporization, which is 2260 kJ/kg; ΔM is the weight of water removed within wet pharmaceutical granules in the product bowl; C_p is the specific heat capacity of air, which is 1.00 kJ/kg·K; U is the superficial gas velocity; A is the cross-section area of the bottom of the conical product bowl; ρ_{air} is the density of air; T_{in} is the inlet gas temperature; T_{out} is the outlet gas temperature; t is the total drying time.

5.3.5 Thin-layer drying modelling

Thin-layer drying modeling was chosen to predict the drying curve due to their high accuracy and ease of use. In this work, nine thin-layer drying models were examined. In order to employ these thin-layer models, the following assumptions are made for the conventional FBD and PFBD:

(1) The granules are assumed to be spherical, uniform in size and shape, homogenous and isotropic.

(2) The shrinkage of granules during drying is not significant.

(3) The moisture distribution of granules is uniform and symmetrical during the course of the drying process.

(4) The temperature of the granules is the same as that of the air in the fluidized bed.

(5) Evaporation takes place at the surface of the granules.

(6) The changes of the air properties are negligible.

(7) Heat transfer is by conduction within the granules and by convention outside of the granules [145].

Three statistical parameters, namely coefficient of determination (R^2), chi-square (χ^2), and root mean square error (RMSE) were used to assess the goodness of curve fitting.

$$\chi^2 = \frac{\sum_{i=1}^{N}(MR_{exp,i} - MR_{pre,i})^2}{N-z} \tag{5.3}$$

$$RMSE = \left[\frac{1}{N}\sum_{i=1}^{N}(MR_{exp,i} - MR_{pre,i})^2\right]^{1/2} \tag{5.4}$$

where i is the order of sample, N is the total number of samples, $MR_{exp,i}$ is the experimental moisture ratio, and $MR_{pre,i}$ is the predicted moisture ratio [146].

Microsoft Excel (Microsoft Office 365, USA) was used to solve the coefficients and constants with minimizing chi-square using the generalized reduced gradient method [147]. These nine models are presented in Table 5.3 below.

Table 5.3 Thin-layer drying models tested for drying curve prediction

Model number	Model name	Equation	Reference
1	Newton	$MR=\exp^{(-k*t)}$	[148]
2	Henderson and Pabis	$MR=a*\exp^{(-k*t)}$	[149]
3	Page	$MR=\exp^{(-k*t^{n})}$	[150]
4	Logarithmic	$MR=a*\exp^{(-k*t)}+c$	[151]
5	Two term	$MR=a*\exp^{(-k*t)}+c*\exp^{(-g*t)}$	[152]
6	Two term exponential	$MR=a*\exp^{(-k*t)}+(1-a)*\exp^{(-k*a*t)}$	[149]
7	Verma et al.	$MR=a*\exp^{(-k*t)}+(1-a)*\exp^{(-g*t)}$	[153]
8	Midilli and Kucuk	$MR=a*\exp^{(-k*t)}+b*t$	[154]
9	Hii et al.	$MR=a*\exp^{(-k*t^{n})} +c*\exp^{(-g*t^{n})}$	[146]

where a, b, e, g, k, n are coefficients used in the thin-layer drying models.

5.3.6 Uncertainty analysis

In order to determine the relative error, the drying experiments at the superficial gas velocity $5.6U_{mf}$ with an air temperature of 50°C, a pulsation frequency of 1.5 Hz and a pulsed air ratio of 20%. The relative errors are 2.2% for conventional FBD and 2.8% for PFBD.

The Student t-test was applied to analysis the significant difference ($P<0.05$) among the mean samples between the conventional FBD and the PFBD with different pulsation frequencies at a 95% confident level. The independent variable with a smaller P-value has a more significant effect on the response. The Student t-test was conducted using Excel (Microsoft Office 365, USA).

5.4 Results and discussion

5.4.1 Effect of pulsation

High moisture content within pharmaceutical granules makes the solid particles cohesive, which poses challenges to smooth fluidization. Agglomerates formed due to cohesiveness also reduce gas-solid contact, and the drying air can only pass the bed through channeling. Therefore, the drying rate will be considerably reduced. The quality of the products is also negatively influenced as granules around the channeling region are over-dried while granules in other areas are still wet due to limited direct contact area with air.

The pulsation is expected to enhance the drying rate by increasing the solid-gas contact area. When the dominant parameter of the drying process is superficial gas velocity, applying pulsed air will not enhance the drying rate, rather than decrease the average airflow rate. It also can be expected that the low pulsation amplitude cannot overcome the inter-particle forces in wet pharmaceutical granules.

The effect of pulsation on drying is shown in Figure 5.3. It can be seen that gas pulsation can enhance drying and decrease the drying time from 80 minutes to 75 minutes at the superficial gas velocity of $5.6U_{mf}$. However, this enhancing effect is not observed at a lower superficial gas velocity ($4.0U_{mf}$). Instead, a shorter drying time (90 minutes) is found in the conventional FBD, compared to that in the PFBD (105 minutes).

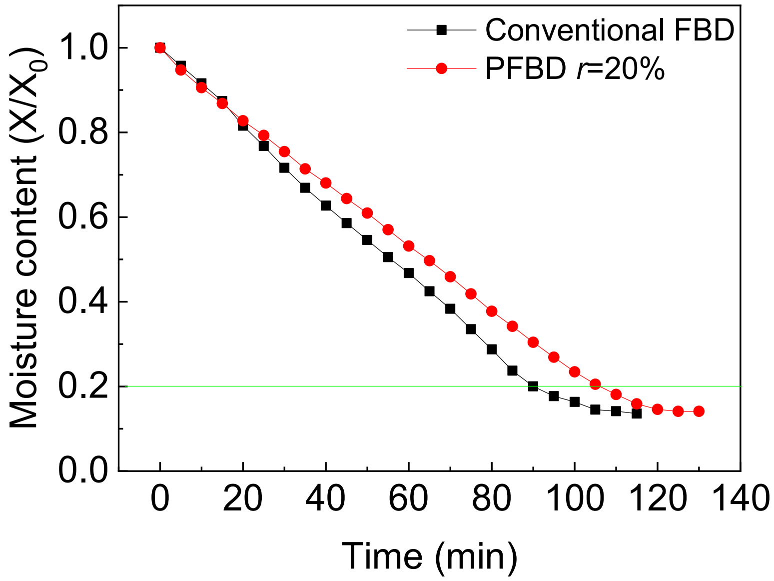

(a)

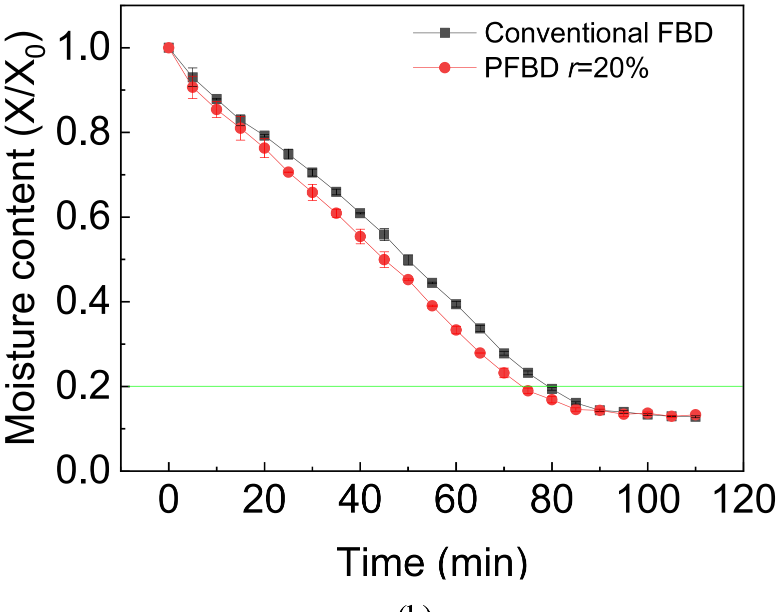

(b)

Figure 5.3 Effect of pulsation on drying (a) U=4.0U_{mf}, (b) U=5.6U_{mf} with T=50°C, f=1.5 Hz and r=20%.

The drying rate is presented in Figure 5.4. At the low superficial gas velocity (4.0U_{mf}), the drying rate of the pulsed fluidized bed is lower than the conventional fluidized bed dryer. Under the higher superficial gas velocity (5.6U_{mf}), the drying rate in the PFBD is slightly higher than that in the FBD at the constant rate drying period, as shown in Figure 5.4 (b). For the PFBD, when 20% of the total airflow is pulsed flow, the other 80% is continuous flow. At the lower superficial gas velocity, the continuous airflow is not high enough to keep the bed at the minimum fluidization status when the materials are wet. The "off" period of pulsed air, in fact, decreased the average airflow rate. When increasing the superficial gas velocity from 4.0U_{mf} to 5.6U_{mf}, the continuous airflow can maintain the bed fluidized, and the other 20% pulsed air enhances mixing and eliminates channeling in the initial period of the drying process.

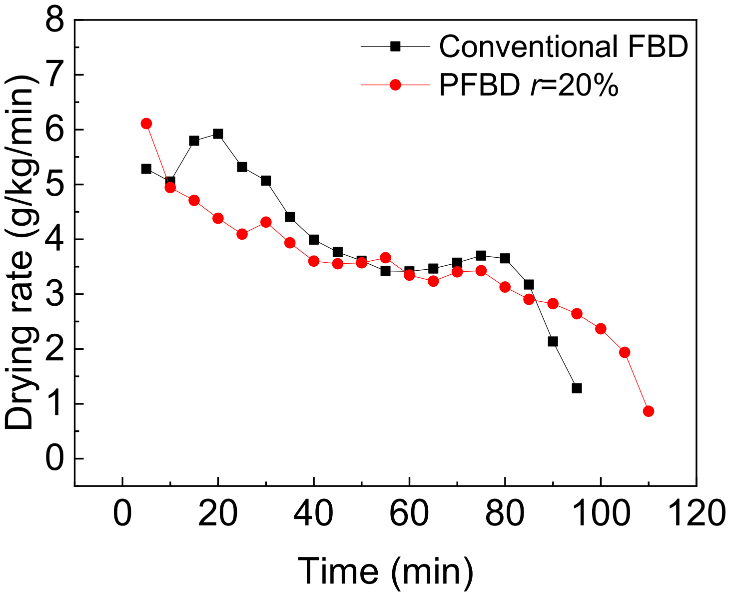

(a)

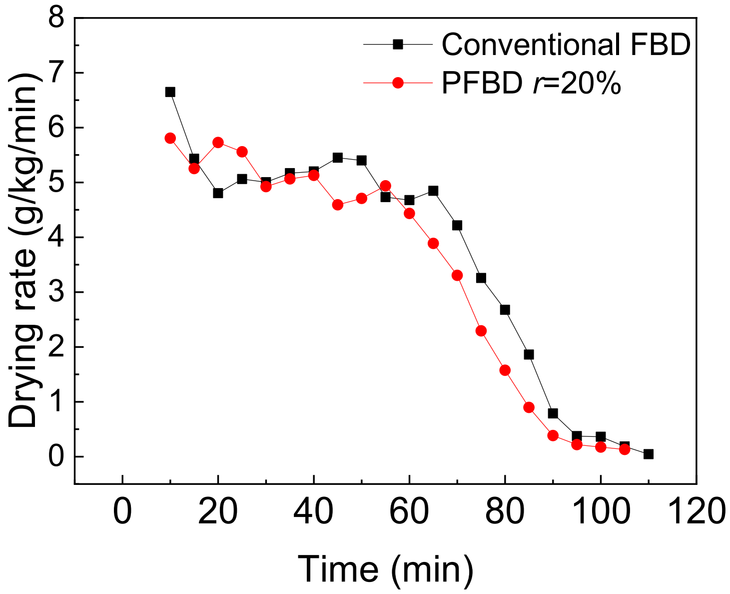

(b)

Figure 5.4 Effect of pulsation on drying rate (a) U=4.0U_{mf}, (b) U=5.6U_{mf} with T=50°C and f=1.5 Hz.

The average pressure drop (*p*), peak pressure drop (Δp), and standard deviation (σ) of the pressure drop measured in both the PFBD and the conventional FBD are shown in Table 5.4. It can be seen that the PFBD at a low pulsation frequency has the highest average pressure drop (1.21 kPa), peak pressure drop (1.87 kPa), and standard deviation (0.35 kPa), which means low-frequency pulsed air can break agglomerates more easily than high-frequency pulsed air and the conventional FBD.

Table 5.4 Pressure of the conventional FBD and PFBD with U=5.6U_{mf} and an air temperature of 50°C

Operating condition	Average pressure drop, *p* (kPa)	Peak pressure drop, Δp (kPa)	Standard deviation, σ (kPa)
PFBD at 1.5 Hz	1.21	1.87	0.35
PFBD at 3.0 Hz	0.46	0.73	0.13
PFBD at 6.0 Hz	0.39	0.62	0.09
Conventional FBD	0.44	0.67	0.11

During the experiments, the air temperatures at the inlet, the outlet, and the fluidized bed were monitored. The curves are shown in Figure 5.5. It can be seen that the inlet air is kept constant at around 50°C during the entire drying process. The outlet air temperature decreases in the first 10 minutes, corresponding to the preheating of wet granules. When the solids are loaded in the product bowl, the heat transfers from hot air to the wet granules. The temperature difference between the hot air and the wet granules drives the mass transfer of water from wet granules to air.

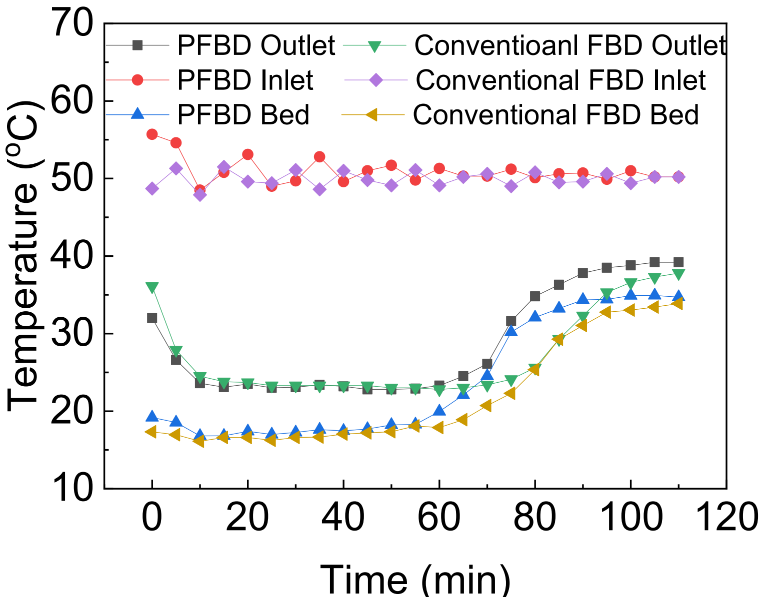

Figure 5.5 Inlet air, outlet air and fluidized bed temperature during the drying process of the conventional FBD and the PFBD with U=5.6U_{mf} , f=1.5 Hz, and r=20%.

The relative humidity (RH) of the inlet and outlet air is shown in Figure 5.6. The RH of the outlet air increases with the moisture content removal from the granules. The outlet air temperature and the bed temperature keep constant during the constant rate drying period. Afterwards, the temperatures of the outlet air and the fluidized bed start to increase. The fluidized bed temperature is always lower than that of the outlet air due to water evaporation, taking place at the surface of wet granules.

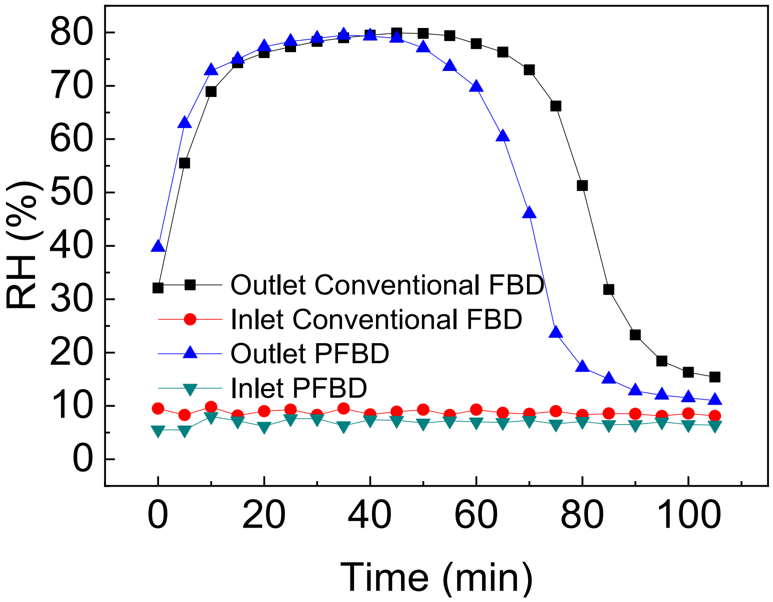

Figure 5.6 Inlet air and outlet air relative humidity during the drying process of the conventional FBD and the PFBD with U=5.6U_{mf} , f=1.5 Hz and r=20%.

The energy efficiency of the conventional FBD and the PFBD is shown in Figure 5.7. It can be seen that during the constant drying rate period, energy efficiency is between 60% to 45%, which is consistent with the values (60%-40%) reported in the literature [143]. During the falling rate period, the energy efficiency falls from 45% to 10%. During the constant rate period, both the drying rate and the energy input rate remain constant. The water that remains in the wet pharmaceutical granules can be classified into bound water and unbound water (or free water). The bound water mainly exists within the porose within granules, and the unbound water mainly locates at the outside of and the surface of the granules. When the free water is removed, the energy required to motivate bound water movement within granules is increased, while the energy required for evaporation decreases due to the decreased drying rate. The input energy decreases at a slower rate than the energy required for evaporation. Thus, the energy efficiency is lower at the falling rate period.

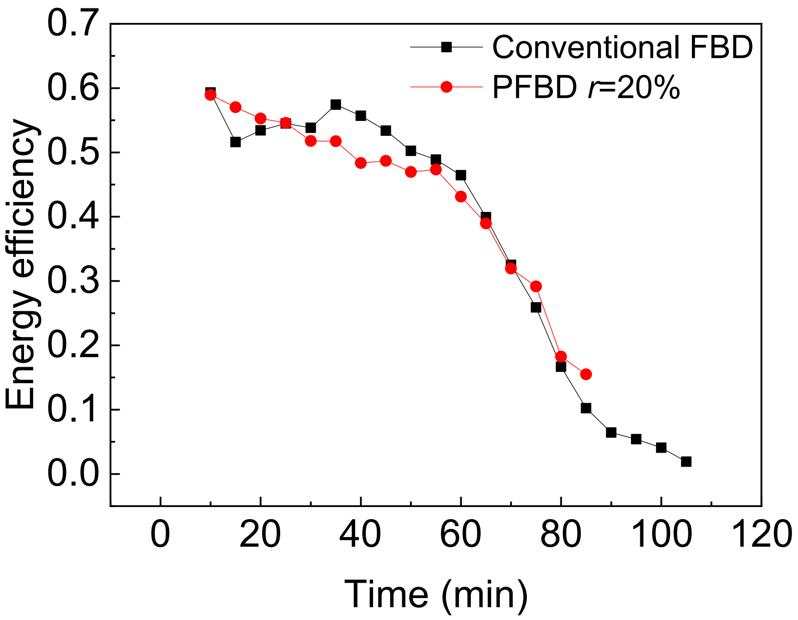

Figure 5.7 Energy efficiency of conventional FBD and PFBD with U=5.6U_{mf} and f=1.5 Hz.

5.4.2 Effect of superficial gas velocity

To study the effect of superficial gas velocity, three superficial gas velocities of 1.0 m/s, 1.4 m/s and 1.8 m/s were used in the conventional FBD, and two superficial gas velocities of 1.0 m/s and 1.4 m/s are used for the PFBD. The results are shown in Figure 5.8.

The drying time decreases with increasing the superficial gas velocity as expected. A higher superficial gas velocity enhances solid-solid mixing, solid-gas contact area, and mass transfer, and heat transfer between air and the granule surface. Therefore, the heat transfer to pharmaceutical granules and mass transfer to air is facilitated.

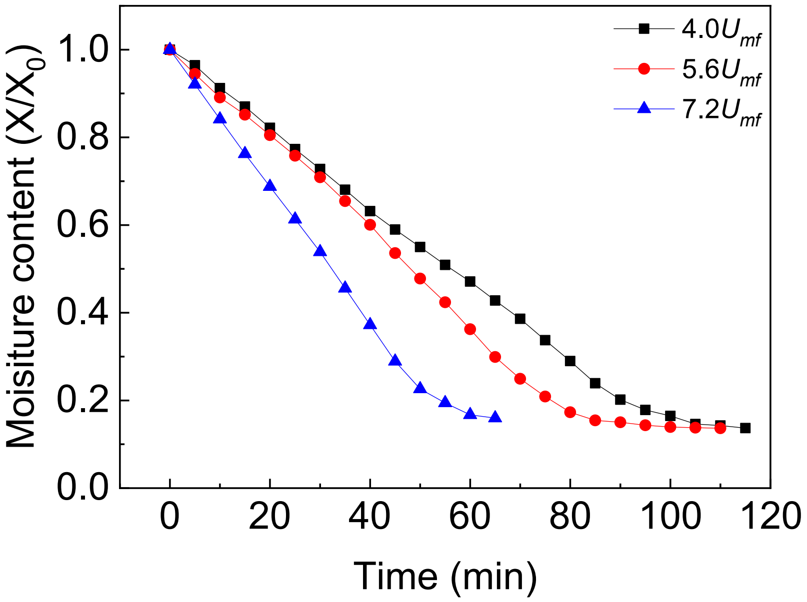

(a)

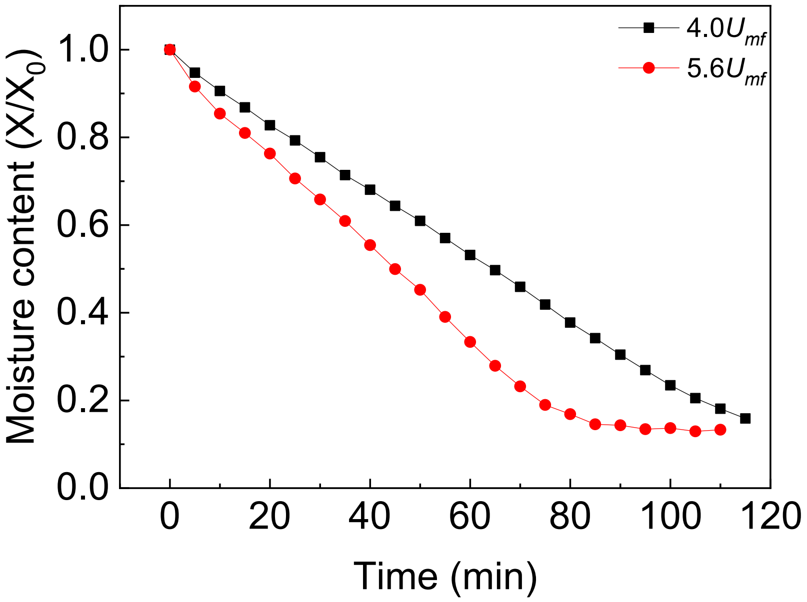

(b)

Figure 5.8 Effect of gas flow rate on drying (a) conventional FBD, (b) PFBD with T=50°C, f=1.5Hz and r=20%.

There are two drying phases that can be seen in Figure 5.8. The first one is the constant drying rate period, during which the moisture content decreases linearly with time. When the moisture content ratio drops to 0.2 (10 wb %), the drying rate falls from 5 g/kg/min during the constant rate period to 1 to 2 g/kg/min for the falling rate period. Similar phenomena were reported in other studies [155, 156].

The effect of the superficial gas velocity on the drying rate is shown in Figure 5.9. When the FBD is operated at continuous flow or pulsed flow, the drying rate increases with a higher drying air flow rate during the constant rate period. The duration of the constant rate period is also shorter at a higher superficial gas velocity.

The effect of superficial gas velocity on the energy efficiency during the drying process is shown in Figure 5.10. Higher superficial gas velocity can enhance the energy efficiency around 8% during the constant drying period for the conventional FBD, and for the PFBD, the energy efficiency can be enhanced by 15% when the superficial gas velocity increased from $4.0U_{mf}$ to $5.6U_{mf}$. Higher superficial velocity, like pulsation and vibration, can also break agglomerate and therefore increase the gas-solid contact area. The mass and heat transfer are directly related to the contact area. The energy efficiency is improved as a result of the larger contact area.

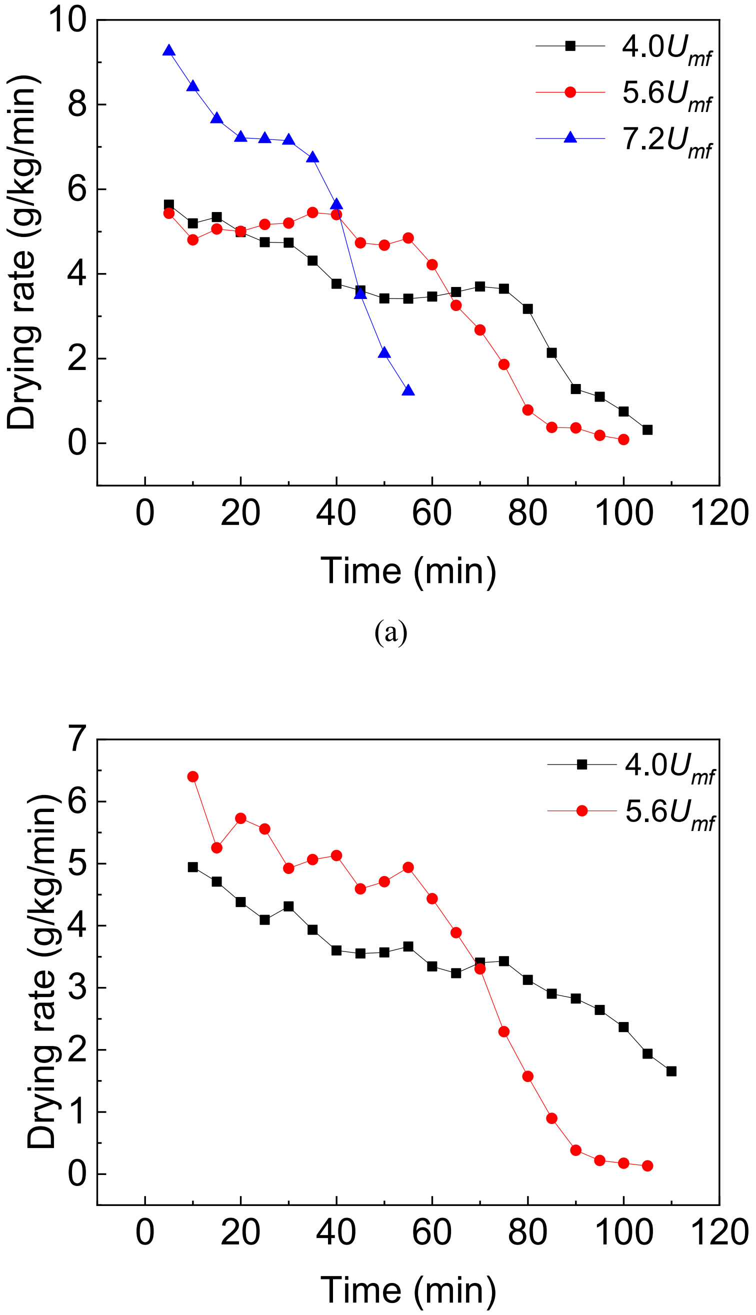

(a)

(b)

Figure 5.9 Effect of gas flow rate on drying rate (a) conventional FBD, (b) PFBD with T=50°C, f=1.5Hz and r=20%.

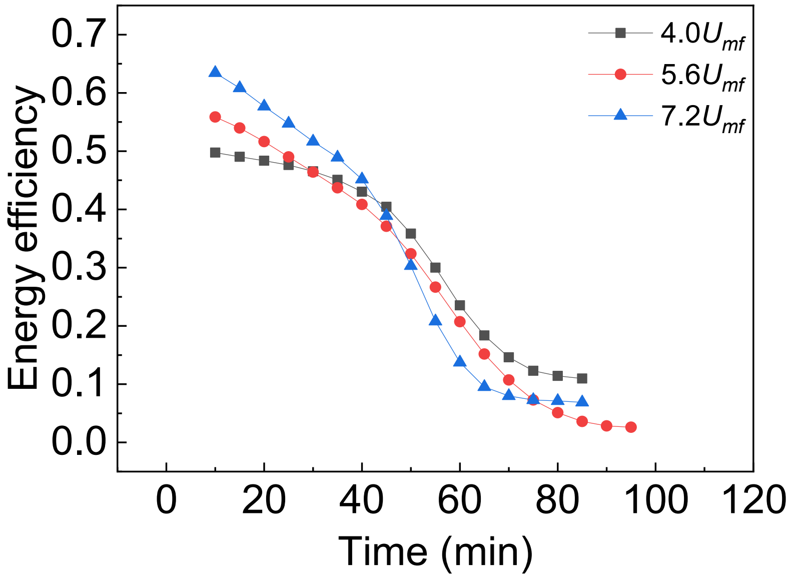

(a)

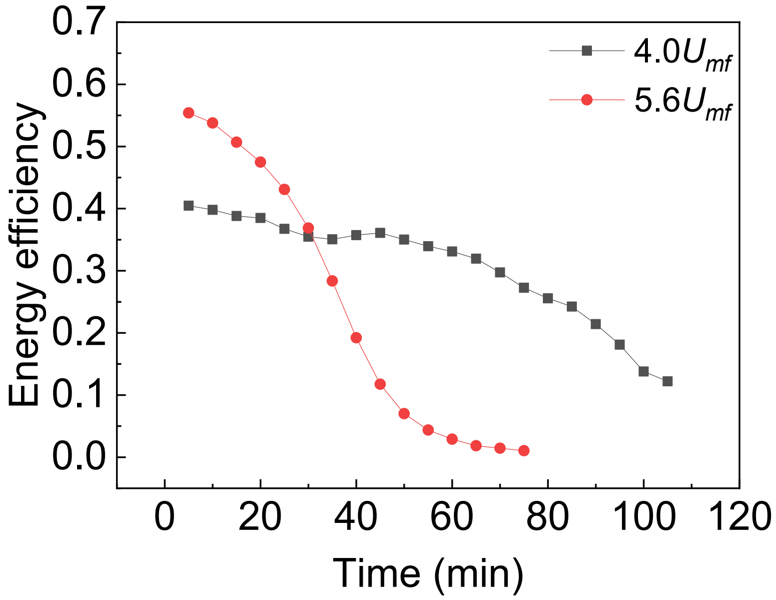

(b)

Figure 5.10 Effect of gas flow rate on energy efficiency (a) conventional FBD, (b) PFBD with T=50°C, f=1.5Hz and r=20%.

5.4.3 Effect of air temperature

The effect of the drying air temperature was studied with three temperatures (40, 50, and 60 °C), and the results are shown in Figure 5.11. Figure 5.11a is operated at continuous airflow, and Figure 5.11b is conducted with pulsed airflow at a pulsation frequency of 1.5 Hz.

The effect of the inlet air temperature on the drying rate is shown in Figure 5.12. The drying rate is generally higher at a higher operating temperature. The average drying rates during the constant rate period are 6.06, 7.28, and 10.73 g/kg/min for the inlet air temperatures of 40, 50, and 60°C, respectively, when the FBD is operated at a continuous flow. For the PFBD, the average drying rates are 6.63, 7.22, and 9.86 g/kg/min with an inlet air temperature at 40, 50, and 60°C, respectively.

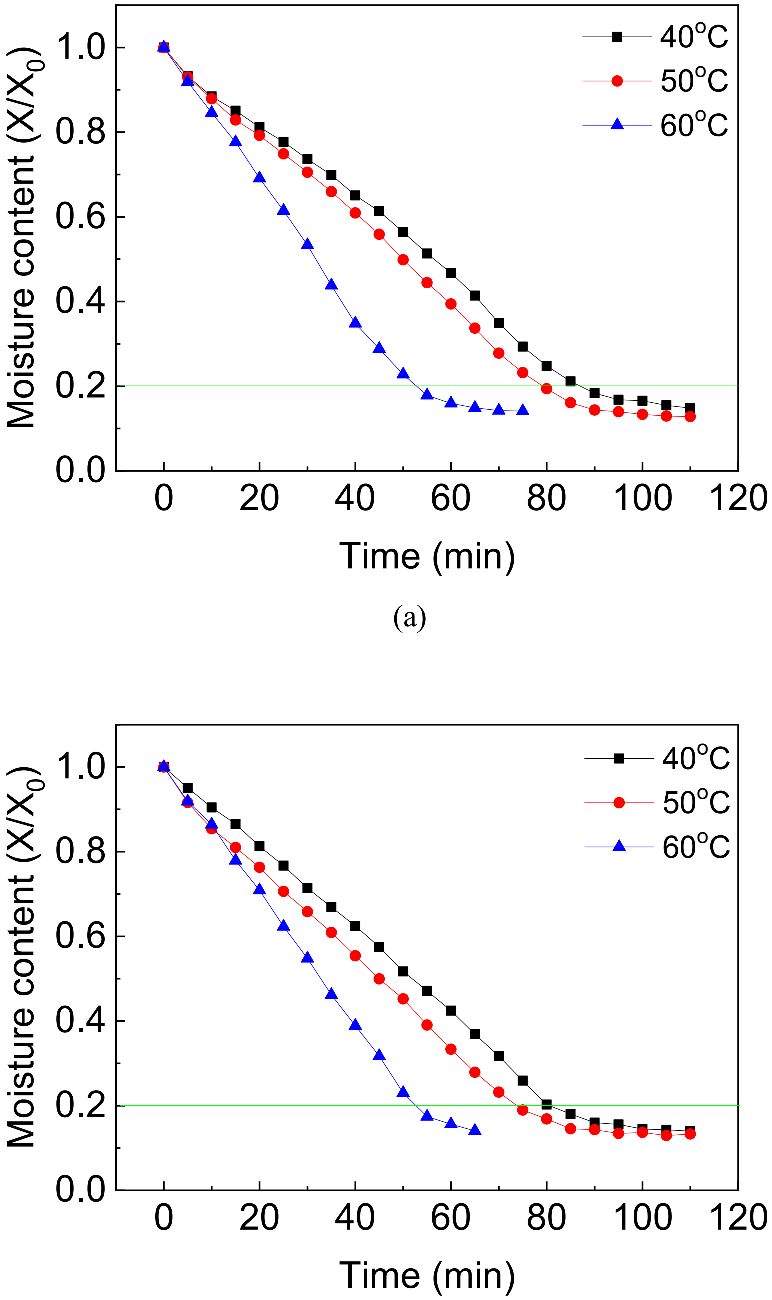

(a)

(b)

Figure 5.11 Effect of the inlet gas temperature on drying (a) conventional FBD, (b) PFBD with U=5.6U_{mf} and f=1.5 Hz.

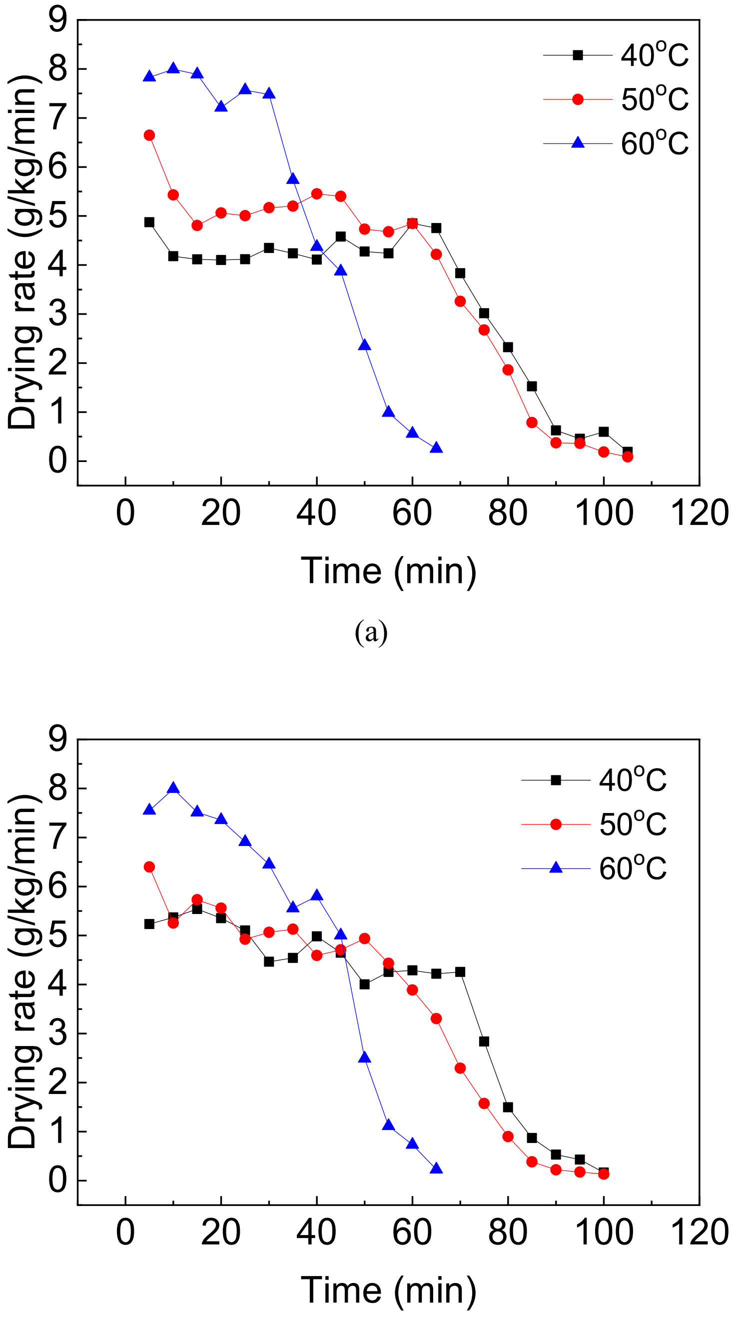

(a)

(b)

Figure 5.12 Effect of the inlet gas temperature on drying rate (a) conventional FBD, (b) PFBD with U=5.6U_{mf} , f=1.5 Hz and r=20%.

When drying porous materials, such as pharmaceutical granules in this work, there exist internal and external mass and heat transfer processes [125]. The external heat and mass transfer process happen between the surface of the wet granules and the gas phase. The air with a higher temperature enhances the evaporation of water at the surface of the granules by increasing the average kinetic energy of water molecules. The moisture removed by the external heat and mass transfer is mainly free water, as shown in Figure 5.13, during the constant drying rate period. The temperature gradient between the gas and granules surface is higher at higher gas temperatures.

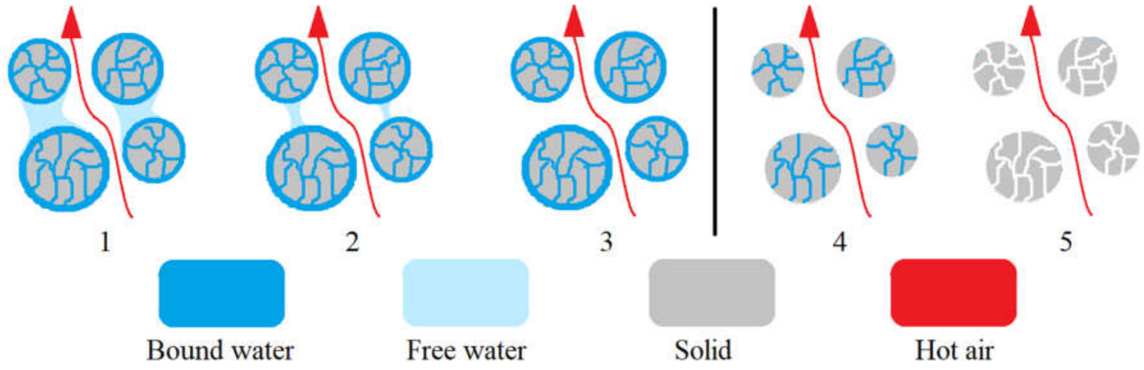

Figure 5.13 Classification of bound water and free water.

For the pharmaceutical granules used in this study, the boundary between the constant rate period and the falling rate period is the point when the moisture content is about 10 wb %. When the moisture outside of the granules is removed, and the surface of the granules is not fully covered with a water film, as illustrated in the fourth part of Figure 5.13, the heat transfer from the heated air from the granule surface to the inner granule structures. The bound water migrates from the granule core to the surface. A higher air temperature increases the mass transfer rate within granules due to the higher temperature gradient. In this work, the boundary between the constant rate drying and the falling rate drying period is found at a moisture content ratio of 0.2 (or 10 wb %).

The effect of the air temperature on energy efficiency is shown in Figure 5.14. Increasing the inlet air temperature is not favourable in terms of increasing energy efficiency in both conventional FBD and PFBD. It can be seen that the enhanced effect of the inlet air temperature is more significant in the PFBD than that in the conventional FBD [144].

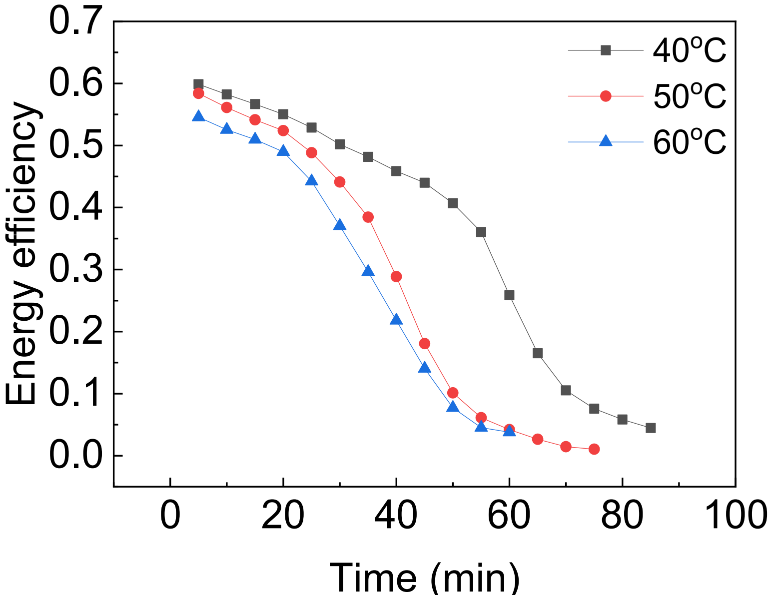

(a)

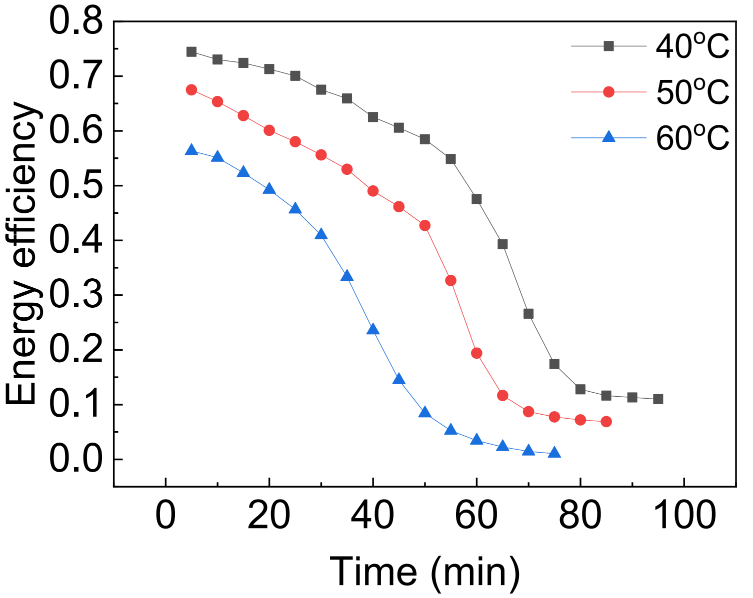

(b)

Figure 5.14 Effect of the inlet gas temperature on energy efficiency (a) conventional FBD, (b) PFBD with U=5.6U_{mf} , f=1.5 Hz and r=20%.

5.4.4 Effect of the pulsation frequency

In the literature, it has been reported that the hydrodynamic properties, including mixing efficiency, bubble size and bubble rise velocity, are influenced by the pulsation frequency [137, 157]. As a result, the pulsation frequency is expected to have an impact on the mass and heat transfer in the pulsed fluidized bed. Batch drying tests were conducted at the pulsation frequencies 1.5, 3.0, and 6.0 Hz to study the effect of pulsation frequency on drying the pharmaceutical granule. The moisture content curves of pharmaceutical granules during the drying process are shown in Figure 5.15.

At a higher superficial gas velocity of 1.4 m/s (5.6U_{mf}), as shown in Figures 5.15a and 5.15b, decreasing the pulsation frequency increases the drying rate. During the open or “on” period of the solenoid valve, the immediate air injection results in higher peak pressure in the fluidized bed as well as more fluctuations, which help in solid mixing and gas-solid contact. This high pressure and the following oscillation can overcome the cohesive inter-particle forces between wet pharmaceutical granules. The pulsed air can achieve higher peak pressure with a longer "off" period.

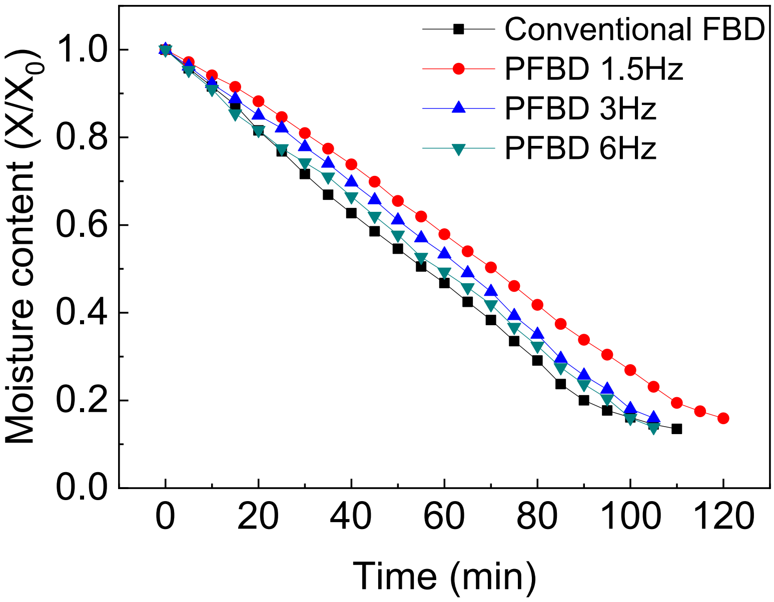

(a)

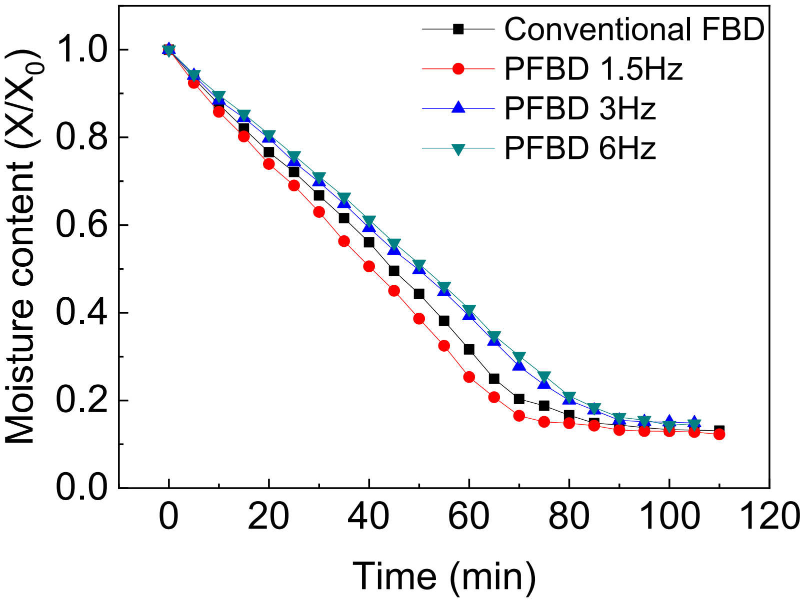

(b)

Figure 5.15 Effect of the pulsation frequency on drying (a) U=4.0U_{mf}, (b) U=5.6U_{mf} with T=50°C and r=20%.

The Student t-test was used to determine the statistically significant between the drying curves with different operating conditions. The mean values and p values are shown in Tables 5.5 and 5.6. It was found that the p values with all different operating conditions are between 0.16 to 0.46. The p values are larger than 0.05, which means the difference between the drying curves are insignificant. The statistical insignificance may be due to the small effect of pulsation frequency, the small sample size, or the high variability. Even though there is no statistically significant difference, the effects of pulsation frequency can still be seen Figure 5.15.

Table 5.5 Student t test of conventional FBD and pulsed FBD with different pulsation frequencies with $U=4.0U_{mf}$, $T=50°C$ and $r=20\%$.

Pulsation frequency	Mean	p value
Conventional FBD	0.52	0.24
PFBD 1.5 Hz	0.58	
Conventional FBD	0.52	0.22
PFBD 3.0 Hz	0.58	
Conventional FBD	0.52	0.33
PFBD 6.0 Hz	0.56	
PFBD 1.5 Hz	0.58	0.46
PFBD 3.0 Hz	0.58	
PFBD 1.5 Hz	0.58	0.40
PFBD 6.0 Hz	0.56	
PFBD 3.0 Hz	0.58	0.34
PFBD 6.0 Hz	0.56	

Table 5.6 Student t test of conventional FBD and pulsed FBD with different pulsation frequency with U=5.6U_{mf}, T=50°C and r=20%.

Pulsation frequency	Mean	p value
Conventional FBD	0.44	0.38
PFBD 1.5 Hz	0.42	
Conventional FBD	0.44	0.29
PFBD 3.0 Hz	0.49	
Conventional FBD	0.44	0.25
PFBD 6.0 Hz	0.50	
PFBD 1.5 Hz	0.42	0.19
PFBD 3.0 Hz	0.49	
PFBD 1.5 Hz	0.42	0.16
PFBD 6.0 Hz	0.50	
PFBD 3.0 Hz	0.49	0.45
PFBD 6.0 Hz	0.50	

The effect of the pulsation frequency on the drying rate is depicted in Figure 5.16. When the FBD is operated at a superficial gas velocity of 4.0U_{mf}, the conventional FBD has the highest drying rate, and when adding pulsed air, a higher pulsation frequency is more favourable to enhance the drying rate during the constant rate period. For the FBD with a higher superficial gas velocity (5.6U_{mf}), the highest drying rate (7.66 g/kg/min) was achieved at the pulsation frequency of 1.5 Hz.

The effect of the pulsation frequency on energy efficiency is shown in Figure 5.17. At both high and low superficial gas velocities, the PFBD shows a higher energy efficiency than the conventional FBD. A higher pulsation frequency is more favourable in terms of increasing energy efficiency when the superficial gas velocity is at $4.0U_{mf}$. When the superficial gas velocity is high, the PFBD with a lower pulsation frequency shows the highest energy efficiency (68%).

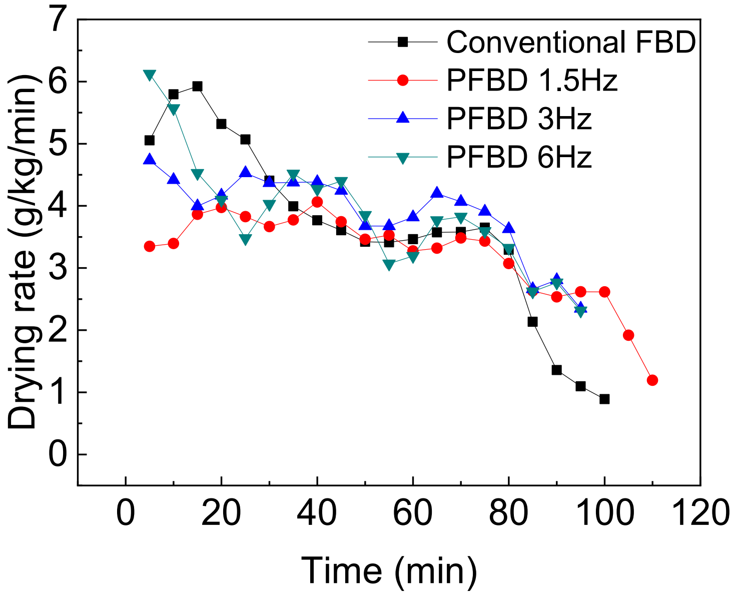

(a)

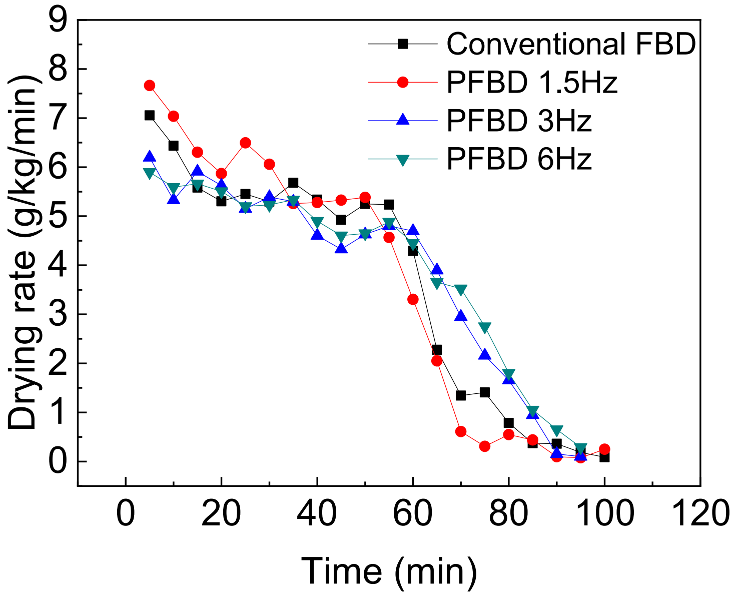

(b)

Figure 5.16 Effect of the pulsation frequency on the drying rate (a) $U=4.0U_{mf}$, (b) $U=5.6U_{mf}$ with $T=50$°C and $r=20\%$.

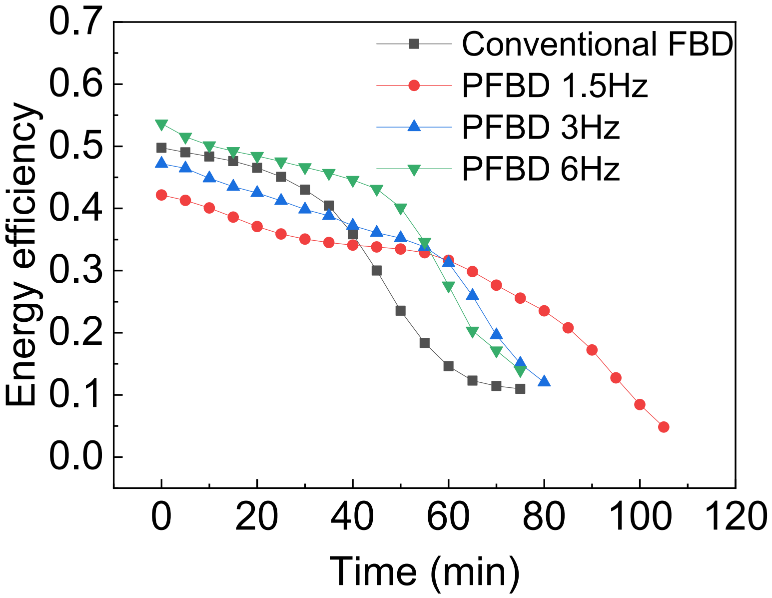

(a)

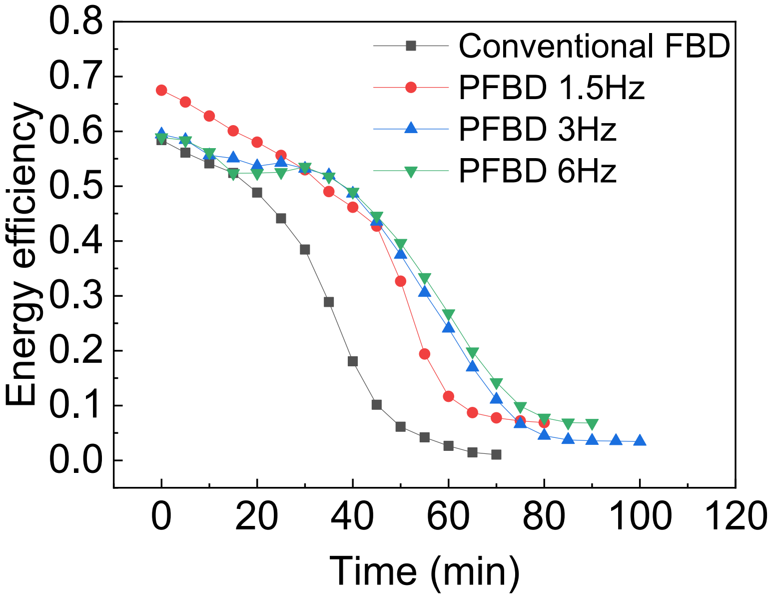

(b)

Figure 5.17 Effect of the pulsation frequency on energy efficiency (a) $U=4.0U_{mf}$, (b) $U=5.6U_{mf}$ with T=50℃ and r=20%.

5.4.5 Effect of the pulsed air ratio

The effect of the pulsed air ratio on the drying process is shown in Figure 5.18. The inlet gas temperature was maintained at 50°C, and the pulsation frequency was kept at 1.5 Hz.

When the superficial gas velocity is $4.0U_{mf}$, increasing the pulsed air ratio does not decrease the drying time, as indicated in Figure 5.18a. Instead, the drying time was increased from 90 minutes to 120 minutes when the pulsed air ratio increased from 0% (continuous flow) to 50%.

When the superficial gas velocity increases from $4.0U_{mf}$ to $5.6U_{mf}$, as shown in Figure 5.18b, increasing the pulsed air ratio shortens the drying time. At a lower pulsed air ratio, 30%, for instance, the drying time to reach a moisture content of 5 wb % is 70 minutes, while the drying time is shortened to 65 minutes at a pulsed air ratio of 50%.

The average drying rate during the constant drying rate period is shown in Table 5.7. When the FBD is operated at the superficial gas velocity of $4.0U_{mf}$, the average drying rate decreases from 6.22 g/kg/min to 4.35 g/kg/min (31% lower) with increasing the pulsed air ratio from 0% (a conventional FBD) to 50%. For an FBD operated at a higher superficial gas velocity of $5.6U_{mf}$, a higher pulsed air ratio is more favourable to enhance the drying rate. When the pulsed air ratio is between 0% to 20%, the drying rates during the constant rate period range from 6.95 to 7.06 g/kg/min. The narrow range indicates that adding pulsed air does not increase the drying rate and facilitate the drying when the PFBD is operated at a higher superficial gas velocity. The pulsed air ratio is low. It might be due to that the natural frequency of the fluidized bed overshadows the pressure fluctuations caused by the pulsed airflow [125].

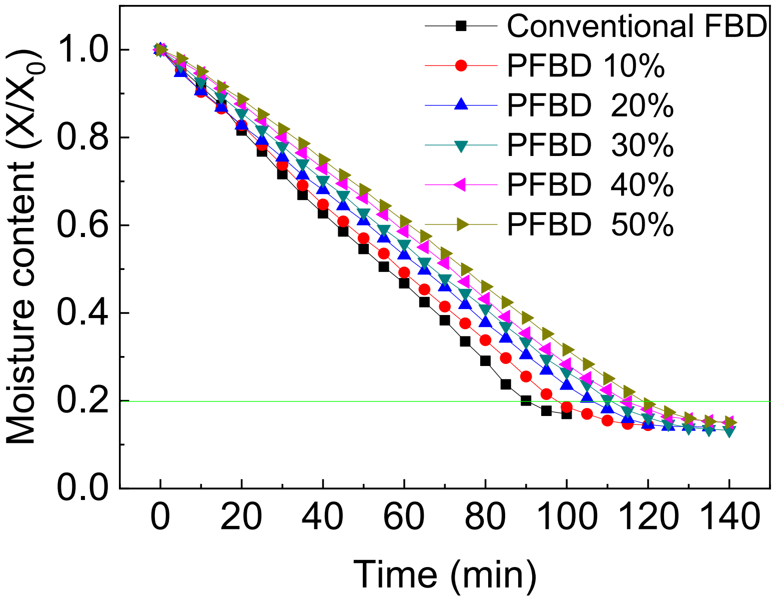

(a)

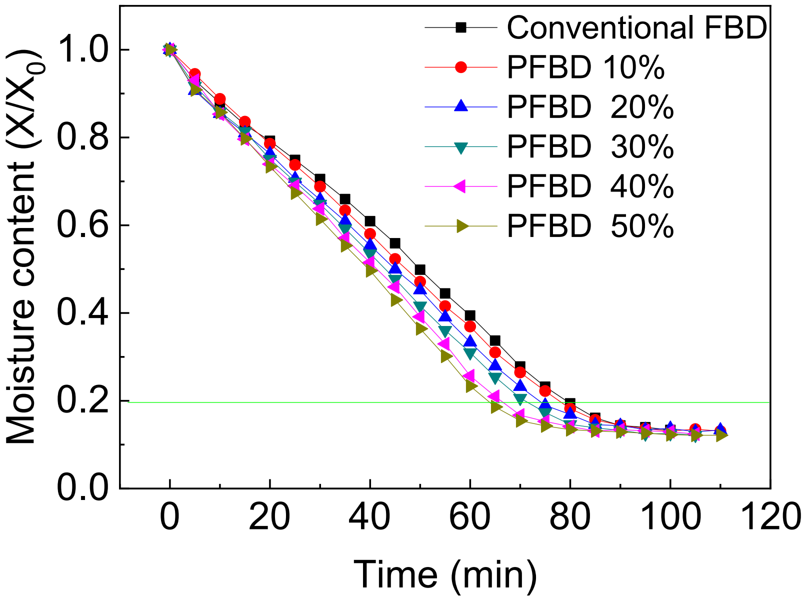

(b)

Figure 5.18 Effect of the pulsed air ratio on drying (a) U=4.0U_{mf}, (b) U=5.6U_{mf} with T=50℃ and f=1.5 Hz.

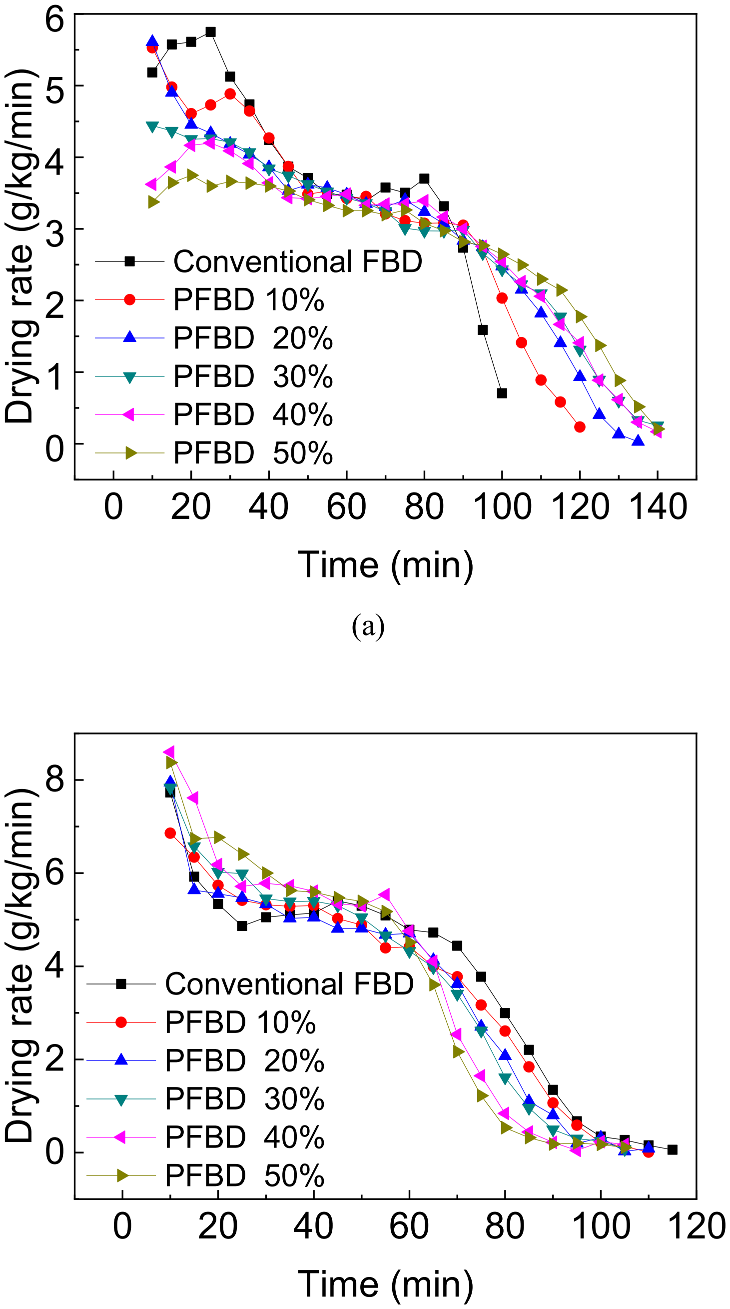

(a)

(b)

Figure 5.19 Effect of the pulsed air ratio on drying rate (a) U=4.0U_{mf}, (b) U=5.6U_{mf} with T=50℃ and f=1.5 Hz.

Table 5.7 Effect of the pulsed air ratio on drying rate during the constant rate period (g/kg/min) with T=50℃ and f=1.5Hz

Pulsed air ratio	$4.0U_{mf}$	$5.6U_{mf}$
Conventional FBD	6.22±0.05	7.06±0.09
10%	5.51	6.99
20%	4.93±0.05	6.95±0.04
30%	4.78	7.47
40%	4.48	8.20
50%	4.35	8.13

The effect of the pulsed air ratio on energy efficiency is shown in Figure 5.20. The effect of the pulsed air ratio is depends on the superficial gas velocity. When the superficial gas velocity is low, higher energy efficiency is observed at a lower pulsed air ratio in the PFBD. When the superficial gas velocity is at $5.6U_{mf}$, increasing the pulsed air ratio enhances energy efficiency.

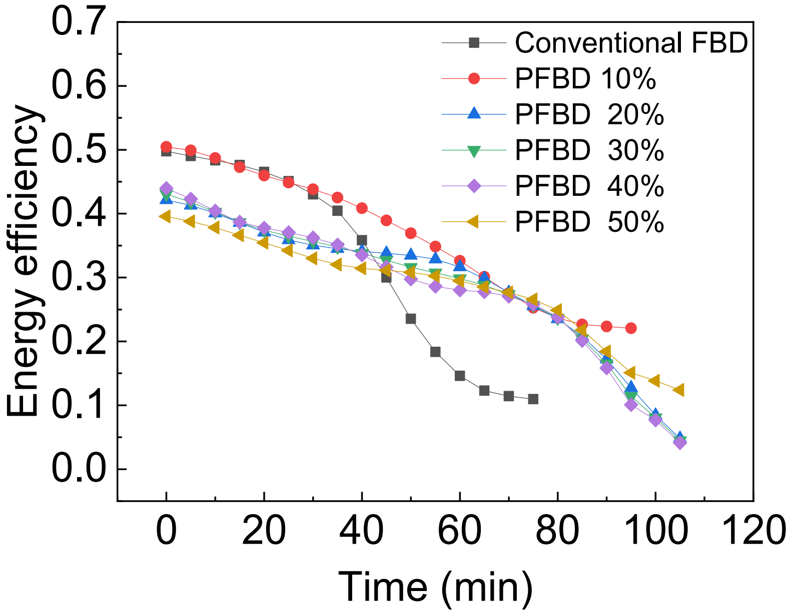

(a)

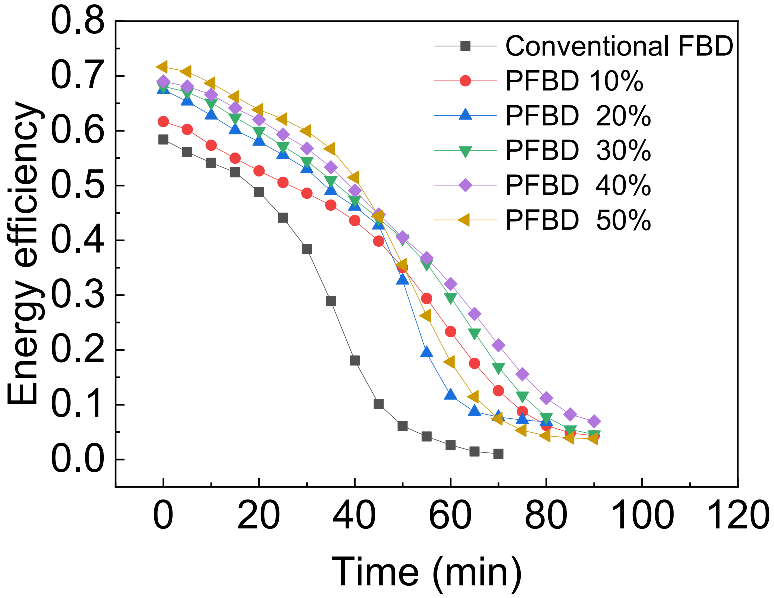

(b)

Figure 5.20 Effect of the pulsed air ratio on energy efficiency (a) U=4.0U_{mf}, (b) U=5.6U_{mf} with T=50℃ and f=1.5 Hz.

5.4.6 Drying models

The best model to predict the drying curve is the one with the largest R^2, the smallest χ^2, and the smallest RMSE. Tables 5.8-5.11 show the statistical results of the fitting parameters of nine models for the conventional FBD and the PFBD with a pulsation frequency of 1.5, 3.0, and 6.0 Hz, a superficial gas velocity $5.6U_{mf}$, a temperature of 50°C, and a pulsed air ratio of 0.2. It can be seen that among the nine models, Midilli and Kucuk model showed the best prediction with the largest R^2 (0.9940-0.9960), smallest χ^2 (0.0005-0.0007), and smallest RMSE (0.0220-0.0254). Figure 5.21 shows the comparison between the drying experimental data and predicted data from the nine thin-layer drying models. All the models have shown relatively good agreement between the experimental data and the predicted values from these models. However, Midilli and Kucuk model with the smallest deviation is considered the best model for the drying curve of the pharmaceutical granules used in this work.

Model 1 (Newton) and Model 3 (Page) are derived from Newton's law of cooling. The other models tested in this study are the semi-theoretical models derived from Fick’s second law of diffusion. These models can be classified based on exponential terms, namely the single term exponential model and its modified forms, the two-term exponential model and its modified forms, and the term exponential model. The models based on Newton's law of cooling have good fitness when the superficial gas velocity is high. This is related to the model assumption that during the falling-rate period, the drying rate is proportional to the difference between the moisture content at the granules surface and its expected equilibrium value and other operating conditions, including the air temperature and relative humidity, are constant. The assumption is valid when the particles are fully fluidized at high superficial gas velocity.

The other models, namely Models 2, 4, 5 to 9, are derived from Fick’s second law of diffusion. The main difference between the models derived from Fick’s second law of diffusion and Newton's law of cooling is the dimensionless coefficient, a, which is a constant taking into account the shape and size of the particle. Model 4 and Model 8 were modified based on the single-term exponential model. Model 4 has an empirical dimensionless constant “c,” which indicates the preheating stage. Model 8 was based on the single term exponential model by adding a “b*t” term. This term is used to improve the accuracy by reflecting the drying rate difference between the constant rate period and the falling rate period. The Models 5, 6, 7, 9 have two exponential terms. By adding the exponential term, these models may have higher accuracy to predict multi-component mixtures. However, introducing additional constants also decrease the convenience of use.

In this work, the initial moisture content of the wet granules was 31 wb %. The drying rate difference between the constant rate period (5 to 9 g/kg/min) and the falling rate period (0.1 to 2 g/kg/min) is quite significant. The drying time is usually within 120 minutes, significantly shorter than other drying techniques, such as solar drying, which usually takes several days. The additional term in Model 8 “b*t” makes this model providing the best prediction of drying the pharmaceutical granules in a PFBD.

Table 5.8 Results of the fitting parameters of the conventional FBD with U=5.6U_{mf} and T=50°C

Model Number	Coefficients and constants	R^2	χ^2	RMSE
1	k=0.0180	0.977	0.003	0.055
2	a=1.0788, k=0.0196	0.973	0.002	0.048
3	k=0.0053, n=1.2860	0.991	0.001	0.035
4	a=1.0787, k=0.0195, c=0	0.973	0.002	0.048
5	a=1.0788, k=0.0195, c=0, g=0.0641	0.973	0.002	0.048
6	a=1.8954, k=0.0273	0.991	0.001	0.028
7	a=20.0705, k=0.0346, g=0.0360	0.992	0.001	0.027
8	a=0.9491, k=0.0012, n=1.6248, b=0	0.994	0.001	0.022
9	a=0.9566, k=0.0025, n=1.4703, c=0.0433, g=1.1999	0.993	0.001	0.026

Table 5.9 Results of the fitting parameters of the PFBD with U=5.6 U_{mf}, T=50°C, f=1.5 Hz and r=20%

Model Number	Coefficients and constants	R^2	χ^2	RMSE
1	k=0.0198	0.980	0.002	0.050
2	a=1.0695, k=0.0212	0.977	0.002	0.043
3	k=0.0063, n=1.2867	0.990	0.001	0.990
4	a=1.0694, k=0.0212, c=0	0.977	0.002	0.043
5	a=1.0695, k=0.0212, c=0, g=0.0641	0.977	0.002	0.043
6	a=1.8487, k=0.0291	0.990	0.001	0.029
7	a=20.2763, k=0.0363, g=0.0377	0.991	0.001	0.029
8	a=0.9457, k=0.0020, n=1.5403, b=0.0003	0.994	0.001	0.022
9	a=0.9694, k=0.0046, n=1.3565, c=0.0305, g=1.1999	0.991	0.001	0.029

Table 5.10 Results of the fitting parameters of the PFBD with *U*=5.6 U_{mf}, *T*=50°C, *f*=3.0 Hz and *r*=20%

Model Number	Coefficients and constants	R^2	χ^2	RMSE
1	k=0.0164	0.975	0.004	0.066
2	a=1.0877, k=0.0180	0.969	0.003	0.057
3	k=0.0025, n=1.4534	0.994	0.001	0.029
4	a=1.0877, k=0.0180, c=0	0.969	0.003	0.057
5	a=1.0877, k=0.0180, c=0, g=0.1977	0.969	0.003	0.057
6	a=1.9373, k=0.0256	0.992	0.001	0.033
7	a=19.2131, k=0.0328, g=0.0344	0.993	0.001	0.031
8	a=0.9590, k=0.0015, n=1.5789, b=0	0.995	0.001	0.026
9	a=0.9316, k=0.0009, n=1.6701, c=0.0683, g=1.2001	0.996	0.001	0.024

Table 5.11 Results of the fitting parameters of the PFBD with *U*=5.6 U_{mf}, *T*=50°C, *f*=6.0 Hz and *r*=20%

Model Number	Coefficients and constants	R^2	χ^2	RMSE
1	k=0.0158	0.973	0.005	0.070
2	a=1.0944, k=0.0176	0.966	0.004	0.060
3	k=0.0020, n=1.5010	0.995	0.001	0.028
4	a=1.0944, k=0.0176, c=0	0.966	0.004	0.060
5	a=1.0944, k=0.0176, c=0, g=0.1977	0.966	0.004	0.060
6	a=1.9635, k=0.0253	0.992	0.001	0.034
7	a=19.2145, k=0.0326, g=0.0343	0.993	0.001	0.032
8	a=0.9579, k=0.0010, n=1.6368, b=0	0.996	0.001	0.025
9	a=0.9323, k=0.0007, n=1.7273, c=0.0676, g=1.2001	0.997	0.001	0.022

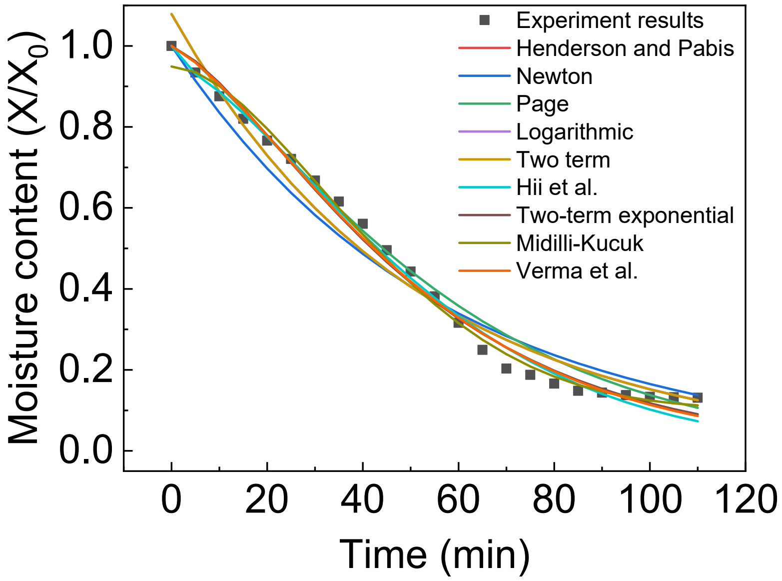
Moisture content (X/X0)
1.0
0.8
0.6
0.4
0.2
0.0
0
20
40
60
80
100
120
Time (min)
Experiment results
Henderson and Pabis
Newton
Page
Logarithmic
Two term
Hii et al.
Two-term exponential
Midilli-Kucuk
Verma et al.

(a)

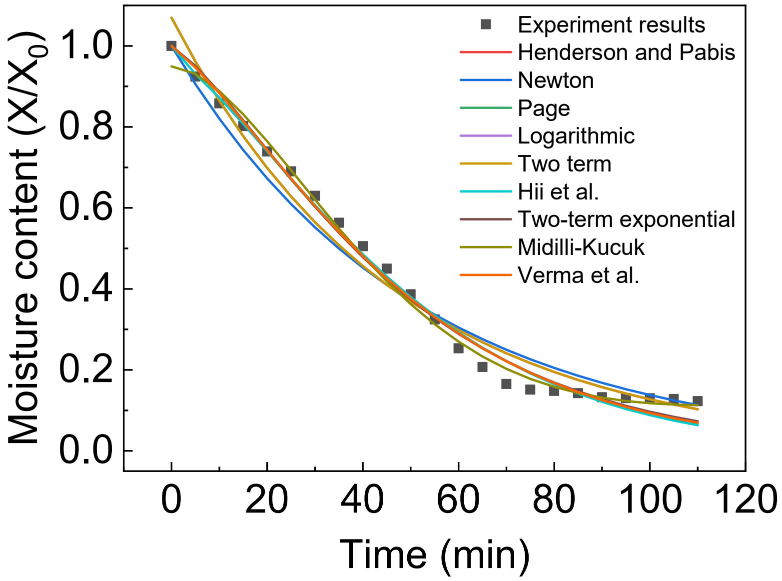
Moisture content (X/X0)
1.0
0.8
0.6
0.4
0.2
0.0
0
20
40
60
80
100
120
Time (min)
Experiment results
Henderson and Pabis
Newton
Page
Logarithmic
Two term
Hii et al.
Two-term exponential
Midilli-Kucuk
Verma et al.

(b)

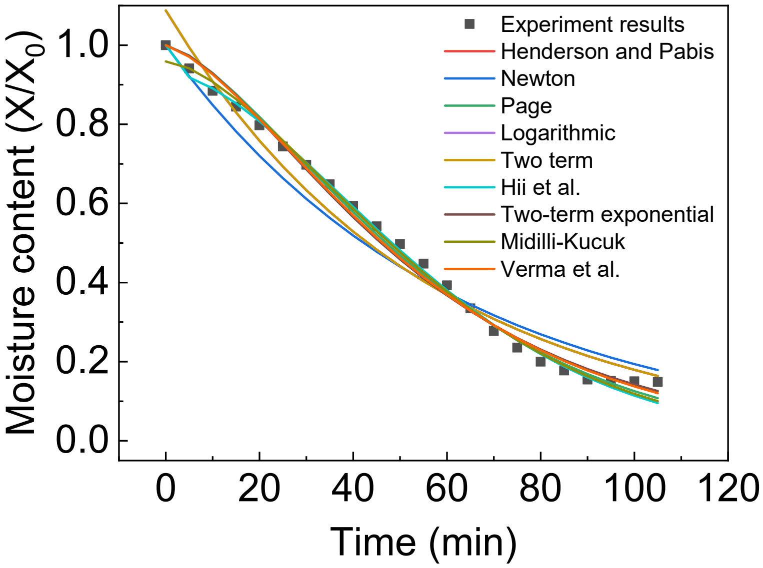

(c)

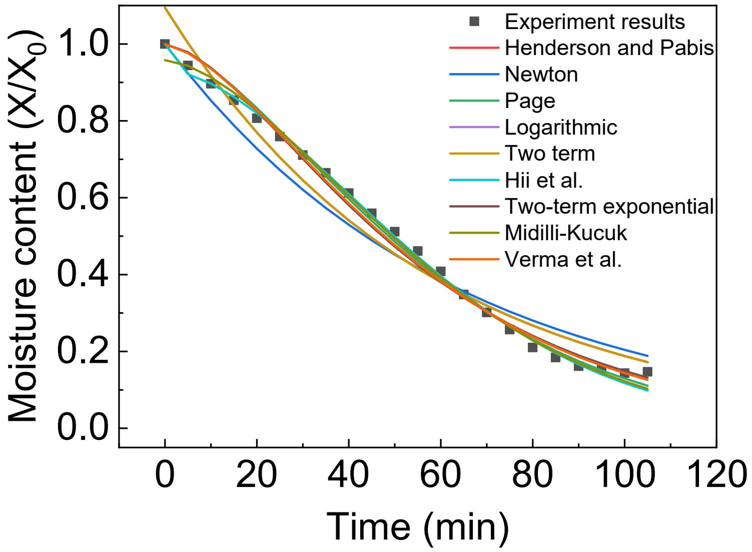

(d)

Figure 5.21 Comparison between the experimental data and predicted values from (a) conventional FBD and PFBD with a pulsation frequency of (b) 1.5Hz, (c) 3.0Hz, (d) 6.0Hz, U=5.6 U_{mf}, T=50°C, and r=20%.

Other operating conditions were also examined, and in general, Midilli and Kucuk model gave the best prediction results. The coefficients and constants of the Midili and Kucuk thin layer model for different operating conditions are shown in Table 5.12. It was found that the coefficients, b, of conventional FBD and the PFBD at a high pulsation frequency, namely 3.0 Hz and 6.0 Hz, became zero, which means the Midili and Kucuk model is simplified to the Henderson and Pabis model. This is consistent with the similarity between the conventional FBD and high-frequency PFBD discussed above. Increasing the pulsed air ratio from 0% to 50%, the coefficients, b, increased from 0 to 0.0008. The increased coefficient of b makes the predicted drying curve steeper during the constant rate period and flatter during the falling rate period. This is supported by the enhanced effect of pulsation on the drying pharmaceutical granules in a fluidized bed dryer discussed above.

Table 5.12 Coefficients and constants of Midilli and Kucuk model

Operating conditions	a	k	n	b
Conventional FBD, U=5.6U_{mf}, T_{in}=50°C	0.9491	0.0012	1.6248	0
PFBD r=20%, f=1.5 Hz, U=5.6U_{mf}, T_{in}=50°C	0.9457	0.0020	1.5403	0.0003
PFBD r=20%, f=3.0 Hz, U=5.6U_{mf}, T_{in}=50°C	0.9590	0.0015	1.5789	0
PFBD r=20%, f=6.0 Hz, U=5.6U_{mf}, T_{in}=50°C	0.9580	0.0011	1.6369	0
PFBD r=20%, f=1.5 Hz, U=4.0U_{mf}, T_{in}=50°C	0.9561	0.0013	1.5083	0
PFBD r=20%, f=1.5 Hz, U=5.6U_{mf}, T_{in}=40°C	0.9640	0.0011	1.6348	0.0002
PFBD r=20%, f=1.5 Hz, U=5.6U_{mf}, T_{in}=60°C	0.9725	0.0028	1.5816	0
PFBD r=0.1, f=1.5 Hz, U=4.0U_{mf}, T_{in}=50°C	0.9665	0.0019	1.5405	0.0002
PFBD r=0.3, f=1.5 Hz, U=4.0U_{mf}, T_{in}=50°C	0.9520	0.0021	1.5612	0.0004
PFBD r=0.4, f=1.5 Hz, U=4.0U_{mf}, T_{in}=50°C	0.9494	0.0017	1.6392	0.0008
PFBD r=0.5, f=1.5 Hz, U=4.0U_{mf}, T_{in}=50°C	0.9454	0.0017	1.6641	0.0008

5.5 Conclusions

A comprehensive experimental study on the drying performance of wet pharmaceutical granules was conducted in a pulsation-assisted fluidized bed dryer. A representative formulation, including active pharmaceutical ingredients (APIs), was used as the wet powders. The following conclusions can be drawn from the experimental results:

The added pulsation effectively enhances drying at a high superficial gas velocity when the wet solid is maintained at minimum fluidization by the continuous gas flow. In general, the PFBD shows higher energy efficiency than the conventional FBD. More profoundly enhanced effects are observed at higher superficial gas velocity and lower inlet drying air temperature. A lower pulsation frequency, namely 1.5 Hz, is more favourable to improve the drying rate than a high pulsation frequency. The impact of the pulsed air ratio depends on the superficial gas velocity. At the low superficial gas velocity, decreasing the pulsed air ratio helps enhance the drying rate. In contrast, at the high superficial gas velocity, the drying rate is higher at a higher pulsed air ratio. Among the nine thin-layer models examined, the Midilli and Kucuk model shows the best performance in terms of predicting the drying curve due to the addition of a linear term, which reflects the difference of drying rate between the constant rate period and the falling rate period.

CHAPTER 6. INVESTIGATING TRIBOCHARGING BEHAVIOUR OF PHARMACEUTICAL GRANULES IN A PULSATION-ASSISTED FLUIDIZED BED DRYER

The content of this chapter will be submitted to a journal for publication.

Contribution of the Ph.D. student:

The experiments were planned and performed by Chen Li. Lifeng Zhang supervised and provided consultation during the experiment preparation, data analyzing, and thesis preparation. Kwangseok Choi offered technical support during set-up construction and work function measurement. Carter Blocka provided help during the experiment. The writing of the manuscript was done by Chen Li, with Lifeng Zhang providing editorial guidance.

Contribution of this chapter to the overall study

Employing pulsed air is a promising method to enhance fluidization and eliminate channeling. However, the pulsation may also influence the tribocharing phenomenon during drying. This chapter provides a good understanding of the tribocharging behaviour of pharmaceutical granules in a pulsed fluidized bed dryer. The effect of important operating parameters, including superficial gas velocity, air temperature, pulsation frequency, as well as pulsed air ratio, and materials parameters, including moisture content and API on tribocharing, were studied in this chapter. These results advance the understanding of the tribocharing phenomenon during the pulsed fluidized bed drying process.

6.1 Abstract

Pharmaceutical powders are prone to carrying electrostatic charge during various manufacturing processes due to the high electrical resistivity. After repeated inter-particle and particle-wall contacts, the net charge acquired by pharmaceutical powders can be very high, posing

significant challenges to industrial processes. The pulsed fluidized bed is a promising method to enhance drying. However, pulsed air may result in more charge accumulation. A clear understanding of the tribocharging behaviour of granules in the pulsed fluidized dryer is essential for optimal process design and safe operation. Tribocharging phenomenon of pharmaceutical granules has been tested in a pulsed fluidized bed with the pulsation frequency 1.5-6.0 Hz, superficial gas velocity 1.0-1.4 m/s, inlet gas temperature 40-60℃, and pulsed air ratio 0-50%.

The specific charge of pharmaceutical granules remained low during the constant rate period. When the moisture content was reduced to a critical moisture content, namely 10%, the specific charge (charge per unit mass) increased sharply. The specific charge amount accumulated during the falling rate period before reach an equilibrium value. This equilibrium specific charge is influenced by the superficial gas velocity, pulsation frequency and pulsed air ratio. Higher superficial gas velocity, lower pulsed frequency, and higher pulsed air ratio have an enhanced effect on the specific charge. When the superficial gas velocity is low, there is no noticeable difference between conventional FBD and PFBD with different pulsation frequencies. The inlet air temperature and pulsed air ratio did not significantly impact the equilibrium specific charge value.

6.2 Introduction

In the pharmaceutical industry, tablets are the most common solid oral dosage (SOD) form, which offers enhanced physical and chemical stability, relatively easy preparation, ease of use, and high throughput and low manufacturing cost [158]. Wet granulation is the most popular method to manufacture tablets in the pharmaceutical industry since its versatility [159].

Fluidized beds are frequently used during the wet granulation and drying operations during the pharmaceutical tablet manufacturing process. One problem during fluidized bed operation is the occurrence of electrostatic charge generation and accumulation due to frequent particle-particle collision and particle-wall contact [160]. This electrostatic phenomenon is also known as tribocharging [161]. Most of the active pharmaceutical ingredients (APIs) and excipients are organic materials with high electrical resistivity (~10^{13} Ωm), which makes the materials can be easily charged [155, 162, 163]

Charge accumulation in fluidized beds might result in particle-wall adhesion, particle agglomeration and segregation, hot spot, and even explosion if there is significant electrostatic discharge [164]. It was found that the electrostatic voltage of the fluidized bed increased when increasing the superficial gas velocity at constant humidity [155]. The studies of the effect of gas temperature on tribocharging show that when using low-density polyethylene (LLDPE) particles [165], glass beads [166], or mental spheres [167] as solids phase increasing gas temperature resulted in a decrease in electrostatic charge generation. The effects of drying gas temperature on the electrostatic charge generation with different materials can be explained by the work function theory. The temperature increase can result in enhanced agility of the electrons, which may enhance electron release and reduce the work function. [168].

The net charge increases with increasing the particle size and the bubble size bed [169]. For a bubbling fluidized bed, increasing the loading particle weight would lead to higher net charge accumulation [170]. The movement status of gas and solids determines the particle-particle and particle-wall contact and friction frequency and intensity, thereby influencing the charge generation, dissipation, and accumulation rate [171, 172]. Previous studies show that the specific charge did not change at the beginning of the drying process until the moisture content was reduced to a critical moisture content (CMC) [155, 163].

It can be seen that most of the current research attention has been placed on the tribocharging phenomenon in conventional fluidized beds. However, when handling fine, cohesive, or wet powders, channeling, partial, or fully defluidization significantly influences heat and mass transfer. Applying pulsed airflow is a promising method to solve this issue. Our recent study showed that adding pulsed airflow to a fluidized bed dryer increased the drying rate and increased the energy efficiency, as discussed in chapter 5.4. However, how the added pulsation influences the tribocharging phenomenon in a fluidized bed dryer is not known.

To fully understand the effect of pulsed airflow on the charge generation inside the fluidized bed, it is crucial to analyze the effect of critical operating conditions, such as superficial gas velocity, air temperature, pulsation frequency, pulsed air ratio. In addition, determining the work function of the pharmaceutical powder is essential to understand the charge polarity as well as quantity. Moreover, this study employed a pharmaceutical mixture, including APIs and excipients, to simulate the tribocharging phenomenon in actual pharmaceutical industrial production.

6.3 Materials and methods

6.3.1 Material characterization and preparation

The experiments were conducted with pre-determined compositions of two formulations, as shown in Table 6.1 and Table 6.2. The chemical structures of the pharmaceutical powders and liquid binder are shown in Figure 6.1. The initial moisture content was 30 ± 1% (wet basis). The dry pharmaceutical powders were stored in a chamber with a constant temperature of 24 ℃ and relative humidity (RH) of 30%. Dry pharmaceutical powders were sieved through a 2.00 mm sieve and mixed with a 250 W low-shear granulator (Kitchen-Aid classic mixer) for 2 minutes at the lowest speed (setting 1). Then, deionized water was gradually added at a rate of 59 mL/min during the following 5 minutes, followed by a higher speed (setting 2) mixing. Afterward, the mixture was sieved through a screen with an opening of 3.36 mm [140]. The wet granules were sealed in a basket and stored in a chamber (kept at 24 ℃) to ensure uniformity of moisture content and temperature distribution for 1 hour.

Table 6.1 Mass percentage of the pharmaceutical powder mixture with API

Component	Function	Percentage by mass (wet basis)
Acetaminophen (APAP)	API	13%
Lactose monohydrate (LMH)	Filler	28%
Microcrystalline cellulose (MCC)	Filler	25%
Hydroxypropyl methylcellulose (HPMC)	Binder	3%
Croscamellose sodium (CCS)	Disintegrant	1%
Water	Solution binder	30%

Table 6.2 Mass percentage of the pharmaceutical powder mixture without API

Component	Function	Percentage by mass (wet basis)
Lactose monohydrate (LMH)	Filler	38%
Microcrystalline cellulose (MCC)	Filler	35%
Hydroxypropyl methylcellulose (HPMC)	Binder	3%
Croscamellose sodium (CCS)	Disintegrant	1%
Water	Solution binder	30%

The characterization of the powder materials, including median particle size, particle skeletal density, and particle bulk density, used in this study is presented in Table 6.3. The median particle size was measured with a Malvern 2000 Mastersizer S (Malvern Instruments, UK). Particle skeletal density was determined by an Ultrapycnometer 1000 (Quantachrome Instruments, Austria).

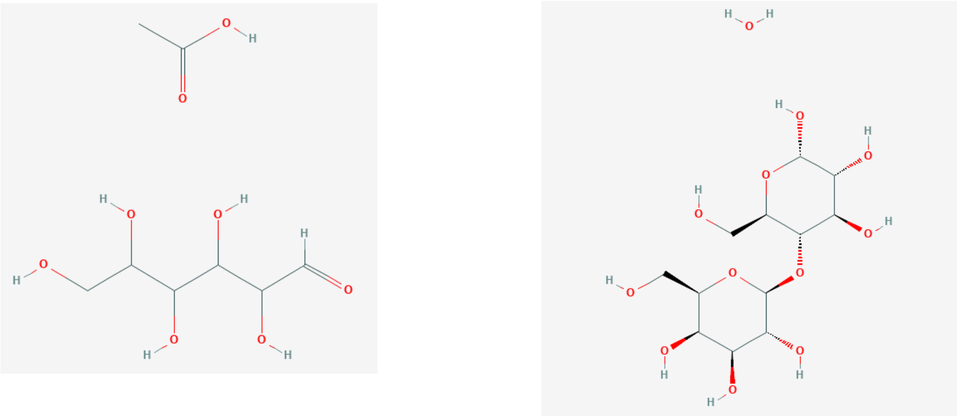

(a)
APAP

(b)
LMH

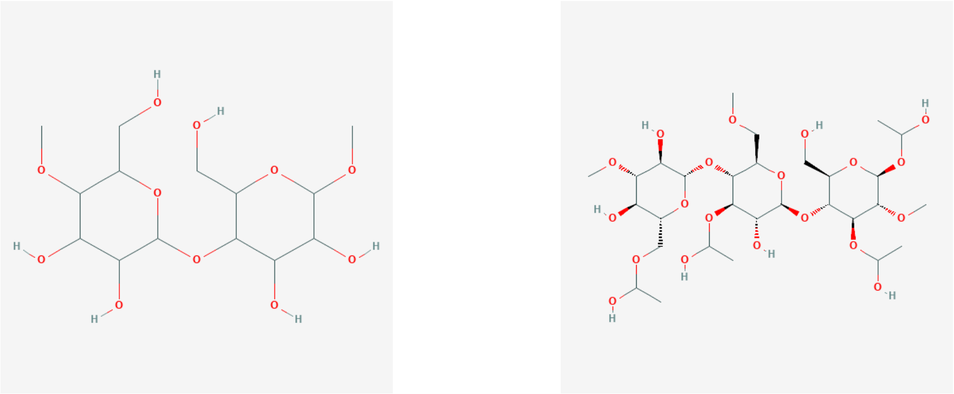

(c)
MCC

(d)
HPMC

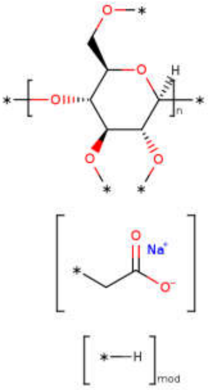

(e)
CCS

Figure 6.1 Chemical structure of the pharmaceutical powder and liquid binder [173].

Table 6.3 Physical properties of pharmaceutical powders

Component	Median particle size, d_{50} (µm)	Particle skeletal density, ρ_p (g/cm^3)	Particle bulk density, ρ_{bed} (g/cm^3)
APAP	96	1.72	0.57
LMH	70	1.52	0.56
MCC	128	1.61	0.36
HPMC	82	1.56	0.52
CCS	41	1.62	0.54

6.3.3 Pulsed fluidized bed dryer setup

Throughout the drying experiment, data were simultaneously collected from the thermocouples, RH meters, and pressure transducers located at the inlet and outlet of the fluidized bed dryer, as shown in Figure 6.2. The details of the pulsed fluidized bed dryer setup have been discussed in section 5.3.2.

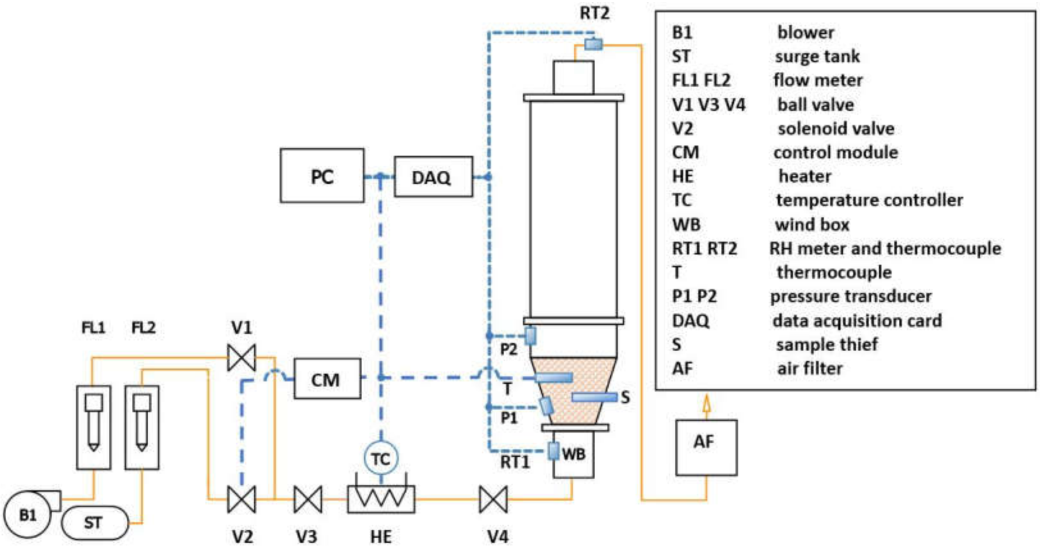

Figure 6.2 The pulsed fluidized bed dryer set-up.

6.3.4 Tribocharging measurements

The drying experiment was conducted batch-wise. The PFBD was adjusted to reach pre-set operating conditions before each run in order to shorten the preheat time. Then, 2 kg of wet pharmaceutical granules were loaded into the product bowl. The average superficial gas velocity (1.0, 1.4, and 1.8 m/s), gas temperature (40, 50, and 60 ℃), pulsed air ratio (0, 10, 20, 30, 40, 50%), and pulsation frequency (0.75, 1.5, 3.0 Hz) are the operating parameters studied. During each run, approximately 3 g granules samples were taken from the central part of the product bowl every 5 minutes with a sampling thief. The experiment operator was grounded by contacting the mental frame of the fluidized bed dryer before each sampling.

The net charge was determined using a Faraday cup connected with an electrometer (6514, Keithley, USA). The diameter of the internal cup of the Faraday cup is 100 mm and a height of 100 mm, as well as an outer cup with a diameter of 150 mm and a height of 140 mm. Moisture content was determined using a drying balance (HB43, Mettler-Toledo, USA). Experiments under certain conditions were repeated five times to determine standard errors. The minimum fluidization velocity (U_{mf}) was 0.25 m/s. The specific charge q (μC/kg) is defined as:

$$q=Q/m \tag{6.1}$$

where Q (μC) is the total charge of the pharmaceutical granules sample, and m is the weight of the sample loaded into the Faraday cup.

6.3.5 Uncertainty analysis

The experiments were repeated five times at a superficial gas velocity of $5.6U_{mf}$, an air temperature of 50℃, a pulsation frequency of 1.5 Hz, and a pulsed air ratio of 20% to evaluate the experimental error. The standard deviations of the specific charge results are shown in Figure 6.3.

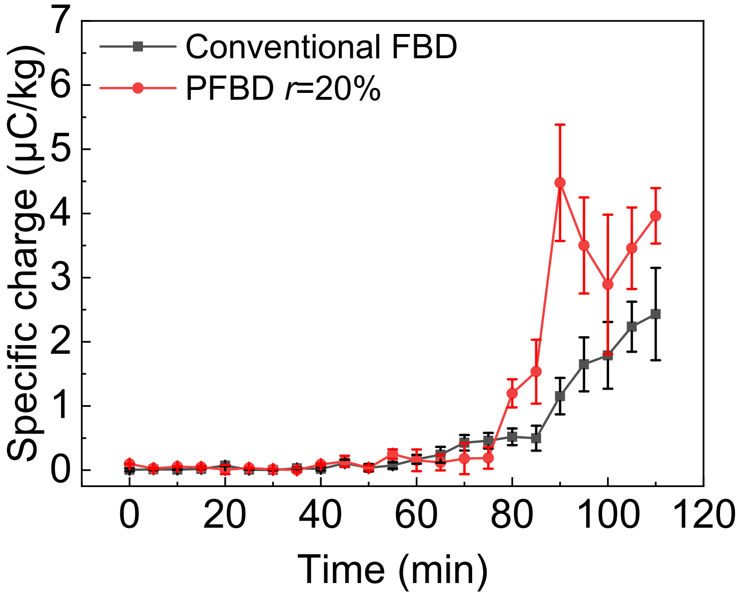

Figure 6.3 Standard deviations of the specific charge of pharmaceutical granules with U=5.6U_{mf}, T=50°C, f= 1.5 Hz, and r= 20%.

The standard deviations are 39.2% and 37.6% for the conventional FBD and the PFBD during the falling rate period. The specific charges have high standard deviation values and very sensitive to the environment.

6.4 Results and discussion

6.4.1 Effect of pulsation

During the particle handling process, due to frequent inter-particle and particle-wall collision and separation, the tribocharing phenomenon is unavoidable. The charge generation and accumulation in the fluidized bed are inevitable. The comparison between the convention FBD and PFBD at the superficial gas velocity of 4.0U_{mf} and 5.6U_{mf} is shown in Figure 6.4.

It can be seen that at both superficial gas velocities, the specific charge remains lower than 0.5 μC/kg at the beginning of the drying process, which is consistent with the duration of the constant rate period. Afterward, when the moisture content reached 10 wb % , the charge increased at a rate of 0.07-0.22 μC/kg/min. A similar phenomenon was reported by our previous study in a conventional fluidized bed dryer [145]. The moisture content at which a sharp rise started to occur is defined as the critical moisture content (CMC). This phenomenon is related to the two types of moisture within the pharmaceutical granules, namely, unbound water (or free water) and bound water. Unbound water is defined as the water on the surface of the granule, which can be evaporated with ease.

In contrast, bound water mainly exists within granules. The capillary force resulted in extra resistance during the drying process. When the surface of the granule is covered by a thin layer of unbound water, the difference between the charge accumulate rate and discharge rete is small. Thus, the net charge build-up rate is slow. When the moisture content is lower than the critical moisture content, the charge starts to gather as the surface of the granules becomes partially or completely dry. The volume resistivity also increases when the moisture content decreases. It was reported that the volume resistivity of particles increased by order of 10^6 when the moisture decreased from 30% to 5% [163]. The specific charge reaches a maximum value ranges from 2.0 to 4.5 μC/kg. It also can be seen in Figure 6.4 that the increase in the charge generation is not linear.

The comparison of the specific charge shows that the specific charge of the granules in the PFBD is higher than that in the conventional FBD observed at the same operating conditions. The average specific charge during the falling rate period of the conventional FBD is +1.47 μC/kg while +2.65 μC/kg is observed for the PFBD. This is due to the enhanced particle mixing and particle movements induced by pulsed airflow. The pulsed air results in more inter-particle and particle-wall collision and separation, which in turn caused more charge generated compared to the conventional FBD.

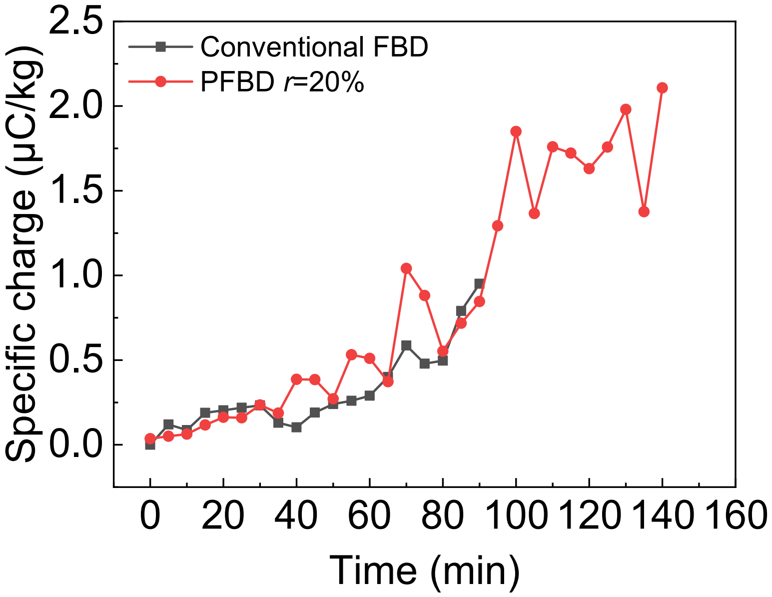

(a)

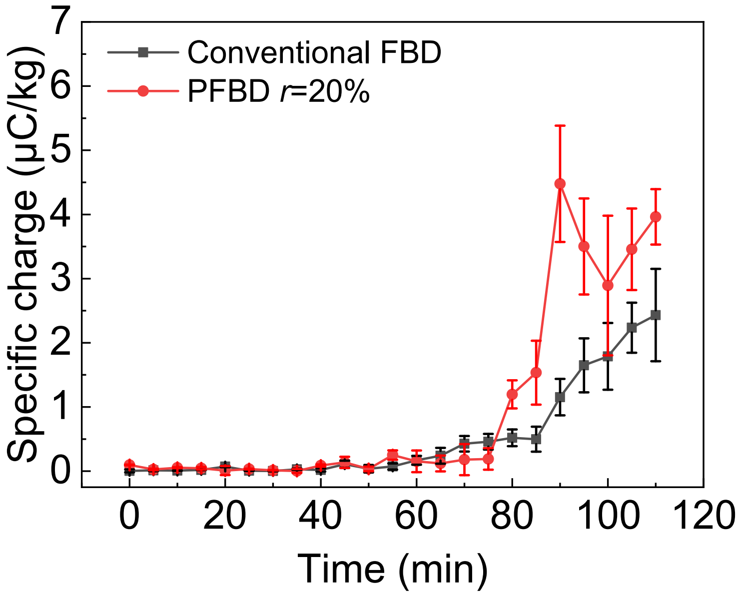

(b)

Figure 6.4 Effect of pulsation on tribocharging (a) U=4.0U_{mf}, (b) U=5.6U_{mf} with T=50°C, f=1.5 Hz, and r=20%.

6.4.2 Effect of superficial gas velocity

The effect of superficial gas velocity on tribocharging of pharmaceutical granules is shown in Figure 6.5. It can be seen that, in general, a higher superficial gas velocity results in a higher specific charge for both the conventional FBD and the PFBD. The differences under different superficial gas velocities are negligible at the constant rate period as most of the specific charges are lower than +0.25 μC/kg. During the falling rate period, higher superficial gas velocity results in a higher specific charge. More charge is generated due to the enhanced inter-particle and particle-wall collisions frequency and intensity caused by a higher superficial gas velocity [40]. During the drying operation, a higher superficial gas velocity also results in more particle entrainment. More entrained fine particles were found in the upper section and the fluidized bed dryer outlet at higher gas velocity. Fine pharmaceutical particles collected from the wall of the upper section of the bed were negatively charged. The specific charge of these fine particles is an order of magnitude higher than that of the granules in the product bowl of the fluidized bed [166, 174]. The separation of the fine entrained particles and the larger granules in the product bowl leads to the particles in the dense phase of the fluidized bed carrying more positive charges.

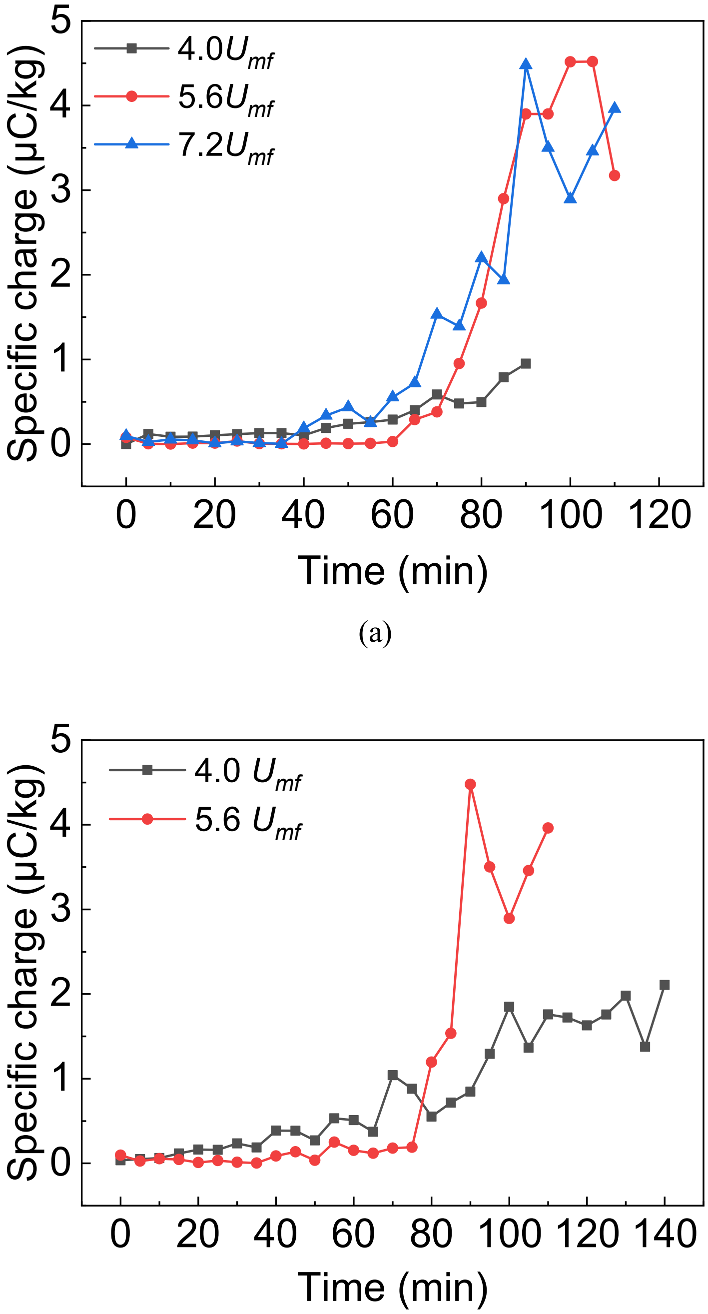

(a)

(b)

Figure 6.5 Effect of superficial gas velocity on drying (a) conventional FBD, (b) PFBD with T=50℃, f=1.5Hz and r=20%.

6.4.3 Effect of air temperature

The effect of air temperature on tribocharging of pharmaceutical granules is shown in Figure 6.6. Inlet air temperature plays an important role in the drying rate. However, the inlet air temperature does not have a significant impact on the specific charge carried. The pharmaceutical granules obtained during the falling rate period are close to each other. The average specific charge during the falling rate period was within the range of 1.85 to 2.23 μC/kg when the superficial gas velocity is $5.6U_{mf}$ in the conventional FBD. When the drying is conducted at the PFBD, the measured specific charge is within a narrow range from 2.19 to 2.33 μC/kg, indicating that the specific charge is not a function of the inlet air temperature in this study. Even though there are some studies have been reported on the effect of temperature on tribocharging, many of the results are contradictory, and the phenomenon cannot be explained [167, 175-177].

In order to further elucidate the relationship between the specific charge of pharmaceutical granules and the moisture content, the specific charge was plotted against moisture content, as shown in Figure 6.7. It was found that the specific charge at similar moisture contents is similar to each other even under different inlet air temperatures. This trend was observed in both the conventional FBD and PFBD.

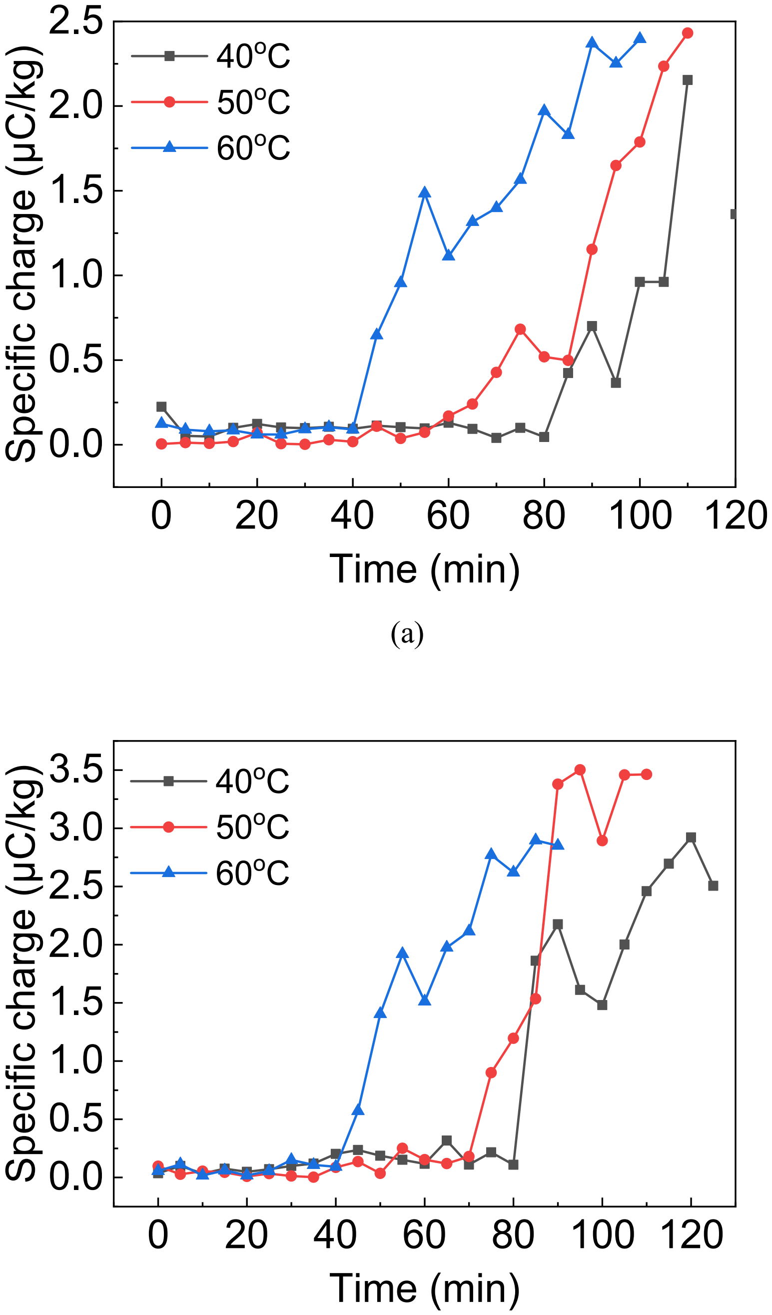

(a)

(b)

Figure 6.6 Effect of the inlet gas temperature on drying (a) conventional FBD, (b) PFBD with U=5.6 U_{mf} and f=1.5 Hz.

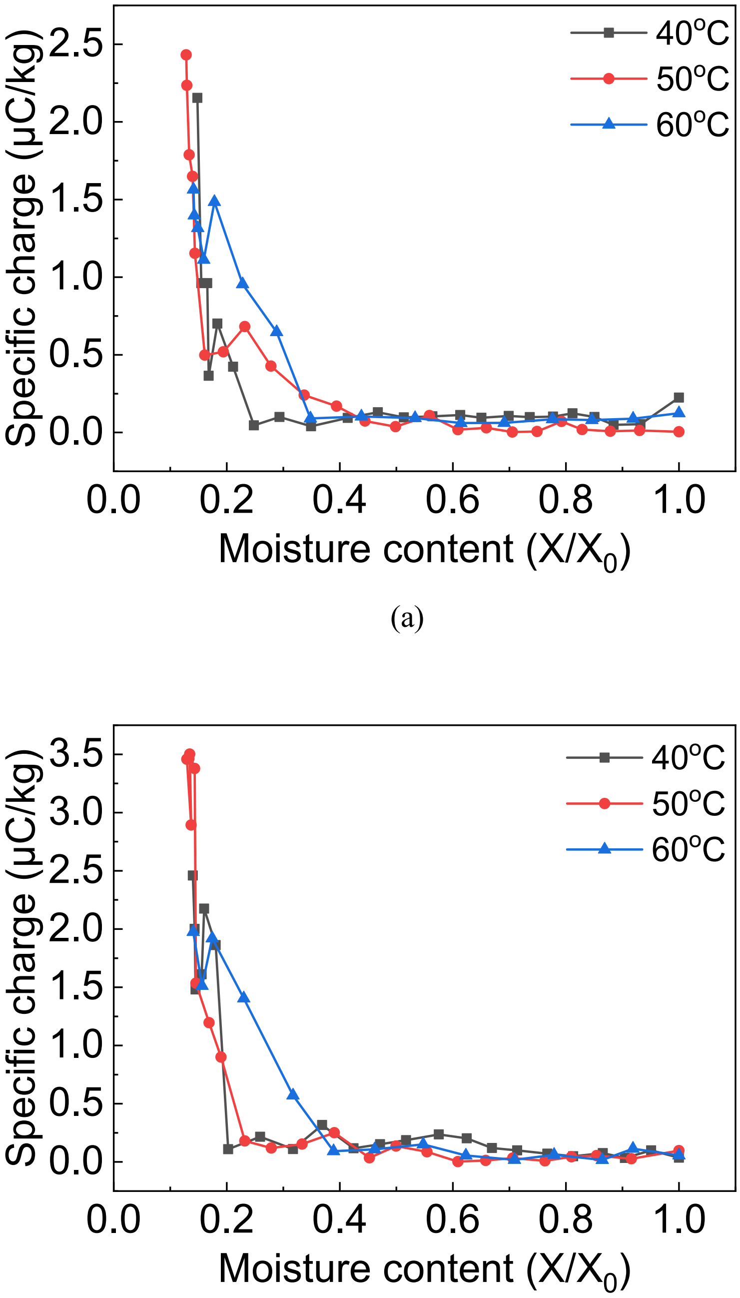

(a)

(b)

Figure 6.7 Specific charges against moisture content using (a) conventional FBD, (b) PFBD with U=5.6 U_{mf} and f=1.5 Hz.

6.4.4 Effect of pulsation frequency

The effect of the pulsation frequency on tribocharging at two superficial gas velocities is shown in Figure 6.8. It can be seen from Figure 6.8a that when the PFBD operated at a lower superficial gas velocity, the equilibrium value of the specific charge is not a function of the pulsation frequency. Most of the inter-particle and particle-wall collision happens in the product bowl. The entrained fine particle is much less compared with the PFBD operated at higher superficial gas velocity. Fine particles usually carry high negative charges [178]. When less entrained fine particles left the fluidized bed at a lower superficial gas velocity, particles that remained at the product bowl can obtain less positive charge. In addition, the granules charged with different polarity and magnitude orders were neutralized during the "OFF" period of the pulsation cycle. Thus, there is no apparent difference between PFBDs at different pulsation frequencies and the conventional FBD.

Compared with the conventional FBD and the PFBD operated at $4.0U_{mf}$, the pulsation frequency affects specific charge when the superficial gas velocity was increased from $4.0U_{mf}$ to $5.6U_{mf}$. During the constant rate period, the specific charge is low under all pulsation frequencies. During the falling rate period, the equilibrium specific charge decreased with higher pulsation frequencies.

The specific charge against moisture content is shown in Figure 6.9. It can be seen that, in general, granules in the PFBD obtain more specific charges than those in the conventional FBD. Lower pulsation frequency slightly enhances charge accumulation.

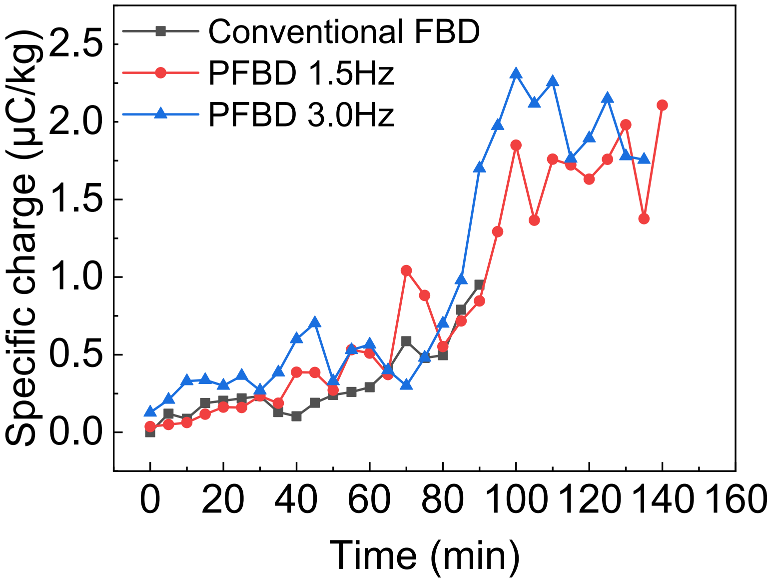

(a)

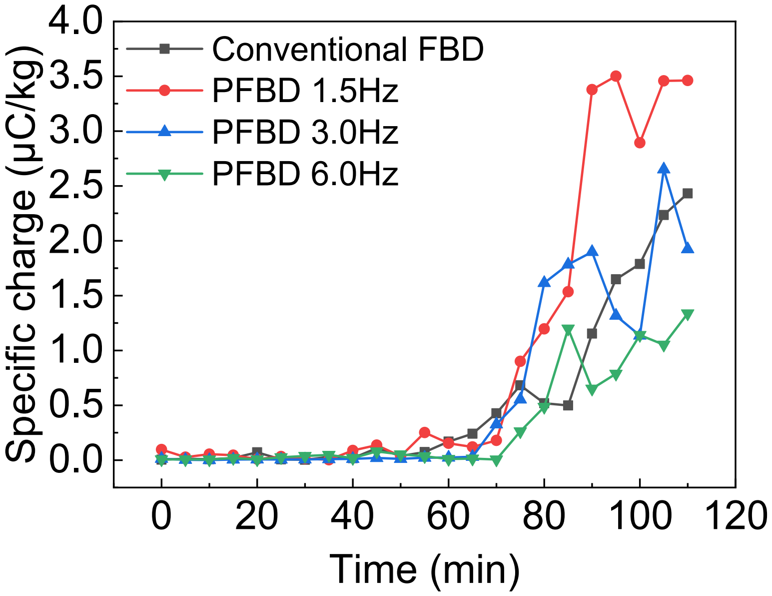

(b)

Figure 6.8 Effect of the pulsation frequency on tribocharging (a) U=4.0U_{mf}, (b) U=5.6U_{mf} with T=50°C and r=20%.

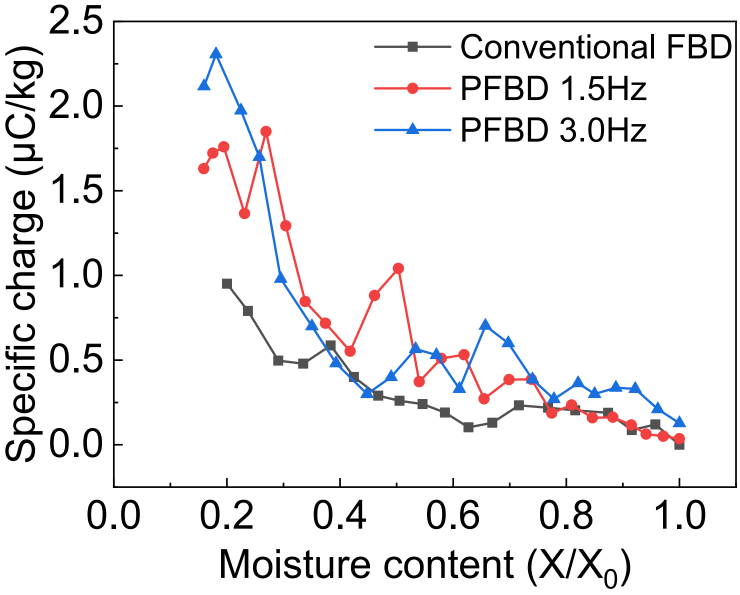

(a)

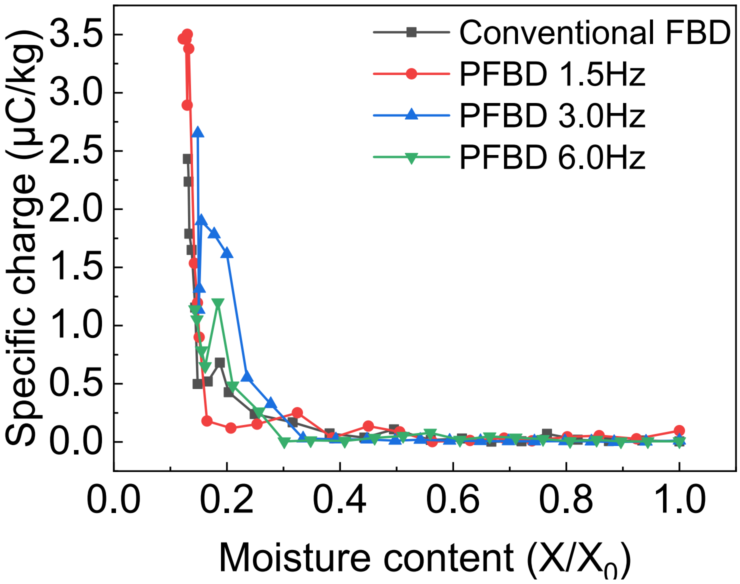

(b)

Figure 6.9 Specific charges against moisture content using (a) U=4.0U_{mf}, (b) U=5.6U_{mf} with T=50℃ and r= 20%.

6.4.5 Effect of pulsed air ratio

The effect of the pulsed air ratio on the specific charge is shown in Figure 6.10. Increasing the pulsed air ratio increases the specific charge during the constant rate period. A higher pulsed air ratio can generate a high peak pressure when the solenoid valve is switched from "OFF" status to "ON." The high instantaneous peak pressure generated a jet flow that can carry more entrained fine particles. A higher pulsed air ratio generates a higher instantaneous pressure, which leads to more entrainment. As a result, the specific charge increases. The specific charge continuously built up until the equilibrium was achieved. The equilibrium specific charge is not a function of the pulsed air ratio. For the PFBD and conventional FBD operated at $4.0U_{mf}$, the average equilibrium specific charge is around +2.0 μC/kg. For that operated at $5.6U_{mf}$, the average equilibrium specific charge is increased to around +4.0 μC/kg.

The effect of the pulsed air ratio on the specific charge at different moisture content is shown in Figure 6.11. It can be seen that at the same moisture content level, the PFBD with a higher pulsed air ratio generates more charge than the conventional FBD and PFDB with a lower pulsed air ratio. This effect is more evident when the FBD is operated at a higher superficial gas velocity.

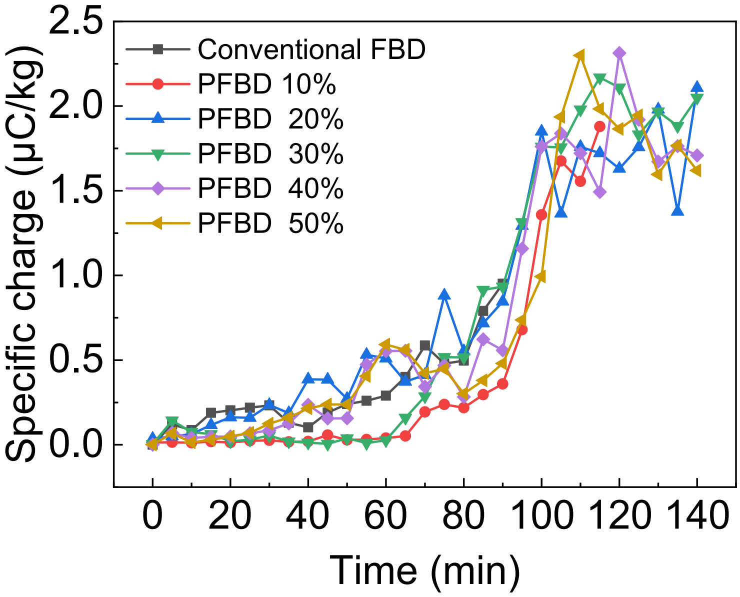

(a)

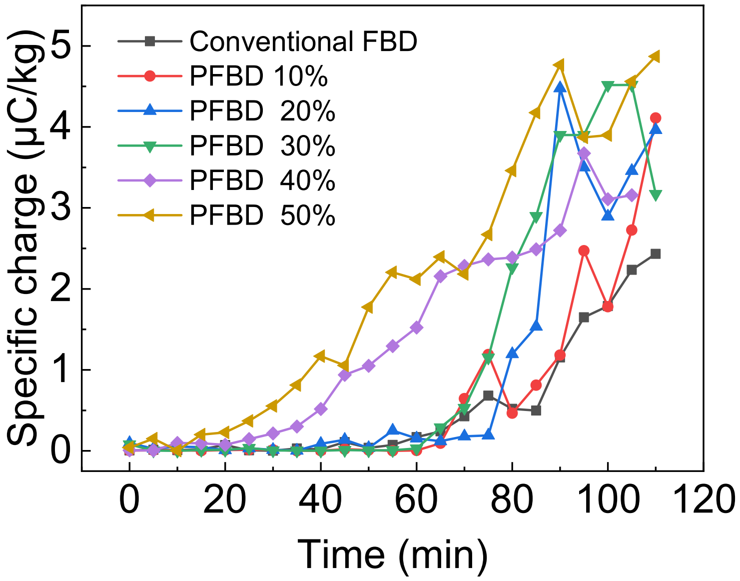

(b)

Figure 6.10 Effect of the pulsed air ratio on drying (a) U=4.0U_{mf}, (b) U=5.6U_{mf} with T=50℃ and f=1.5 Hz.

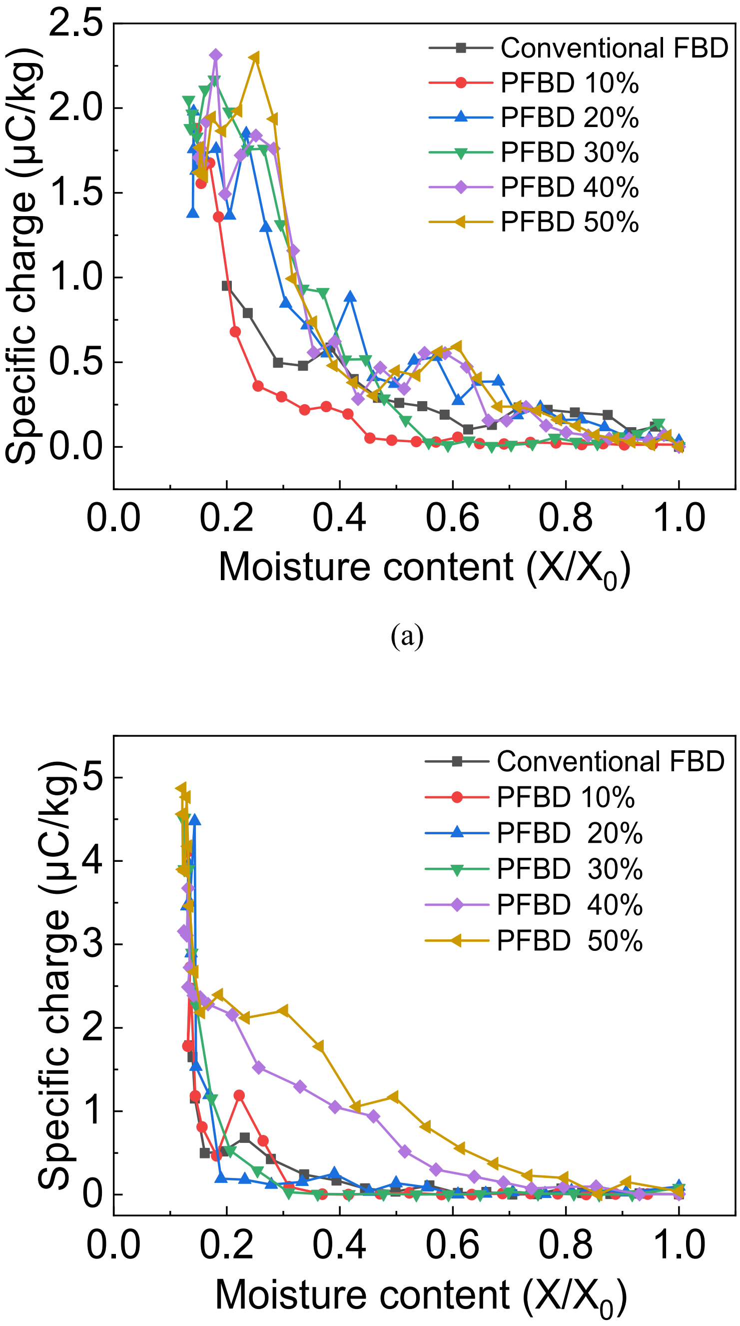

(a)

(b)

Figure 6.11 Specific charges against moisture content using (a) U=4.0U_{mf}, (b) U=5.6U_{mf} with T=50℃ and f=1.5 Hz.

6.4.6 Effect of API on tribocharging

Adding API changes the work function and morphology, which again might influence tribocharging behaviour [179]. The mixture without API has also been used to compare with the mixture with API. The results are shown in Figure 6.12. It is found that the mixture without API gathered more specific charge. The API used is APAP, which has the highest work function, 5.88Ev, as discussed in Appendix C. The addition of APAP increased the work function of the mixture, which makes the mixture with API hard to accumulate more positive charge. The specific charges against moisture content are shown in Figure 6.13. It can be seen that the granules without API can gather more positive specific charge than the granule with API at most moisture content, which is consistent with the hypothesis that adding API has changed the tribocharging behaviour of pharmaceutical mixture.

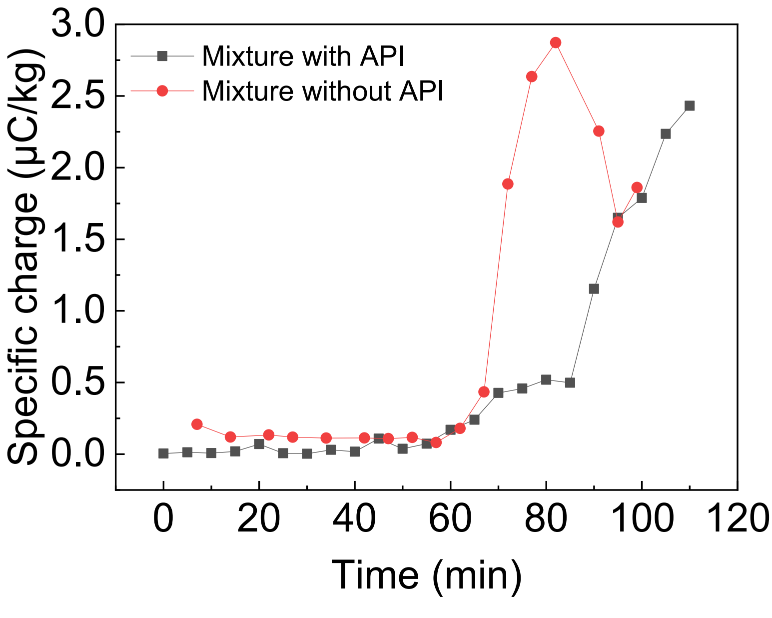

Figure 6.12 Effect of API on tribocharging with U=5.6U_{mf} and T=50°C.

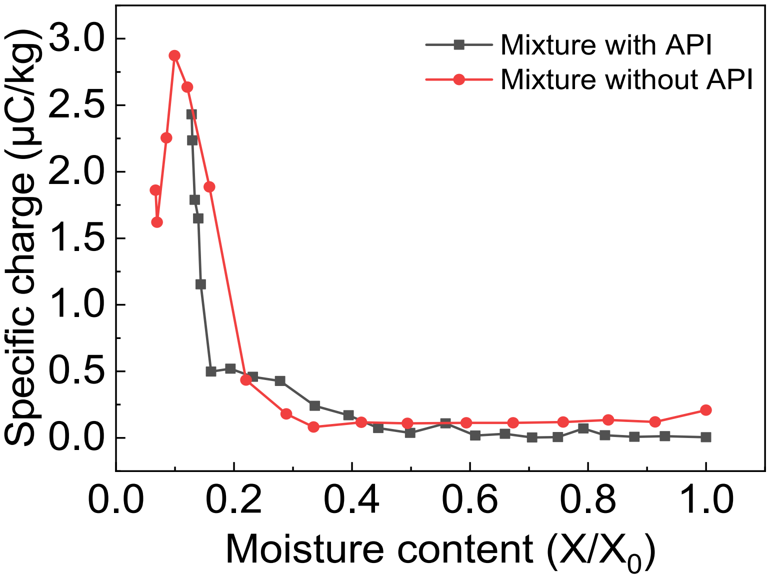

Figure 6.13 Specific charges against moisture content with U=5.6U_{mf} and T=50°C.

6.5 Conclusions

In this chapter, the tribocharging behaviour of pharmaceutical granules in a conventional FBD and a PFBD was studied to investigate the effect of superficial gas velocity, inlet air temperature, pulsation frequency, and pulsed air ratio on specific charge obtained.

During the drying process, the specific charge of pharmaceutical granules remained lower than 0.2 μC/kg during the constant rate period. When the moisture content was reduced to a critical moisture content, namely 10 wb %, the specific charge increased sharply regardless of the superficial gas velocity and inlet air temperature applied. The specific charge amount accumulated during the falling rate period before reach an equilibrium value. During the increasing trend, the fluctuations of the specific charge are caused by discharge and charge neutralization. The equilibrium specific charge is influenced by the superficial gas velocity and pulsation frequency. Higher superficial gas velocity and lower pulsed frequency have an enhanced effect on the specific charge. When the superficial gas velocity is low, there is no noticeable difference between the conventional FBD and PFBD with different pulsation frequencies. The inlet air temperature and pulsed air ratio did not significantly impact the equilibrium specific charge value.

CHAPTER 7. CONCLUSIONS

7.1 Summary of results

During the granulation process of pharmaceutical powders, powders with higher hydrophilicity (smaller contact angle) are more likely to form granules with lower sphericity (plate-shaped), and lower hydrophilicity (larger contact angle) will result in more spherical granules.

The fluid movement beneath the powder bed surface and the interaction between the pharmaceutical powders and liquid binder were observed with high speed and high-resolution X-ray images.

For coarse powders, granulation processes with droplets released at a lower height result in the spreading mechanism. In contrast, the processes with higher droplet release heights result in the crater formation mechanism. Decreasing the particle size leads to the tunneling mechanism, and the resultant final granules are rounder than those generated with powders of larger particle size.

The overall movement ratio, r_m, was introduced to describe the fluid movement during the granulation process quantitatively. When the overall movement ratio, r_m, is larger than 1, the liquid moves faster in the vertical direction, which can be described as penetration. When the overall movement ratio, r_m, is smaller than 1, the liquid moves faster in the radial direction, spreading.

Higher superficial gas velocity and lower inlet air temperature are observed to have enhanced effects on drying. A lower pulsation frequency is more favorable to improve the drying rate than a high pulsation frequency. The impact of the pulsed air ratio is dependent on the superficial gas velocity. At the low superficial gas velocity, increasing the pulsed air ratio helps enhance the drying rate. In contrast, at the high superficial gas velocity, the drying rate is higher at a higher pulsed air ratio. Among the nine thin-layer models examined, the Midilli and Kucuk model shows the best performance in predicting the drying curve due to the addition of linear term, which reflects the difference between constant rate period and falling rate period.

During the drying process, the specific charge of pharmaceutical granules remained lower than 0.2 µC/kg during the constant rate period. When the moisture content was reduced to a critical moisture content, namely 10%, the specific charge increased sharply regardless of the superficial gas velocity and inlet air temperature. The specific charge amount accumulated during the falling rate period before reaching an equilibrium value. During the increasing trend, the fluctuations of the specific charge are caused by discharge and charge neutralization. The equilibrium specific charge is found to be influenced by the superficial gas velocity and pulsation frequency. Higher superficial gas velocity and lower pulsed frequency have an enhanced effect on the specific charge. When the superficial gas velocity is low, there is no noticeable difference between the conventional FBD and the PFBD with different pulsation frequencies. The inlet air temperature and pulsed air ratio were not found to significantly impact the equilibrium specific charge value.

7.2 Conclusions

In-situ synchrotron X-ray imaging can be used to quantitatively study the dynamic wet granulation process with a single drop impacting method. In general, the porosity of the granule decreases from the top part to the bottom part of the granule.

The particle properties, including size and hydrophilicity, and liquid properties, including droplet volume and release height, have significant influences on the granulation process.

The added pulsed air is an effective method to enhance drying at a high superficial gas velocity when the solid is maintained at minimum fluidization by the continuous gas flow. In general, the PFBD shows higher energy efficiency than the conventional FBD.

The specific charge of pharmaceutical granules is mainly influenced by the moisture content. When the moisture content was reduced to a critical moisture content, namely 10%, the specific charge increased sharply regardless of the superficial gas velocity and inlet air temperature.

CHAPTER 8. RECOMMENDATIONS FOR FUTURE RESEARCH

This study has shown that synchrotron X-ray computed tomography is a promising tool to study the wet granulation process using the single drop impact method. Some further improvement can be made to have better image quality, higher scan speed, and a larger field of view.

This study has placed a focus on the static three-dimensional image reconstruction of final granules. The same method can also be applied to visualize the dynamic 3-dimensional granulation process. When more 3D image results are obtained, the overall porosity and structure of the granules can be analyzed.

The dynamic projectional wet granulation image study focuses on operating parameters like liquid binder type, droplet volume, droplet release height, and particle size. However, a limited operating range of these parameters has been explored. Also, the particle size distribution of pharmaceutical powder used in this study is broad. More uniform particles are needed. The X-ray absorption of the APIs and excipients is close to each other, making it hard to tell them apart under X-ray images. The segregation and distribution of different components within the granules can be studied if powders with very different x-ray absorption are selected.

The drying process of pharmaceutical granules within the conventional FBD and PFBD has been explored. Under low superficial gas velocity, pulsed air did not show significant impacts on drying. However, pulsation can be coupled with mechanical vibration to eliminate channeling at low superficial gas velocity. Other critical operating parameters, such as bed height and relative humidity, still need to be investigated. The moisture distribution at different radial and vertical locations should be studied in future work. The tribocharging distribution at different radial and the vertical location is also expected to be studied in future works. In order to avoid experimental errors from the manual sampling method, a Faraday cup-type fluidized bed dryer can be used to monitor dynamic changes of electrostatic charges during the drying process.

REFERENCES

[1] A. Kumar, K.V. Gernaey, T.D. Beer, I. Nopens, Model-based analysis of high shear wet granulation from batch to continuous processes in pharmaceutical production – A critical review, European Journal of Pharmaceutics and Biopharmaceutics, 85 (2013) 814-832.

[2] R.M. Dhenge, J.J. Cartwright, M.J. Hounslow, A.D. Salman, Twin screw granulation: Steps in granule growth, International Journal of Pharmaceutics, 438 (2012) 20-32.

[3] P. Soyeux, A. Delacourte, B. Delie, P. Lefevre, B. Boniface, Influence and optimisation of operating parameters with a new binder in wet granulation. I: use in powder form, European Journal of Pharmaceutics and Biopharmaceutics, 46 (1998) 95-103.

[4] A. Faure, P. York, R. Rowe, Process control and scale-up of pharmaceutical wet granulation processes: a review, European Journal of Pharmaceutics and Biopharmaceutics, 52 (2001) 269-277.

[5] E.M. Hansuld, L. Briens, A review of monitoring methods for pharmaceutical wet granulation, International Journal of Pharmaceutics, 472 (2014) 192-201.

[6] P. Kleinebudde, Roll compaction/dry granulation: pharmaceutical applications, European Journal of Pharmaceutics and Biopharmaceutics, 58 (2004) 317-326.

[7] S. Mangal, F. Meiser, D. Morton, I. Larson, Particle engineering of excipients for direct compression: understanding the role of material properties, Current Pharmaceutical Design, 21 (2015) 5877-5889.

[8] P. Suresh, I. Sreedhar, R. Vaidhiswaran, A. Venugopal, A comprehensive review on process and engineering aspects of pharmaceutical wet granulation, Chemical Engineering Journal, 328 (2017) 785-815.

[9] S.D. Schaber, D.I. Gerogiorgis, R. Ramachandran, J.M.B. Evans, P.I. Barton, B.L. Trout, Economic analysis of integrated continuous and batch pharmaceutical manufacturing: a case study, Industrial & Engineering Chemistry Research, 50 (2011) 10083-10092.

[10] S. Simons, R. Fairbrother, Direct observations of liquid binder–particle interactions: the role

of wetting behaviour in agglomerate growth, Powder Technology, 110 (2000) 44-58.

[11] H.G. Kristensen, T. Schaefer, Granulation: a review on pharmaceutical wet-granulation, Drug Development and Industrial Pharmacy, 13 (1987) 803-872.

[12] D. Zhang, J.H. Flory, S. Panmai, U. Batra, M.J. Kaufman, Wettability of pharmaceutical solids: its measurement and influence on wet granulation, Colloids and Surfaces A: Physicochemical and Engineering Aspects, 206 (2002) 547-554.

[13] B.J. Ennis, J. Li, T. Gabriel I, P. Robert, The influence of viscosity on the strength of an axially strained pendular liquid bridge, Chemical Engineering Science, 45 (1990) 3071-3088.

[14] B.J. Ennis, G. Tardos, R. Pfeffer, A microlevel-based characterization of granulation phenomena, Powder Technology, 65 (1991) 257-272.

[15] A. El Hagrasy, P. Cruise, I. Jones, J. Litster, In-line size monitoring of a twin screw granulation process using high-speed imaging, Journal of Pharmaceutical Innovation, 8 (2013) 90-98.

[16] A. Kumar, J. Dhondt, F. De Leersnyder, J. Vercruysse, V. Vanhoorne, C. Vervaet, J.P. Remon, K.V. Gernaey, T. De Beer, I. Nopens, Evaluation of an in-line particle imaging tool for monitoring twin-screw granulation performance, Powder Technology, 285 (2015) 80-87.

[17] V. Rimpiläinen, S. Poutiainen, L.M. Heikkinen, T. Savolainen, M. Vauhkonen, J. Ketolainen, Electrical capacitance tomography as a monitoring tool for high-shear mixing and granulation, Chemical Engineering Science, 66 (2011) 4090-4100.

[18] K. Hapgood, L. Farber, J.N. Michaels, Agglomeration of hydrophobic powders via solid spreading nucleation, Powder Technology, 188 (2009) 248-254.

[19] S. Poutiainen, J. Pajander, A. Savolainen, J. Ketolainen, K. Jarvinen, Evolution of granule structure and drug content during fluidized bed granulation by X-ray microtomography and confocal Raman spectroscopy, Journal of Pharmaceutical Sciences, 100 (2011) 5254-5269.

[20] H.N. Emady, D. Kayrak-Talay, W.C. Schwerin, J.D. Litster, Granule formation mechanisms and morphology from single drop impact on powder beds, Powder Technology, 212 (2011) 69-79.

[21] D. Geldart, Types of gas fluidization, Powder Technology, 7 (1973) 285-292.

[22] B. Guignon, A. Duquenoy, E.D. Dumoulin, Fluid bed encapsulation of particles: principles and practice, Drying Technology, 20 (2002) 419-447.

[23] S.K. Chou, K.J. Chua, New hybrid drying technologies for heat sensitive foodstuffs, Trends in Food Science & Technology, 12 (2001) 359-369.

[24] W. Senadeera, B.R. Bhandari, G. Young, B. Wijesinghe, Influence of shapes of selected vegetable materials on drying kinetics during fluidized bed drying, Journal of Food Engineering, 58 (2003) 277-283.

[25] S. Giner, A. Calvelo, Modelling of wheat drying in fluidized beds, Journal of Food Science, 52 (1987) 1358-1363.

[26] M. Hemati, R. Cherif, K. Saleh, V. Pont, Fluidized bed coating and granulation: influence of process-related variables and physicochemical properties on the growth kinetics, Powder Technology, 130 (2003) 18-34.

[27] S. Poutiainen, M. Honkanen, J. Becker, D. Nachtweide, K. Järvinen, J. Ketolainen, X-ray microtomography analysis of intragranular drug migration during fluidized bed and oven tray drying, Journal of Pharmaceutical Sciences, 101 (2012) 1587-1598.

[28] M. Dosta, S. Antonyuk, S. Heinrich, Multiscale simulation of agglomerate breakage in fluidized beds, Industrial & Engineering Chemistry Research, 52 (2013) 11275-11281.

[29] A. Chandran, S.S. Rao, Y. Varma, Fluidized bed drying of solids, AIChE Journal, 36 (1990) 29-38.

[30] C. Bemrose, J. Bridgwater, A review of attrition and attrition test methods, Powder Technology, 49 (1987) 97-126.

[31] C. Wen, L. Chen, Fluidized bed freeboard phenomena: entrainment and elutriation, AIChE Journal, 28 (1982) 117-128.

[32] E. Marring, A. Hoffmann, L. Janssen, The effect of vibration on the fluidization behaviour of some cohesive powders, Powder Technology, 79 (1994) 1-10.

[33] M. Taghavivand, K. Choi, L. Zhang, Investigation on drying kinetics and tribocharging

behaviour of pharmaceutical granules in a fluidized bed dryer, Powder Technology, 316 (2016) 171-180.

[34] G. Askari, Z. Emam-Djomeh, S. Mousavi, An investigation of the effects of drying methods and conditions on drying characteristics and quality attributes of agricultural products during hot air and hot air/microwave-assisted dehydration, Drying Technology, 27 (2009) 831-841.

[35] W.L. Davies, W.T. Gloor, Batch production of pharmaceutical granulations in a fluidized bed I: Effects of process variables on physical properties of final granulation, Journal of Pharmaceutical Sciences, 60 (1971) 1869-1874.

[36] Y.H. Xie, L. Chen, C.H. Lin, S. Du, Experimental research on granule moisture measurement by microwave resonance technology in a fluidized bed dryer, Key Engineering Materials, 544 (2013) 466-470.

[37] T.J. Jamaleddine, M.B. Ray, Application of computational fluid dynamics for simulation of drying processes: a review, Drying technology, 28 (2010) 120-154.

[38] H. Liu, M. Li, Two-compartmental population balance modeling of a pulsed spray fluidized bed granulation based on computational fluid dynamics (CFD) analysis, International Journal of Pharmaceutics, 475 (2014) 256-269.

[39] W.R.W. Daud, Fluidized bed dryers—recent advances, Advanced Powder Technology, 19 (2008) 403-418.

[40] J. Burgschweiger, E. Tsotsas, Experimental investigation and modelling of continuous fluidized bed drying under steady-state and dynamic conditions, Chemical Engineering Science, 57 (2002) 5021-5038.

[41] A. Kaleta, K. Górnicki, R. Winiczenko, A. Chojnacka, Evaluation of drying models of apple (var. Ligol) dried in a fluidized bed dryer, Energy Conversion and Management, 67 (2013) 179-185.

[42] S. Meziane, Drying kinetics of olive pomace in a fluidized bed dryer, Energy Conversion and Management, 52 (2011) 1644-1649.

[43] J. Cross, Electrostatics, principles, problems and applications, CRC Press, 1987.

[44] M. Glor, Ignition hazard due to static electricity in particulate processes, Powder Technology, 135-136 (2003) 223-233.

[45] D.M. Adams, L. Brus, C.E. Chidsey, S. Creager, C. Creutz, C.R. Kagan, P.V. Kamat, M. Lieberman, S. Lindsay, R.A. Marcus, Charge transfer on the nanoscale: current status, The Journal of Physical Chemistry B, 107 (2003) 6668-6697.

[46] L.-S. Fan, C. Zhu, Principles of gas-solid flows, (1999).

[47] D.J. Lacks, R.M. Sankaran, Contact electrification of insulating materials, Journal of Physics D: Applied Physics, 44 (2011) 453001.

[48] L.S. McCarty, G.M. Whitesides, Electrostatic charging due to separation of ions at interfaces: contact electrification of ionic electrets, Angewandte Chemie International Edition, 47 (2008) 2188-2207.

[49] M.D. Scanlon, P. Peljo, M.A. Méndez, E. Smirnov, H.H. Girault, Charging and discharging at the nanoscale: Fermi level equilibration of metallic nanoparticles, Chemical Science, 6 (2015) 2705-2720.

[50] P. Peljo, J.A. Manzanares, H.H. Girault, Contact potentials, fermi level equilibration, and surface charging, Langmuir, 32 (2016) 5765-5775.

[51] W. Dolan, W. Dyke, Temperature-and-field emission of electrons from metals, Physical Review, 95 (1954) 327.

[52] M. Chung, P. Cutler, N. Miskovsky, T. Sullivan, Energy exchange processes in electron emission at high fields and temperatures, Journal of Vacuum Science & Technology B: Microelectronics and Nanometer Structures Processing, Measurement, and Phenomena, 12 (1994) 727-736.

[53] F.S. Ali, M.A. Ali, R.A. Ali, I.I. Inculet, Minority charge separation in falling particles with bipolar charge, Journal of Electrostatics, 45 (1998) 139-155.

[54] A. Wolny, I. Opalinski, Electric charge neutralization by addition of fines to a fluidized bed

composed of coarse dielectric particles, Journal of Electrostatics, 14 (1983) 279-289.

[55] H. Zhao, G. Castle, I. Inculet, A. Bailey, Bipolar charging in polydisperse polymer powders in industrial processes, Conference Record of the 2000 IEEE Industry Applications Conference. Thirty-Fifth IAS Annual Meeting and World Conference on Industrial Applications of Electrical Energy (Cat. No. 00CH37129), IEEE, 2000, pp. 835-841.

[56] A. Sowinski, F. Salama, P. Mehrani, New technique for electrostatic charge measurement in gas–solid fluidized beds, Journal of Electrostatics, 67 (2009) 568-573.

[57] J.B. Gajewski, B. Gload, W. Kala, Electrostatic method for measuring the two-phase pipe flow parameters, Industry Applications Society Annual Meeting, 1990., Conference Record of the 1990 IEEE, IEEE, 1990, pp. 897-902.

[58] H. Masuda, S. Matsusaka, S. Nagatani, Measurements of powder flow rate in gas-solids pipe flow based on the static electrification of particles, Advanced Powder Technology, 5 (1994) 241-254.

[59] Y. Yan, B. Byrne, S. Woodhead, J. Coulthard, Velocity measurement of pneumatically conveyed solids using electrodynamic sensors, Measurement Science and Technology, 6 (1995) 515.

[60] Y. Yan, Mass flow measurement of bulk solids in pneumatic pipelines, Measurement Science and Technology, 7 (1996) 1687.

[61] J.B. Gajewski, Electrostatic flow probe and measuring system calibration for solids mass flow rate measurement, Journal of Electrostatics, 45 (1999) 255-264.

[62] G. Hearn, J. Ballard, The use of electrostatic techniques for the identification and sorting of waste packaging materials, Resources, Conservation and Recycling, 44 (2005) 91-98.

[63] J.B. Gajewski, Electrostatic, inductive ring probe bandwidth, Measurement Science and Technology, 7 (1996) 1766.

[64] A. Pedersen, On the electrostatics of probe measurements of surface charge densities, Gaseous Dielectrics V, Elsevier, 1987, pp. 235-241.

[65] S.M. Iveson, J.D. Litster, K. Hapgood, B.J. Ennis, Nucleation, growth and breakage phenomena in agitated wet granulation processes: a review, Powder Technology, 117 (2001) 3-39.

[66] K.P. Hapgood, J.D. Litster, S.R. Biggs, T. Howes, Drop penetration into porous powder beds, Journal of Colloid and Interface Science, 253 (2002) 353-366.

[67] N.B. Davis, K. Waibel, K. Wang, J.D. Litster, Microstructure of single-droplet granules formed from ultra-fine powders, Powder Technology, 305 (2017) 19-26.

[68] A.M. Bouwman, J.C. Bosma, P. Vonk, J.H.A. Wesselingh, H.W. Frijlink, Which shape factor (s) best describe granules?, Powder Technology, 146 (2004) 66-72.

[69] A.L. Mundozah, J.J. Cartwright, C.C. Tridon, M.J. Hounslow, A.D. Salman, Hydrophobic/hydrophilic static powder beds: Competing horizontal spreading and vertical imbibition mechanisms of a single droplet, Powder Technology, 330 (2018) 275-283.

[70] B.Y. Shekunov, P. Chattopadhyay, H.H. Tong, A.H. Chow, Particle size analysis in pharmaceutics: principles, methods and applications, Pharmaceutical Research, 24 (2007) 203-227.

[71] J.K.S. De Souza, M.A. da Silva Pinto, P.G. Vieira, J. Baron, C.J. Tierra-Criollo, An open-source, FireWire camera-based, Labview-controlled image acquisition system for automated, dynamic pupillometry and blink detection, Computer Methods and Programs in Biomedicine, 112 (2013) 607-623.

[72] H. Yamada, K. Masuda, T. Ishige, K. Fujii, H. Uekusa, K. Miura, E. Yonemochi, K. Terada, Potential of synchrotron X-ray powder diffractometry for detection and quantification of small amounts of crystalline drug substances in pharmaceutical tablets, Journal of Pharmaceutical and Biomedical Analysis, 56 (2011) 448-453.

[73] S. Noguchi, R. Kajihara, Y. Iwao, Y. Fujinami, Y. Suzuki, Y. Terada, K. Uesugi, K. Miura, S. Itai, Investigation of internal structure of fine granules by microtomography using synchrotron X-ray radiation, International Journal of Pharmaceutics, 445 (2013) 93-98.

[74] R. Liu, X. Yin, H. Li, Q. Shao, P. York, Y. He, T. Xiao, J. Zhang, Visualization and quantitative

profiling of mixing and segregation of granules using synchrotron radiation X-ray microtomography and three dimensional reconstruction, International Journal of Pharmaceutics, 445 (2013) 125-133.

[75] A. Buleon, B. Pontoire, C. Riekel, H. Chanzy, W. Helbert, R. Vuong, Crystalline ultrastructure of starch granules revealed by synchrotron radiation microdiffraction mapping, Macromolecules, 30 (1997) 3952-3954.

[76] H. Xi Yuan, M.J. Rosen, Dynamic surface tension of aqueous surfactant solutions: I. Basic paremeters, Journal of Colloid and Interface Science, 124 (1988) 652-659.

[77] S. Wang, X. Huang, C. Yang, Mixing enhancement for high viscous fluids in a microfluidic chamber, Lab on a Chip, 11 (2011) 2081-2087.

[78] S. Oka, H. Emady, O. Kašpar, V. Tokárová, F. Muzzio, F. Štěpánek, R. Ramachandran, The effects of improper mixing and preferential wetting of active and excipient ingredients on content uniformity in high shear wet granulation, Powder Technology, 278 (2015) 266-277.

[79] H.N. Emady, D. Kayrak-Talay, J.D. Litster, A regime map for granule formation by drop impact on powder beds, AIChE Journal, 59 (2013) 96-107.

[80] P. Rahimian, L. Battrell, R. Anderson, N. Zhu, E. Johnson, L. Zhang, Investigation of time dependent water droplet dynamics on porous fuel cell material via synchrotron based X-ray imaging technique, Experimental Thermal and Fluid Science, 97 (2018) 237-245.

[81] T. Gao, A.S.S. Singaravelu, S. Oka, R. Ramachandran, F. Štepánek, N. Chawla, H.N. Emady, Granule formation and structure from single drop impact on heterogeneous powder beds, International Journal of Pharmaceutics, 552 (2018) 56-66.

[82] V. Schiller, A drag coefficient correlation, Z. Vereines Ingenieure, 77 (1933) 318-320.

[83] A.M. Bouwman, J.C. Bosma, P. Vonk, J.A. Wesselingh, H.W. Frijlink, Which shape factor(s) best describe granules?, Powder Technology, 146 (2004) 66-72.

[84] N.B. Davis, K. Waibel, K. Wang, J.D. Litster, Microstructure of single-droplet granules formed from ultra-fine powders, Powder Technology, 305 (2017) 19-26.

[85] S.M. Iveson, J.D. Litster, B.J. Ennis, Fundamental studies of granule consolidation Part 1: Effects of binder content and binder viscosity, Powder Technology, 88 (1996) 15-20.

[86] S.T. Keningley, P.C. Knight, A.D. Marson, An investigation into the effects of binder viscosity on agglomeration behaviour, Powder Technology, 91 (1997) 95-103.

[87] N. Ouchiyama, T. Tanaka, Stochastic model for compaction of pellets in granulation, Industrial & Engineering Chemistry Process Design and Development, 19 (1980) 555-560.

[88] S.M. Iveson, J.D. Litster, Fundamental studies of granule consolidation part 2: quantifying the effects of particle and binder properties, Powder Technology, 99 (1998) 243-250.

[89] B. Crean, A. Parker, D.L. Roux, M. Perkins, S.Y. Luk, S.R. Banks, C.D. Melia, C.J. Roberts, Elucidation of the internal physical and chemical microstructure of pharmaceutical granules using X-ray micro-computed tomography, Raman microscopy and infrared spectroscopy, European Journal of Pharmaceutics and Biopharmaceutics, 76 (2010) 498-506.

[90] S. Poutiainen, J. Pajander, A. Savolainen, J. Ketolainen, K. Järvinen, Evolution of granule structure and drug content during fluidized bed granulation by X-ray microtomography and confocal Raman spectroscopy, Journal of Pharmaceutical Sciences, 100 (2011) 5254-5269.

[91] K.P. Hapgood, L. Farber, J.N. Michaels, Agglomeration of hydrophobic powders via solid spreading nucleation, Powder Technology, 188 (2009) 248-254.

[92] H.N. Emady, D. Kayrak-Talay, J.D. Litster, A regime map for granule formation by drop impact on powder beds, AIChE Journal, 59 (2013) 96-107.

[93] M. Liu, J. Wu, Y. Gan, D.A. Hanaor, C. Chen, Evaporation limited radial capillary penetration in porous media, Langmuir, 32 (2016) 9899-9904.

[94] K.P. Hapgood, B. Khanmohammadi, Granulation of hydrophobic powders, Powder Technology, 189 (2009) 253-262.

[95] C. Li, N. Zhu, H.N. Emady, L. Zhang, Synchrotron-based X-ray in-situ imaging techniques for advancing the understanding of pharmaceutical granulation, International Journal of Pharmaceutics, 572 (2019) 118797.

[96] X.L. Lu, Q. Zheng, X.Z. Yin, G.Q. Xiao, Z.H. Liao, M. Yang, J.W. Zhang, Quantitative structure characteristics and fractal dimension of Chinese medicine granules measured by synchrotron radiation X-ray computed micro tomography, Yao Xue Xue Bao, 50 (2015) 767-774.

[97] A. Buléon, B. Pontoire, C. Riekel, H. Chanzy, W. Helbert, R. Vuong, Crystalline Ultrastructure of Starch Granules Revealed by Synchrotron Radiation Microdiffraction Mapping, Macromolecules, 30 (1997) 3952-3954.

[98] S. Dale, C. Wassgren, J. Litster, Measuring granule phase volume distributions using X-ray microtomography, Powder Technology, 264 (2014) 550-560.

[99] S. Noguchi, R. Kajihara, Y. Iwao, Y. Fujinami, Y. Suzuki, Y. Terada, K. Uesugi, K. Miura, S. Itai, Investigation of internal structure of fine granules by microtomography using synchrotron X-ray radiation, International Journal of Pharmaceutics, 445 (2013) 93-98.

[100] H. Aoki, Y. Iwao, M. Mizoguchi, S. Noguchi, S. Itai, Clarithromycin highly-loaded gastro-floating fine granules prepared by high-shear melt granulation can enhance the efficacy of Helicobacter pylori eradication, European Journal of Pharmaceutics and Biopharmaceutics, 92 (2015) 22-27.

[101] R.M. Dhenge, J.J. Cartwright, D.G. Doughty, M.J. Hounslow, A.D. Salman, Twin screw wet granulation: Effect of powder feed rate, Advanced Powder Technology, 22 (2011) 162-166.

[102] R. Liu, X. Yin, H. Li, Q. Shao, P. York, Y. He, T. Xiao, J. Zhang, Visualization and quantitative profiling of mixing and segregation of granules using synchrotron radiation X-ray microtomography and three dimensional reconstruction, International Journal of Pharmaceutics, 445 (2013) 125-133.

[103] E. Gallucci, K. Scrivener, A. Groso, M. Stampanoni, G. Margaritondo, 3D experimental investigation of the microstructure of cement pastes using synchrotron X-ray microtomography (μCT), Cement and Concrete Research, 37 (2007) 360-368.

[104] B. Cai, S. Karagadde, L. Yuan, T.J. Marrow, T. Connolley, P.D. Lee, In situ synchrotron tomographic quantification of granular and intragranular deformation during semi-solid

compression of an equiaxed dendritic Al–Cu alloy, Acta Materialia, 76 (2014) 371-380.

[105] Y. Nishiyama, J.-l. Putaux, N. Montesanti, J.-L. Hazemann, C. Rochas, B→A allomorphic transition in native starch and amylose spherocrystals monitored by in situ synchrotron X-ray diffraction, Biomacromolecules, 11 (2010) 76-87.

[106] M.-C. Schlegel, A. Sarfraz, U. Müller, U. Panne, F. Emmerling, First seconds in a building's life—in situ synchrotron X-ray diffraction study of cement hydration on the millisecond timescale, Angewandte Chemie International Edition, 51 (2012) 4993-4996.

[107] Z. Cheng, J. Wang, M.R. Coop, G. Ye, A miniature triaxial apparatus for investigating the micromechanics of granular soils with in situ X-ray micro-tomography scanning, Frontiers of Structural and Civil Engineering, 14 (2020) 357-373.

[108] M. Sistaninia, S. Terzi, A.B. Phillion, J.M. Drezet, M. Rappaz, 3-D granular modeling and in situ X-ray tomographic imaging: a comparative study of hot tearing formation and semi-solid deformation in Al–Cu alloys, Acta Materialia, 61 (2013) 3831-3841.

[109] D.M. Parikh, Handbook of pharmaceutical granulation technology, Drugs and the Pharmaceutical Sciences, 198 (1997) 175-184.

[110] M.W. Scott, H.A. Lieberman, A.S. Rankell, F.S. Chow, G.W. Johnston, Drying as a unit operation in the pharmaceutical industry I. Drying of tablet granulations in fluidized beds, Journal of Pharmaceutical Sciences, 52 (1963) 284-291.

[111] S. Tirawanichakul, S. Prachayawarakorn, W. Varanyanond, P. Tungtrakul, S. Soponronnarit, Effect of fluidized bed drying temperature on various quality attributes of paddy, Drying Technology, 22 (2004) 1731-1754.

[112] N.V. Menshutina, M.G. Gordienko, A.A. Voynovskiy, T. Kudra, Dynamic analysis of drying energy consumption, Drying Technology, 22 (2004) 2281-2290.

[113] T. Kudra, Energy aspects in drying, Drying Technology, 22 (2004) 917-932.

[114] G. Chaplin, T. Pugsley, C. Winters, Application of chaos analysis to pressure fluctuation data from a fluidized bed dryer containing pharmaceutical granule, Powder Technology, 142 (2004)

110-120.

[115] K. Clarke, T. Pugsley, G. Hill, Fluidization of moist sawdust in binary particle systems in a gas–solid fluidized bed, Chemical Engineering Science, 60 (2005) 6909-6918.

[116] J. Zhu, Fluidization of fine powders, Granular materials. fundamentals and applications, The Royal Society of Chemistry, (2004) 270-295.

[117] M. Krantz, H. Zhang, J. Zhu, Characterization of powder flow: Static and dynamic testing, Powder Technology, 194 (2009) 239-245.

[118] Z. Gawrzynski, R. Glaser, Drying in a pulsed-fluid bed with relocated gas stream, Drying Technology, 14 (1996) 1121-1172.

[119] A. Akhavan, J.R. van Ommen, J. Nijenhuis, X.S. Wang, M.-O. Coppens, M.J. Rhodes, Improved drying in a pulsation-assisted fluidized bed, Industrial & Engineering Chemistry Research, 48 (2009) 302-309.

[120] P. Zhao, Y. Zhao, Z. Luo, Z. Chen, C. Duan, S. Song, Effect of operating conditions on drying of Chinese lignite in a vibration fluidized bed, Fuel Processing Technology, 128 (2014) 257-264.

[121] R.V. Daleffe, M.C. Ferreira, J.T. Freire, Drying of pastes in vibro-fluidized beds: effects of the amplitude and frequency of vibration, Drying Technology, 23 (2005) 1765-1781.

[122] K.L. Clarke, T. Pugsley, G.A. Hill, Fluidization of moist sawdust in binary particle systems in a gas–solid fluidized bed, Chemical Engineering Science, 60 (2005) 6909-6918.

[123] C. Si, Q. Guo, Fluidization characteristics of binary mixtures of biomass and quartz sand in an acoustic fluidized bed, Industrial & Engineering Chemistry Research, 47 (2008) 9773-9782.

[124] M. Nitz, O.P. Taranto, Drying of beans in a pulsed fluid bed dryer: Drying kinetics, fluid-dynamic study and comparisons with conventional fluidization, Journal of Food Engineering, 80 (2007) 249-256.

[125] D. Jia, O. Cathary, J. Peng, X. Bi, C.J. Lim, S. Sokhansanj, Y. Liu, R. Wang, A. Tsutsumi, Fluidization and drying of biomass particles in a vibrating fluidized bed with pulsed gas flow, Fuel

Processing Technology, 138 (2015) 471-482.

[126] A. Reyes, R. Vega, G. Garcia, Drying sawdust in a pulsed fluidized bed, Drying Technology, 26 (2008) 476-486.

[127] Z. Li, W. Su, Z. Wu, R. Wang, A.S. Mujumdar, Investigation of flow behaviors and bubble characteristics of a pulse fluidized bed via CFD modeling, Drying Technology, 28 (2009) 78-93.

[128] K.L. Harbaum, G. Houghton, Effects of sonic vibrations on the rate of absorption of carbon dioxide in gas bubble-beds, Journal of Applied Chemistry, 12 (1962) 234-240.

[129] Z. Gawrzynski, R. Glaser, T. Kudra, Drying of powdery materials in a pulsed fluid bed dryer, Drying Technology, 17 (1999) 1523-1532.

[130] S. Soponronnarit, S. Prachayawarakorn, W. Rordprapat, A. Nathakaranakule, W. Tia, A superheated-steam fluidized-bed dryer for parboiled rice: Testing of a pilot-scale and mathematical model development, Drying Technology, 24 (2006) 1457-1467.

[131] S.S. Ali, M. Asif, A. Ajbar, Bed collapse behavior of pulsed fluidized beds of nano-powder, Advanced Powder Technology, 25 (2014) 331-337.

[132] T. Miles, T. Miles Jr, Overview of biomass gasification in the USA, Biomass, 18 (1989) 163-168.

[133] M. Simone, F. Barontini, C. Nicolella, L. Tognotti, Gasification of pelletized biomass in a pilot scale downdraft gasifier, Bioresource technology, 116 (2012) 403-412.

[134] Y. Liu, J. Peng, Y. Kansha, M. Ishizuka, A. Tsutsumi, D. Jia, X.T. Bi, C. Lim, S. Sokhansanj, Novel fluidized bed dryer for biomass drying, Fuel Processing Technology, 122 (2014) 170-175.

[135] A. Reyes, P. Moyano, J. Paz, Drying of potato slices in a pulsed fluidized bed, Drying technology, 25 (2007) 581-590.

[136] A. Reyes, N. Herrera, R. Vega, Drying suspensions in a pulsed fluidized bed of inert particles, Drying Technology, 26 (2007) 122-131.

[137] H.K. Bizhaem, H.B. Tabrizi, Experimental study on hydrodynamic characteristics of gas–solid pulsed fluidized bed, Powder Technology, 237 (2013) 14-23.

[138] D. Jia, X. Bi, C.J. Lim, S. Sokhansanj, A. Tsutsumi, Biomass drying in a pulsed fluidized bed without inert bed particles, Fuel, 186 (2016) 270-284.

[139] M. Cavinato, E. Franceschinis, S. Cavallari, N. Realdon, A. Santomaso, Relationship between particle shape and some process variables in high shear wet granulation using binders of different viscosity, Chemical Engineering Journal, 164 (2010) 292-298.

[140] G. Chaplin, T. Pugsley, C. Winters, The S-statistic as an early warning of entrainment in a fluidized bed dryer containing pharmaceutical granule, Powder technology, 149 (2005) 148-156.

[141] H. Khosravi Bizhaem, H. Basirat Tabrizi, Experimental study on hydrodynamic characteristics of gas–solid pulsed fluidized bed, Powder Technology, 237 (2013) 14-23.

[142] A. Motevali, S. Minaei, M.H. Khoshtagaza, Evaluation of energy consumption in different drying methods, Energy Conversion and Management, 52 (2011) 1192-1199.

[143] N. Menshutina, M. Gordienko, A. Voynovskiy, T. Kudra, Dynamic analysis of drying energy consumption, Drying Technology, 22 (2004) 2281-2290.

[144] H. Chen, X. Liu, C. Bishop, B.J. Glasser, Fluidized bed drying of a pharmaceutical powder: a parametric investigation of drying of dibasic calcium phosphate, Drying Technology, 35 (2017) 1602-1618.

[145] M. Taghavivand, Investigations on Drying and Tribocharging Behaviour of Pharmaceutical Powders in a Fluidized Bed Dryer, in: C.o.G.S. University of Saskatchewan, Research (Eds.), 2016.

[146] C. Hii, C. Law, M. Cloke, Modeling using a new thin layer drying model and product quality of cocoa, Journal of Food Engineering, 90 (2009) 191-198.

[147] R. Barati, Application of excel solver for parameter estimation of the nonlinear Muskingum models, KSCE Journal of Civil Engineering, 17 (2013) 1139-1148.

[148] A. Ayensu, Dehydration of food crops using a solar dryer with convective heat flow, Solar Energy, 59 (1997) 121-126.

[149] E.K. Akpinar, Y. Bicer, C. Yildiz, Thin layer drying of red pepper, Journal of Food Engineering, 59 (2003) 99-104.

[150] V.T. Karathanos, V.G. Belessiotis, Application of a thin-layer equation to drying data of fresh and semi-dried fruits, Journal of Agricultural Engineering Research, 74 (1999) 355-361.

[151] O. Yaldiz, C. Ertekin, H.I. Uzun, Mathematical modeling of thin layer solar drying of sultana grapes, Energy, 26 (2001) 457-465.

[152] İ.T. Toğrul, D. Pehlivan, Modelling of thin layer drying kinetics of some fruits under open-air sun drying process, Journal of Food Engineering, 65 (2004) 413-425.

[153] L.R. Verma, R. Bucklin, J. Endan, F. Wratten, Effects of drying air parameters on rice drying models, Transactions of the ASAE, 28 (1985) 296-0301.

[154] A. Midilli, H. Kucuk, Z. Yapar, A new model for single-layer drying, Drying Technology, 20 (2002) 1503-1513.

[155] M. Taghavivand, K. Choi, L. Zhang, Investigation on drying kinetics and tribocharging behaviour of pharmaceutical granules in a fluidized bed dryer, Powder Technology, 316 (2017) 171-180.

[156] G. Chaplin, T. Pugsley, C. Winters, The S-statistic as an early warning of entrainment in a fluidized bed dryer containing pharmaceutical granule, Powder Technology, 149 (2005) 148-156.

[157] L. Dong, Y. Zhao, C. Duan, Z. Luo, B. Zhang, X. Yang, Characteristics of bubble and fine coal separation using active pulsing air dense medium fluidized bed, Powder Technology, 257 (2014) 40-46.

[158] A.K. Nayak, K. Manna, Current developments in orally disintegrating tablet technology, Journal of Pharmaceutical Education and Research, 2 (2011) 21.

[159] H.G. Kristensen, T. Schaefer, Granulation: A review on pharmaceutical wet-granulation, Drug Development and Industrial Pharmacy, 13 (1987) 803-872.

[160] A. Sowinski, L. Miller, P. Mehrani, Investigation of electrostatic charge distribution in gas–solid fluidized beds, Chemical Engineering Science, 65 (2010) 2771-2781.

[161] S. Matsusaka, Control of particle tribocharging, KONA Powder and Particle Journal, 29 (2011) 27-38.

[162] F. Fotovat, X.T. Bi, J.R. Grace, Electrostatics in gas-solid fluidized beds: a review, Chemical Engineering Science, 173 (2017) 303-334.

[163] K. Choi, M. Taghavivand, L. Zhang, Experimental studies on the effect of moisture content and volume resistivity on electrostatic behaviour of pharmaceutical powders, International Journal of Pharmaceutics, 519 (2017) 98-103.

[164] R.G. Rokkam, A. Sowinski, R.O. Fox, P. Mehrani, M.E. Muhle, Computational and experimental study of electrostatics in gas–solid polymerization fluidized beds, Chemical Engineering Science, 92 (2013) 146-156.

[165] W.O. Moughrabiah, J.R. Grace, X.T. Bi, Effects of pressure, temperature, and gas velocity on electrostatics in gas− solid fluidized beds, Industrial & Engineering Chemistry Research, 48 (2009) 320-325.

[166] T.A. Alsmari, J.R. Grace, X.T. Bi, Effects of superficial gas velocity and temperature on entrainment and electrostatics in gas–solid fluidized beds, Chemical Engineering Science, 123 (2015) 49-56.

[167] W.D. Greason, Investigation of a test methodology for triboelectrification, Journal of Electrostatics, 49 (2000) 245-256.

[168] S. Karner, N.A. Urbanetz, The impact of electrostatic charge in pharmaceutical powders with specific focus on inhalation-powders, Journal of Aerosol Science, 42 (2011) 428-445.

[169] D. Boland, D. Geldart, Electrostatic charging in gas fluidised beds, Powder Technology, 5 (1972) 289-297.

[170] V. Rojo, J. Guardiola, A. Vian, A capacitor model to interpret the electric behaviour of fluidized beds. Influence of apparatus geometry, Chemical Engineering Science, 41 (1986) 2171-2181.

[171] G. Hendrickson, Electrostatics and gas phase fluidized bed polymerization reactor wall sheeting, Chemical Engineering Science, 61 (2006) 1041-1064.

[172] Y. Cheng, D.Y.J. Lau, G. Guan, C. Fushimi, A. Tsutsumi, C.-H. Wang, Experimental and

numerical investigations on the electrostatics generation and transport in the downer reactor of a triple-bed combined circulating fluidized bed, Industrial & Engineering Chemistry Research, 51 (2012) 14258-14267.

[173] S. Kim, J. Chen, T. Cheng, A. Gindulyte, J. He, S. He, Q. Li, B.A. Shoemaker, P.A. Thiessen, B. Yu, L. Zaslavsky, J. Zhang, E.E. Bolton, PubChem in 2021: new data content and improved web interfaces, Nucleic Acids Research, 49 (2021) D1388-D1395.

[174] F. Fotovat, T.A. Alsmari, J.R. Grace, X.T. Bi, The relationship between fluidized bed electrostatics and entrainment, Powder Technology, 316 (2017) 157-165.

[175] T. Poppe, R. Schräpler, Further experiments on collisional tribocharging of cosmic grains, A&A, 438 (2005) 1-9.

[176] W.O. Moughrabiah, J.R. Grace, X.T. Bi, Effects of pressure, temperature, and gas velocity on electrostatics in gas−solid fluidized beds, Industrial & Engineering Chemistry Research, 48 (2009) 320-325.

[177] P.M. Ireland, Triboelectrification of particulate flows on surfaces: part ii—mechanisms and models, Powder Technology, 198 (2010) 199-210.

[178] L. Laakso, S. Gagné, T. Petäjä, A. Hirsikko, P. Aalto, M. Kulmala, V.-M. Kerminen, Detecting charging state of ultra-fine particles: instrumental development and ambient measurements, Atmospheric Chemistry and Physics, 7 (2007) 1333-1345.

[179] S. Naik, B. Hancock, Y. Abramov, W. Yu, M. Rowland, Z. Huang, B. Chaudhuri, Quantification of tribocharging of pharmaceutical powders in v-blenders: experiments, multiscale modeling, and simulations, Journal of Pharmaceutical Sciences, 105 (2016) 1467-1477.

[180] D. Verkoeijen, G.M.H. Meesters, P.H.W. Vercoulen, B. Scarlett, Determining granule strength as a function of moisture content, Powder Technology, 124 (2002) 195-200.

[181] M.E. Aulton, K.M. Taylor, Aulton's pharmaceutics e-book: the design and manufacture of medicines, Elsevier Health Sciences, 2017.

[182] P. Mohanachandran, P. Sindhumol, T. Kiran, Superdisintegrants: an overview, International

Journal of Pharmaceutical Sciences review and research, 6 (2011) 105-109.

[183] W. Senadeera, Minimum fluidization velocity of food materials: effect of moisture and shape, Chemical Product and Process Modeling, 4 (2009) 1-19.

[184] A. Kahn, Fermi level, work function and vacuum level, Materials Horizons, 3 (2016) 7-10.

[185] J. Wong, P.C.L. Kwok, H.-K. Chan, Electrostatics in pharmaceutical solids, Chemical Engineering Science, 125 (2015) 225-237.

[186] S. Naik, S. Sarkar, B. Hancock, M. Rowland, Y. Abramov, W. Yu, B. Chaudhuri, An experimental and numerical modeling study of tribocharging in pharmaceutical granular mixtures, Powder Technology, 297 (2016) 211-219.

[187] S. Karner, N. Anne Urbanetz, The impact of electrostatic charge in pharmaceutical powders with specific focus on inhalation-powders, Journal of Aerosol Science, 42 (2011) 428-445.

[188] D.A. Engers, M.N. Fricke, A.W. Newman, K.R. Morris, Triboelectric charging and dielectric properties of pharmaceutically relevant mixtures, Journal of Electrostatics, 65 (2007) 571-581.

APPENDICES

Appendix A. Supplementary granulation experimental results

The following content has been published in International Journal of Pharmaceutics. 2019; 572. https://doi.org/10.1016/j.ijpharm.2019.118797

A1. Dynamic granulation process of LMH powders

The dynamic wetting and nucleation process of LMH powders is shown in Figure A.1. This granulation process follows the spreading granule formation mechanism [20]. It includes three periods: impaction, spreading, and penetration. When the liquid droplet impacts the powder bed surface, the droplet rebounds and distorts within 50 ms (see Figures A.1a and A. 1b). Afterward, LMH powders attach to the external surface of the liquid droplet and move upward (see Figures A.1c and A. 1d). Two layers are observed from the granule beneath the powder bed at 125 ms, as shown in Figure A.1d. The inner layer with a darker colour is the core of the granule, and the outer layer represents the water-penetrating layer. The water-penetrating layer has lower moisture content and was formed during penetration and spreading stages. The inner layer has a higher moisture content than the outer layer. High moisture can form more liquid films and enhance adhesion forces between the powders in granules. The strength of the granule increases with an increase in moisture content when the moisture content is lower than 20% [180]. The internal structure of the granule core usually has a higher strength than the water-penetrating layer [181].

The LMH granule size is shown in Figure A.2. The droplet diameter, d_d, increases when the kinetic energy releases, as shown in Figure A.2a. The distortion process lasts approximately 200 ms after the droplet contacts the powder bed surface. When d_d reaches its maximum, the gravity and capillary forces drive the growth of the granule beneath the bed surface from 200 ms to 1 s, as indicated in Figures A.1e-g. In the meantime, the droplet above the bed surface diminishes gradually. After 1 s, the spreading process becomes almost stationary, as illustrated in Figure A.1h. When the droplet volume is 15 μL, the impaction period (0.2 s) is more extended than that of a droplet of 10 μL, which is 0.1 s. The spreading period with a 10-μL droplet is shorter than with a

15-μL droplet. This is due to the lower kinetic energy for a smaller droplet.

As shown in Figure A.2b, the penetration time of water is within 1 s. This can be explained by the hydrophilic properties of LMH powders (contact angle of 79.6°). It can be seen in Figure A.2b that the water droplet of 15 μL disappears within 0.6 s, faster compared to that for the 10 μL water droplet (0.8 s). This is likely due to the higher kinetic energy with a larger droplet.

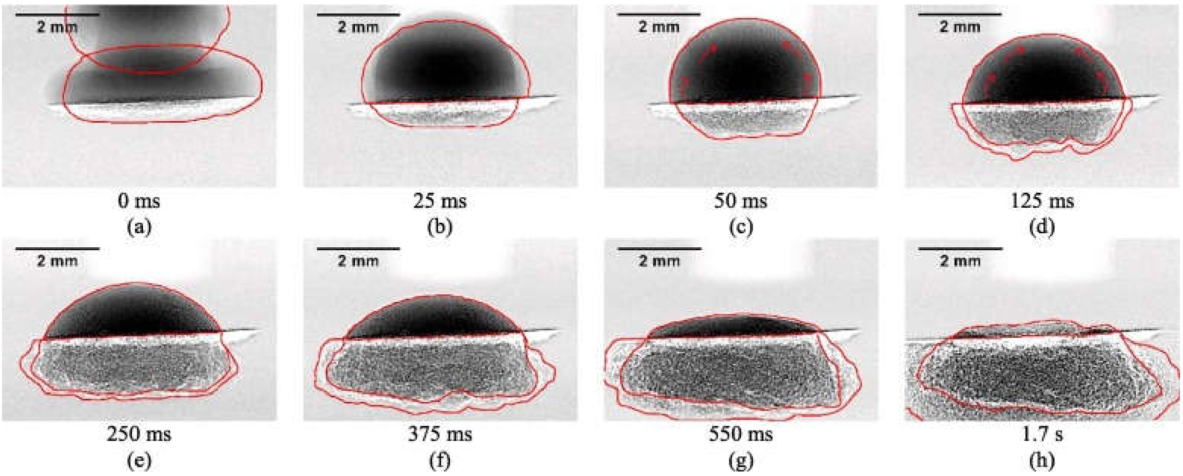

Figure A.1 Time sequence X-ray images of dynamic wetting and nucleation process of LMH powders.

Because the spreading water exceeds the field of view of the camera, the granule size was not measured after 0.9 s in Figure A.2c. The water spreading and penetration processes are slower than the liquid droplet collapsing, as shown in Figure A.2c. The LMH powders offer high cohesive properties, and the final LMH granule was firmly embedded into the powder layer. The estimated Bo_g^* for the LMH powders with water is 252.8, which is located in the spreading region [79].

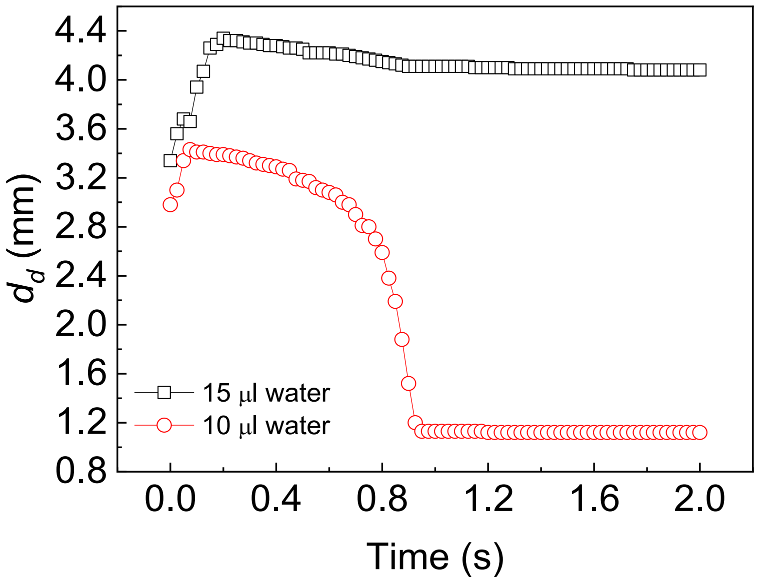
d_d (mm)
4.4
4.0
3.6
3.2
2.8
2.4
2.0
1.6
1.2
0.8
0.0
0.4
0.8
1.2
1.6
2.0
Time (s)
15 μl water
10 μl water

(a)

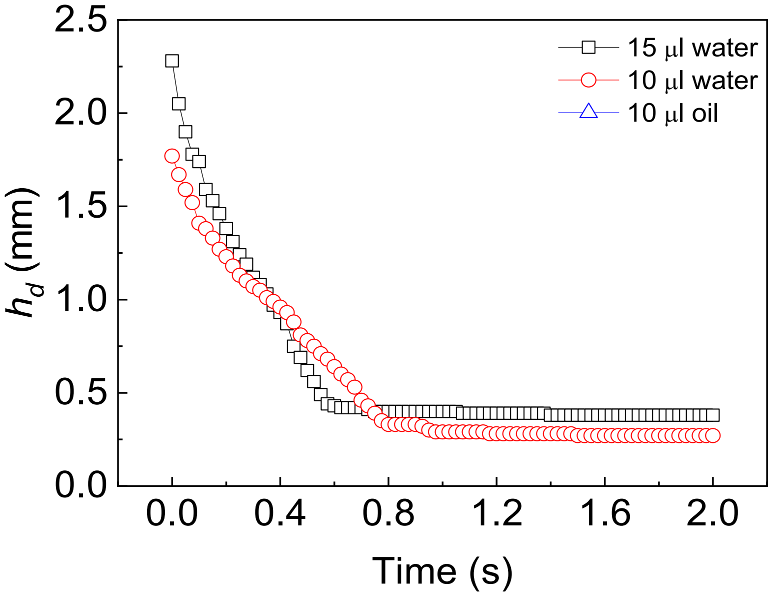
h_d (mm)
2.5
2.0
1.5
1.0
0.5
0.0
0.0
0.4
0.8
1.2
1.6
2.0
Time (s)
15 μl water
10 μl water
10 μl oil

(b)

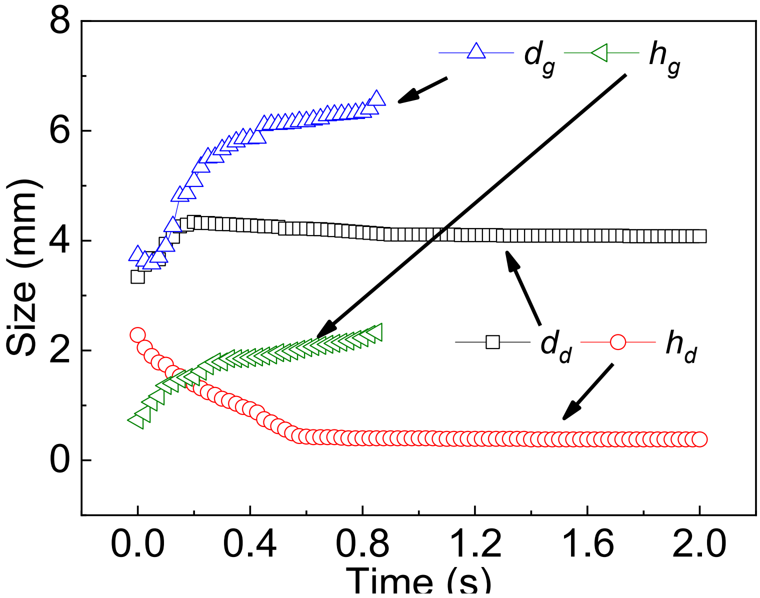

(c)

Figure A.2 Size of the LMH granule with water as liquid binder: (a) diameter of the droplet, (b) height of the droplet, and (c) granule size.

A2. Dynamic granulation process of CCS powders

CCS is mainly used as a disintegrant in pharmaceutical formulations. The wetting and nucleation process of CCS powders is illustrated in Figure A.3. This process consists of three phases: impaction, attaching, and swelling. The impaction period is similar to that observed from the LMH powder bed (see section 3.3.1). The two shadows in Figure A.3a represent the movement of the droplet during the scan interval of 0.25 s. However, once the liquid droplet becomes relatively stable, fine powders move upward through the droplet surface and form a nucleus (see Figures A.3d and A.3e). When the powders cover the outer surface of the droplet, the CCS powders move inward, and the top of the droplet collapses (see Figure A.3f). The CCS granule then swells (see Figures A.3g and A.3h). During swelling, the shape of the granule changes from oval to a central sinking apple shape. The central sinking may be attributed to the uneven moisture distribution in the granule. The surface of the granule, covered with CCS powders, forms a shell. This prevents the water inside the granule from spreading out because of the low water solubility and extra high hydroscopicity. The swelling of CCS powders changes the shape of the granule and forms the apple-shaped CCS granule.

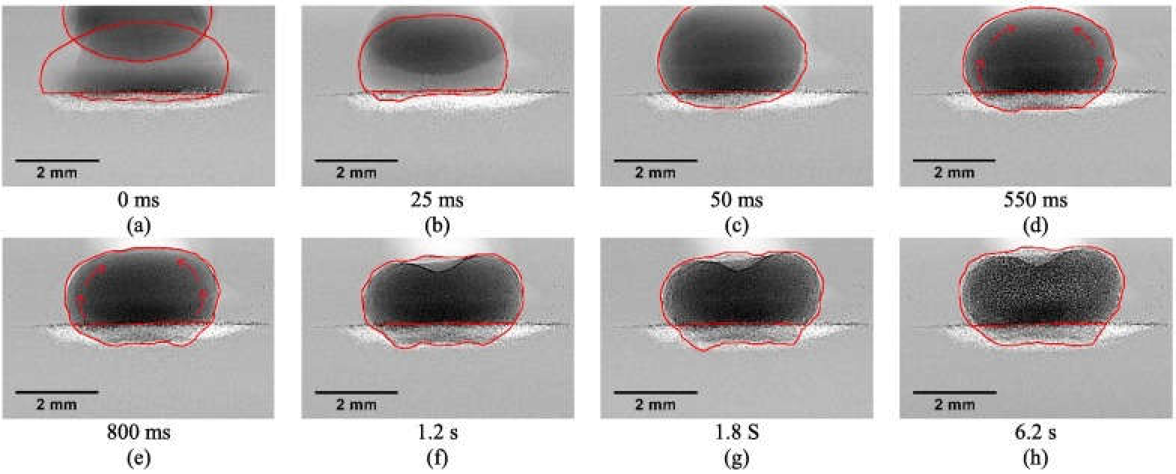

0 ms (a) 25 ms (b) 50 ms (c) 550 ms (d)

800 ms (e) 1.2 s (f) 1.8 S (g) 6.2 s (h)

Figure A.3 Time sequence X-ray images of dynamic wetting and nucleation process of CCS powders.

The Bo_g^* of the CCS granule with water as the liquid binder is 236.1, which is similar to the LMH granule (Bo_g^*=252.8), but the wetting and nucleation process is different. According to the Bo_g^*'s, both of these powders should fall in the spreading regime [79]. However, this regime map does not capture the intricacies of the CCS granule formation mechanism. CCS powders have internally cross-linked structures and low water solubility, which ensures extra high hydroscopicity [182]. The CCS powders attached to the droplet surface form a shell and prevent the water inside the granule from spreading out to the bed layer.

A3. Dynamic granulation process of MCC powders

Figure A.4 illustrates the wetting and nucleation process of MCC powders. The highly hydrophilic nature (contact angle $\theta=49.60^0 \pm 0.20^0$) and large particle size (d_{50}=128 μm) of MCC powders result in spreading mechanism, and the shortest penetration time (200 ms) among all of the powders investigated in this work. The water droplet disappears immediately (within 25 ms) after it impacts the bed surface, as seen in Figures A.4a and A. 4b. However, the penetration in the bed and the swelling process continue for a few seconds, as illustrated in subsequent Figures A.4b to A.4h. The bed surface slightly moves up during the swelling process. Comparing the final granule in Figure 3.3m, the plate shape of the MCC granule and high *VAR* (2.38) indicate that the liquid water mainly moves horizontally in the powder bed.

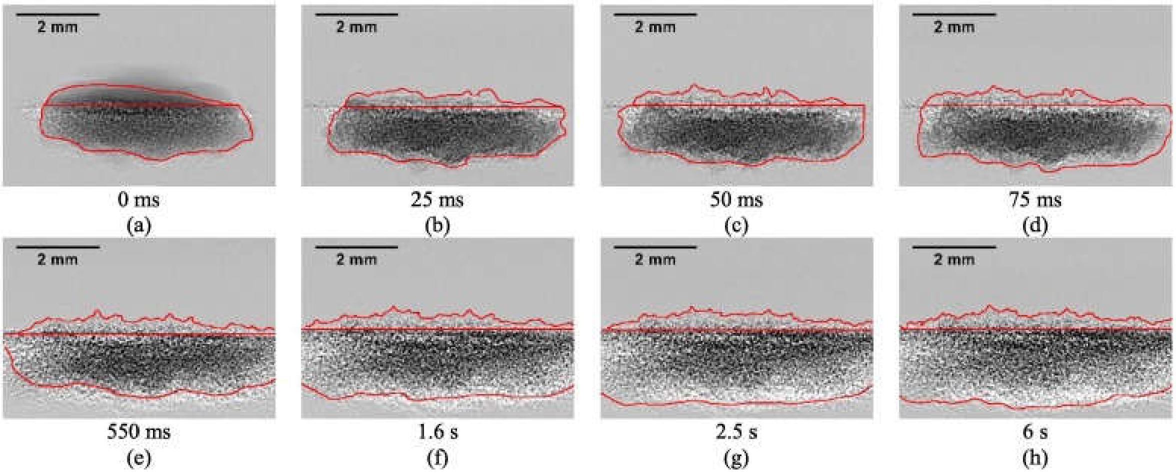

Figure A.4 Time sequence X-ray images of dynamic wetting and nucleation process of MCC powders.

A4. Dynamic granulation process of APAP powders

Figure A.5 shows the dynamic granulation process of APAP powders, which contains three phases: impaction, attaching, and penetration. The impaction and attaching phases are very similar to that of the LMH powders (see Appendix A.1). This can be explained by the similar contact angle and particle size, as indicated in Tables 4.1 and 4.2. Figure A.5g shows that when the APAP powders move upward on the droplet surface, the droplet above the bed surface remains stable for 1 s (see Figure A.6). Then the water beneath the bed surface starts spreading, and the droplet collapses (see Figures A.5g and A.5h). The attaching results from the relative hydrophobicity (θ=82.9°) and the small particle size of APAP powders. The small particle size makes it easier to attach to the droplet surface and form a shell, preventing continuous contact between the water and the powder bed. This resulted in a long penetration time for the APAP granulation process (about 3.5 s). The time range of each phase can be seen in Figure A.6. Here, the impaction phase (0 to 0.50 ms) can be seen from the sharp decrease of d_d and h_d in the initial period. Figure A.6 shows that the d_d, h_d, d_g, and h_g remain stable from 0.50 ms to 1s, which represents the attaching phase. Then, d_d, d_g and h_g increase, and d_d decrease from 1 to 3.5 s during the penetration phase.

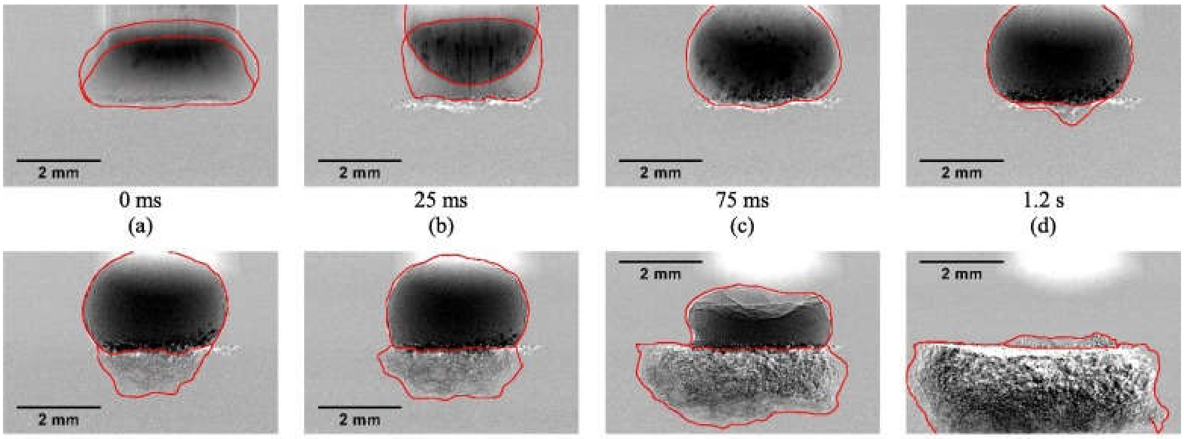

0 ms (a) 25 ms (b) 75 ms (c) 1.2 s (d)

1.4 s (e) 1.5 s (f) 2.1 s (g) 3.4 s (h)

Figure A.5 Time sequence X-ray images of dynamic wetting and nucleation process of APAP powders.

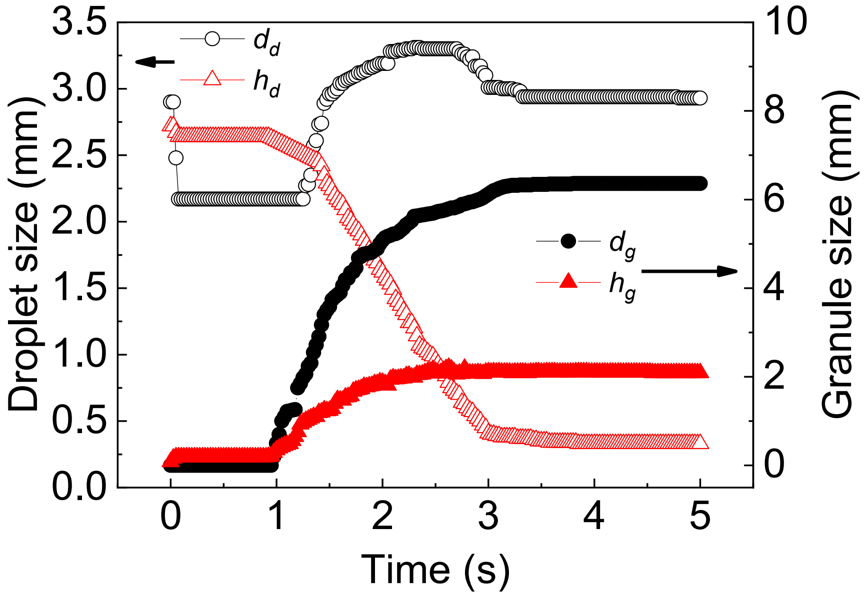

Figure A.6 Size of the APAP granule with water as the liquid binder.

A5. Dynamic granulation process of IBU powders

Figure A.7 shows images captured during the dynamic granulation process of the IBU powders. This process is a typical spreading mechanism granulation process. The granulation process of IBU powders includes three phases: impaction, penetration, and spreading. The particle size of IBU powders is the largest one in this study (d_{50}=195 μm), and the needle-like shape of IBU powders results in low sphericity. Due to the lowest modified Bond number (Bo_g^*=16.8), the impaction phase (see Figures A.7a-b) and penetration time (1 s) are shorter (see Figures A.7c-d) compared to other powders.

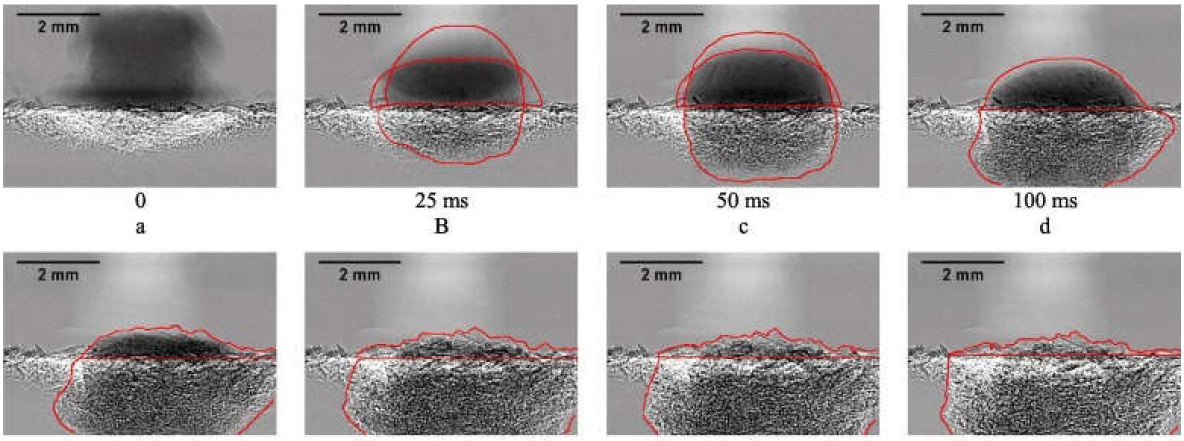

0
a

25 ms
B

50 ms
c

100 ms
d

150 ms
e

500 ms
F

1 s
g

2.8 s
h

Figure A.7 Time sequence X-ray images of dynamic wetting and nucleation process of IBU powders.

A6. Dynamic granulation process of pharmaceutical powder mixtures

The granulation process of pharmaceutical powder mixtures was studied to simulate the actual industrial formulations in the pharmaceutical industry. Two formulations, as shown in Tables 3.1 and 3.2, with different API loadings, were investigated in this work. The images obtained from the dynamic process of Formulation 1 are shown in Figure A.8. The entire granulation process can be described in three steps: impaction, spreading, and swelling. During the impaction stage, powders attached to the surface of the droplet, as shown in Figures A.8a-b. In Figures A.8c-d, it is observed that the attached powders were moving downward, compared with Figure A.8b. This demonstrates the penetration of water into the bed layer. Comparing Figures A.8e-h, the water penetrates further under the bed surface.

The influence of API loading on the size is presented in Figure A.9. The loading of the APAP in the mixture has shown a significant impact on the granulation process. When the content of APAP is greater than 15%, d_d increases with the APAP concentration, as shown in Figure A.9a. If APAP is smaller than 15%, d_d decreases with an increase in the APAP concentration. In the literature, similar granulation transition results were reported by Gao et al. [81].

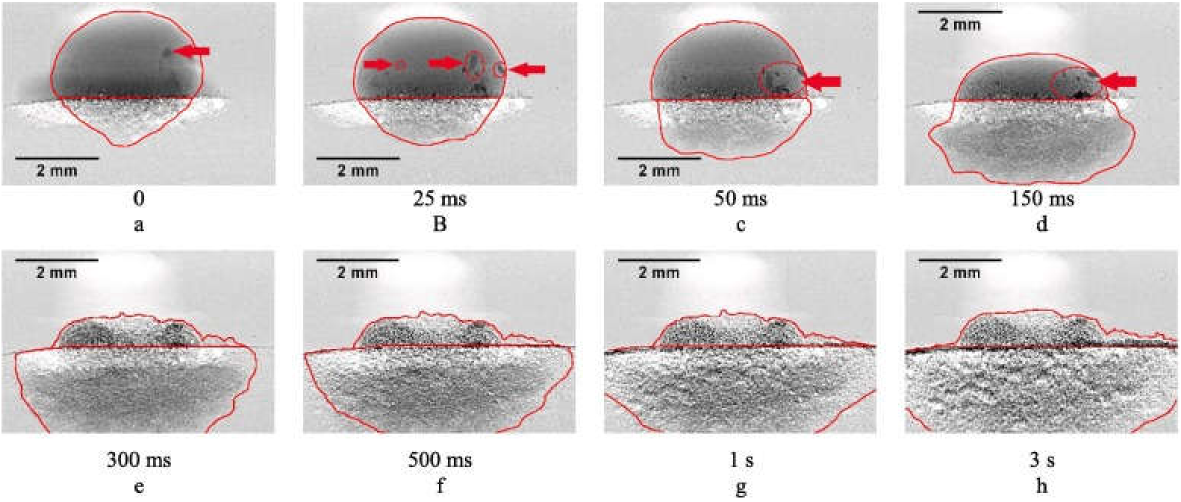

Figure A.8 Time sequence X-ray images of dynamic wetting and nucleation process of formulation 1 (15% APAP) powders.

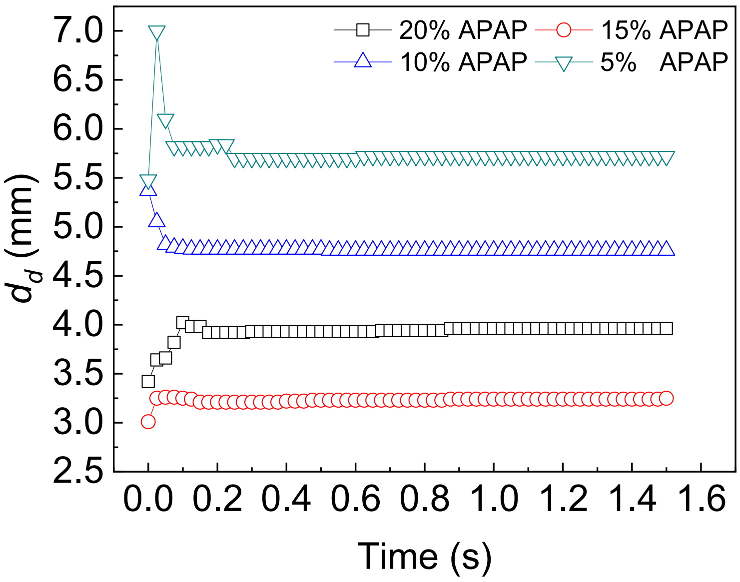

(a)

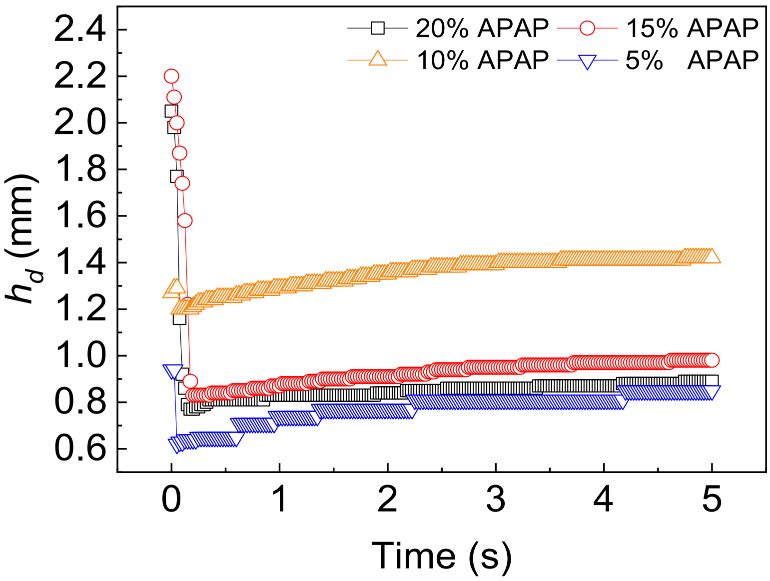

(b)

Figure A.9 Size of pharmaceutical powder mixture granules: (a) diameter of the droplet, and (b) height of the droplet.

Another set of formulations with IBU as the API was investigated. The formulation (formulation 2) of the mixture is shown in Table 3.2. The dynamic granulation process of formulation 2 is very similar to that of formulation 1 (see Table 3.1), as shown in Figure A.8. As illustrated in Figure A.10, the IBU loading in the pharmaceutical mixtures also shows an impact on the dynamic granulation process. Increasing the IBU concentration results in a longer spreading time.

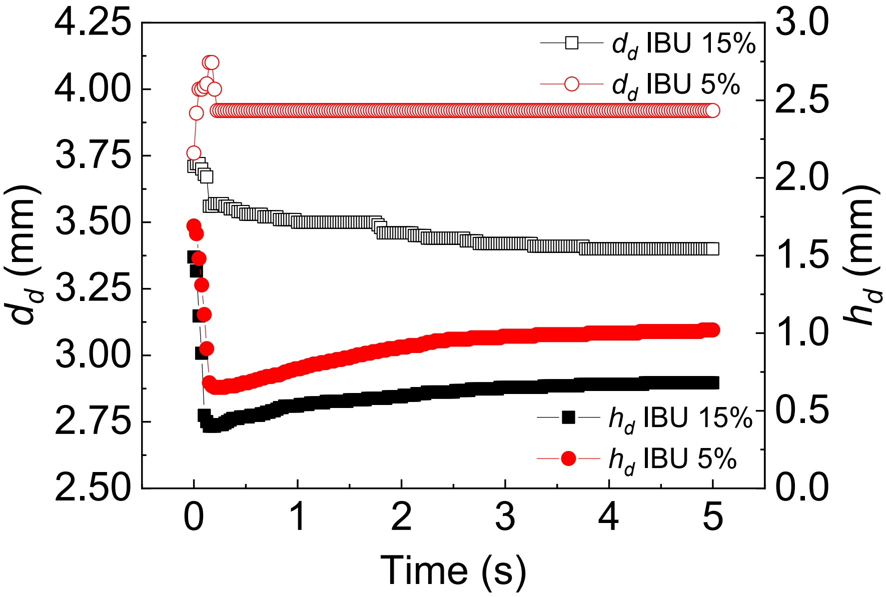

Figure A.10 Size of pharmaceutical powder mixture granule.

Appendix B. Minimum fluidization velocity of pharmaceutical granules

The minimum fluidization velocity is an important parameter, which is defined as the minimum superficial gas velocity at which the particles become completely fluidized. In a conventional fluidized bed, the minimum fluidization velocity is measured by monitoring the pressure drop across the bed when gradually decreasing (or increasing) the superficial gas velocity. The pressure drop increases when increasing the superficial gas velocity at the initial period. The drag force and buoyancy force equals the weight of the bed layer at the minimum fluidization velocity. The pressure drop keeps constant when the superficial gas velocity is higher than the minimum fluidization velocity.

The minimum fluidization velocity is a function of the moisture content. The pharmaceutical granules with high moisture content usually have high minimum fluidization velocity [183]. The minimum fluidization velocity of the pharmaceutical granules decreases during the course of drying as the granules get dried. Therefore, the minimum fluidization velocity was measured with the granules with the moisture content of 5, 13, 22, and 31 wb %.

The bed pressure drop is periodically oscillating in the pulsed fluidized bed dryer. It's challenging to determine the minimum fluidization velocity directly by plotting pressure drop against superficial gas velocity. Thus, the experiments were conducted with continuous airflow. The minimum fluidization velocity of the pharmaceutical granules with the moisture content of 5, 13, 22, and 31 wb % were 0.13, 0.18, 0.26, 0.44 m/s, respectively, as shown in Figure B.1 An average value of 0.25 m/s was taken as the minimum fluidization velocity.

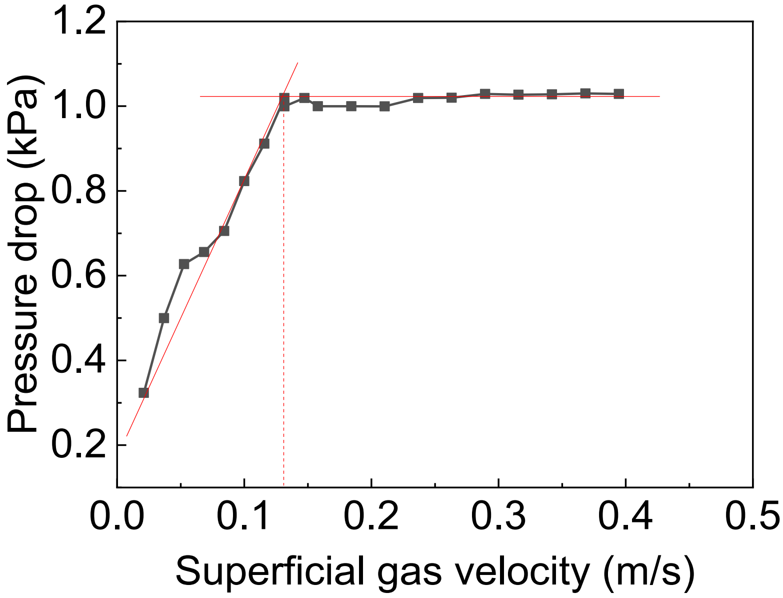
1.2
1.0
0.8
0.6
0.4
0.2
Pressure drop (kPa)
0.0
0.1
0.2
0.3
0.4
0.5
Superficial gas velocity (m/s)

(a)

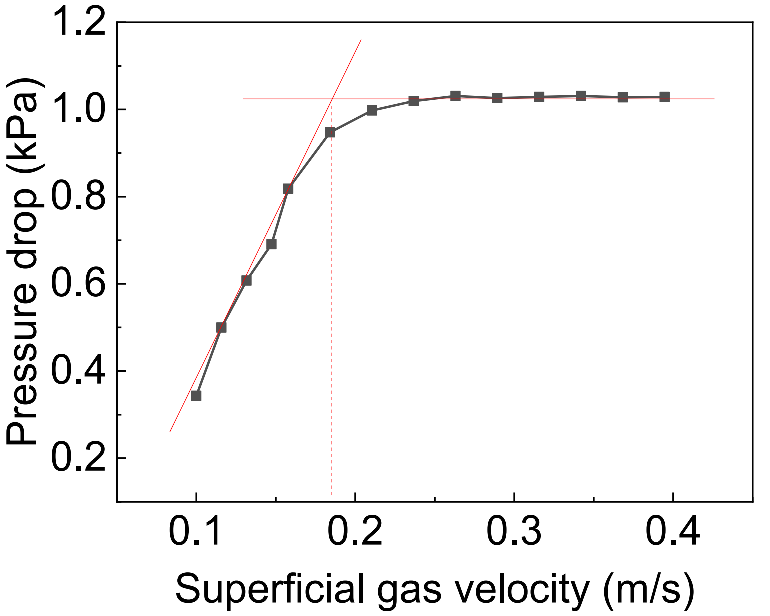
1.2
1.0
0.8
0.6
0.4
0.2
Pressure drop (kPa)
0.1
0.2
0.3
0.4
Superficial gas velocity (m/s)

(b)

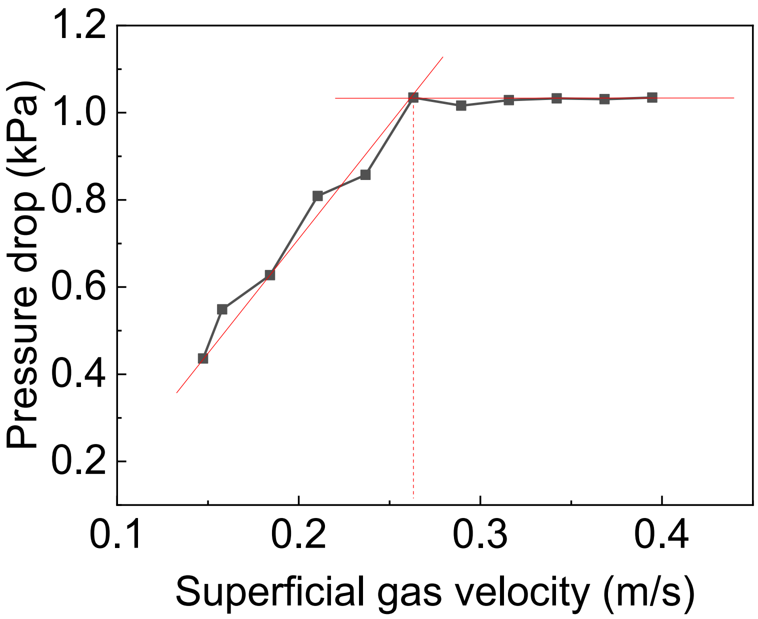

(c)

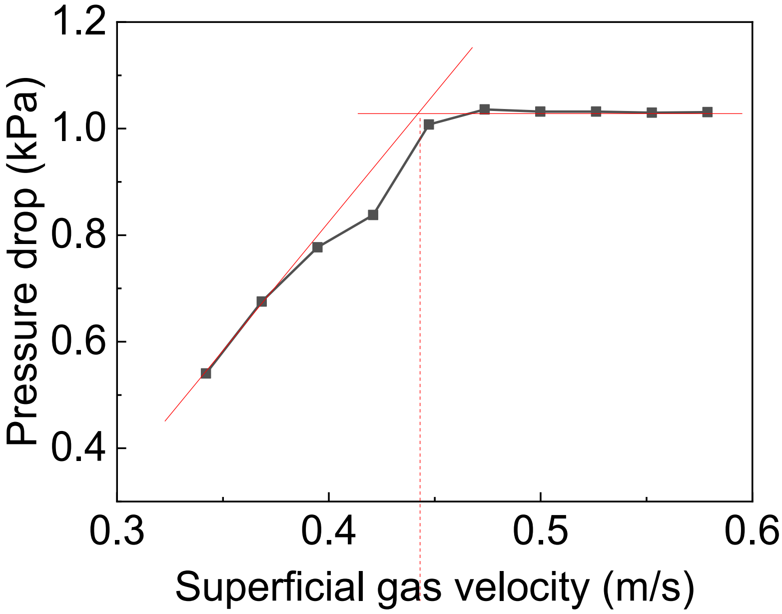

(d)

Figure B.1 Pressure drop in the fluidized bed of granules as a function of superficial gas velocity

(a) *MR*=5 wb %, (b) *MR*=13 wb %, (c) *MR*=22 wb %,(d) *MR*=31 wb %.

Appendix C. Work function of pharmaceutical powders

The work function, as known as ionization potential, is defined as the minimum energy needed to remove an electron from a solid to a point in the vacuum immediately outside the solid surface [184]. The work functions of pharmaceutical powders were measured with a photoemission yield spectroscopy in the air (AC-5, RKI Instruments, Japan). The surface analyzer is equipped with an ultraviolet lamp. The ultraviolet lamp can generate ultraviolet rays from low energy level to high energy level. The scanned materials can emit photoelectrons when the energy level is higher than the excitation energy.

The photoelectron output was recorded and plotted in a rectangular system with the horizontal axis as the ultraviolet energy level was applied. The vertical axis is the standardized photoelectron yield ratio. The work function can be calculated as a line with a specific slope of degree. The work function measurement was conducted once for each type of pharmaceutical powders.

The work function can be determined with the method discussed above. However, this high equipment cost limits its wide applications for measuring the work function. A newly developed cyclone tribocharger can be used to estimate the relative work function of the powders by continuously rubbing against another material with work function already known. The tribocharger consists of a cylindrical vessel connected to a cyclone, as shown in Figure C.1.

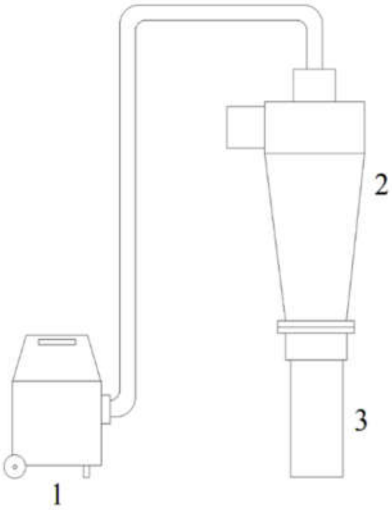

Figure C.1 Turbulent tribocharger. (1) air vacuum pump, (2) cyclone, (3) cylindrical container.

An air vacuum pump was connected to the top of the cyclone, which can provide a vortex of airflow in the cyclone and cylindrical containers made of different materials (copper, PTFE (polytetrafluoroethylene), and PMMA (polymethylmethacrylate), as shown in Figure C.2. Cooper is the metal material used in Faraday cup. PMMA is used to build the product bowl of fluidized bed dryer. Thus, these three types of material were used to relative work function measurement. The powders were loaded into the containers. The inner diameters of copper, PMMA, and PTFE containers are 6.3, 6.3, 5.7 cm, respectively, while the corresponding inner heights are 21.6, 21.6, and 20.4 cm. The air velocity at the inlet of the cyclone was measured by an anemometer (HHF81, OMEGA, US), and the velocity was maintained at 10.2 m/s. The total charge of granules was measured by a Faraday cup connected to an electrometer (6514, Keithley, USA). The wight of the powder sample were determined with a balance (ME4002TE, Mettler Toledo, USA). The specific charge, which is defined as the charge value per unit weight of sample.

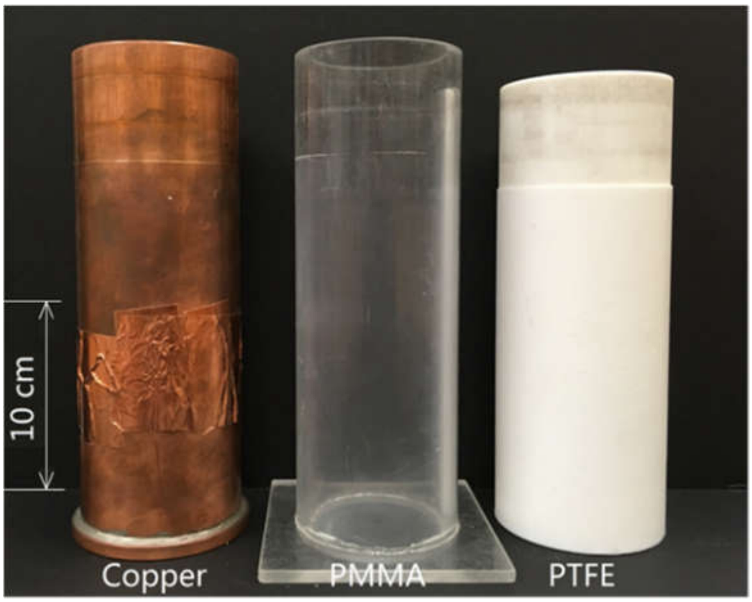

Figure C.2 Cylindrical containers made of copper, PMMA, and PTFE.

Tribocharging behaviour was investigated under different operating parameters, including particle-wall contact time, particle loading mass, and different contact surfaces. The particle-wall contact time is defined as the operation time of the air vacuum pump. The pharmaceutical particles used in the study were made based on a typical placebo pharmaceutical formulation containing lactose monohydrate (LMH), microcrystalline cellulose (MCC), hydroxypropyl methylcellulose (HPMC), and croscarmellose sodium (CCS). The compositions and particle sizes are detailed in Table 6.3.

The work function is defined as the minimum energy needed to remove an electron from a solid surface to a point in infinity relative to the surface yet not far away as to be affected by the ambient electric field [185]. The standardized photoelectron yield ratio at the energy range from 3.4 to 6.2eV of the pharmaceutical powder is shown in Figure C.3. The excitation energy can be determined by the two red lines, as shown in this figure. The APAP powder has the highest work function, 5.88eV, as displayed in Figure C.3b, which means when contacting with other pharmaceutical powders, APAP powder is less likely to lose electrons. Therefore, APAP powders are more likely to gather negative charge than other pharmaceutical powders investigated in this work.

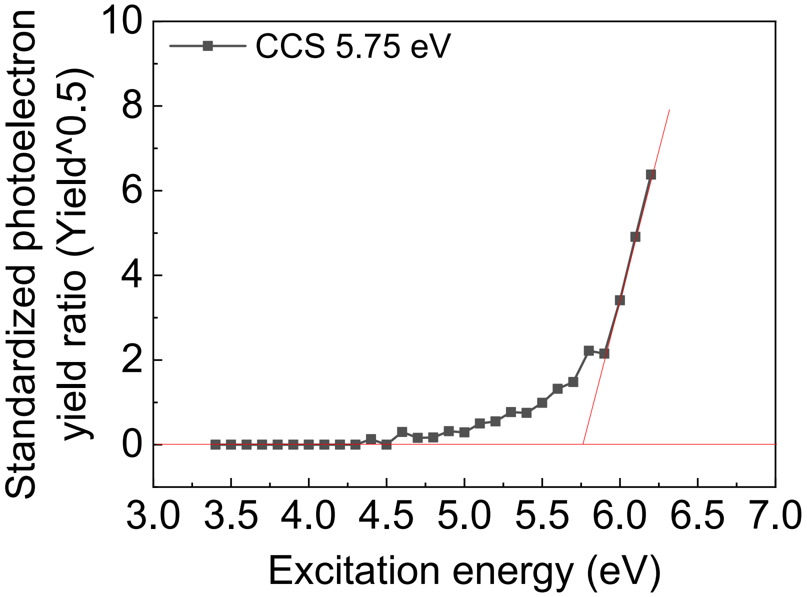

(a)

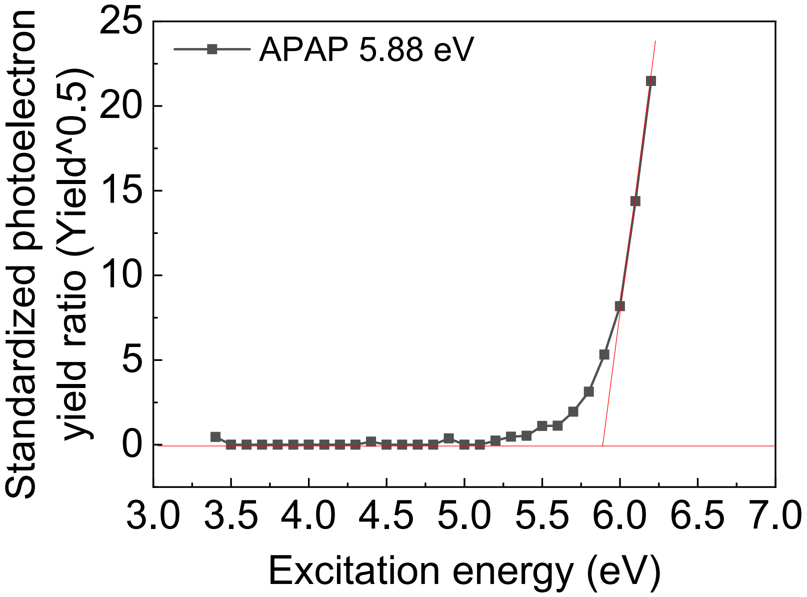

(b)

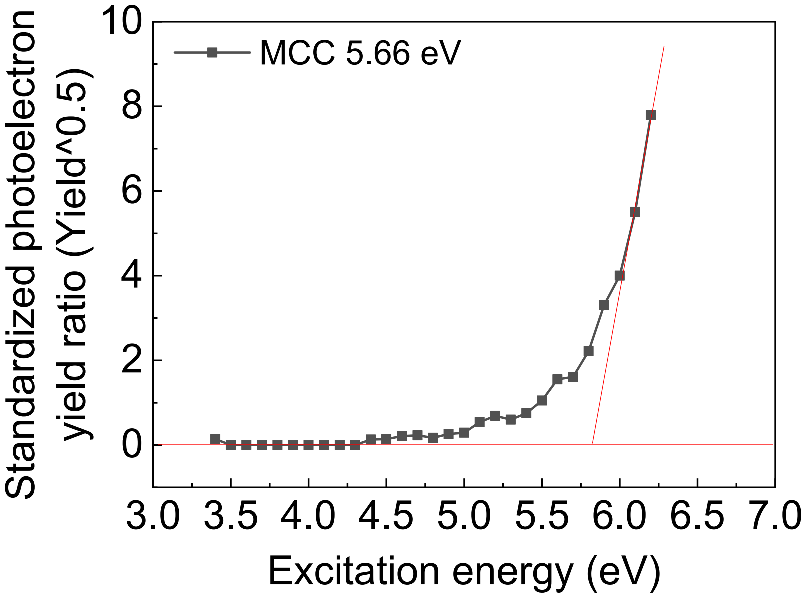
MCC 5.66 eV
Standardized photoelectron yield ratio (Yield^0.5)
Excitation energy (eV)
10
8
6
4
2
0
3.0
3.5
4.0
4.5
5.0
5.5
6.0
6.5
7.0

(c)

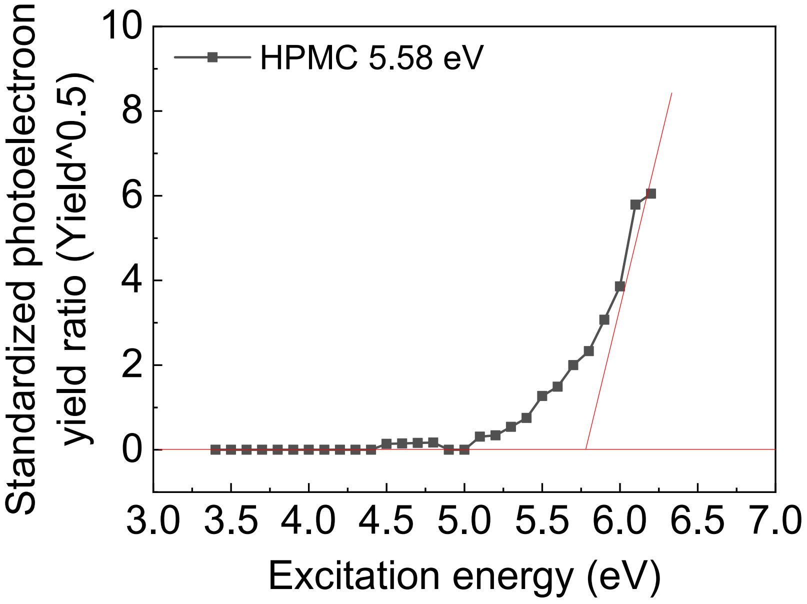
HPMC 5.58 eV
Standardized photoelectroon yield ratio (Yield^0.5)
Excitation energy (eV)
10
8
6
4
2
0
3.0
3.5
4.0
4.5
5.0
5.5
6.0
6.5
7.0

(d)

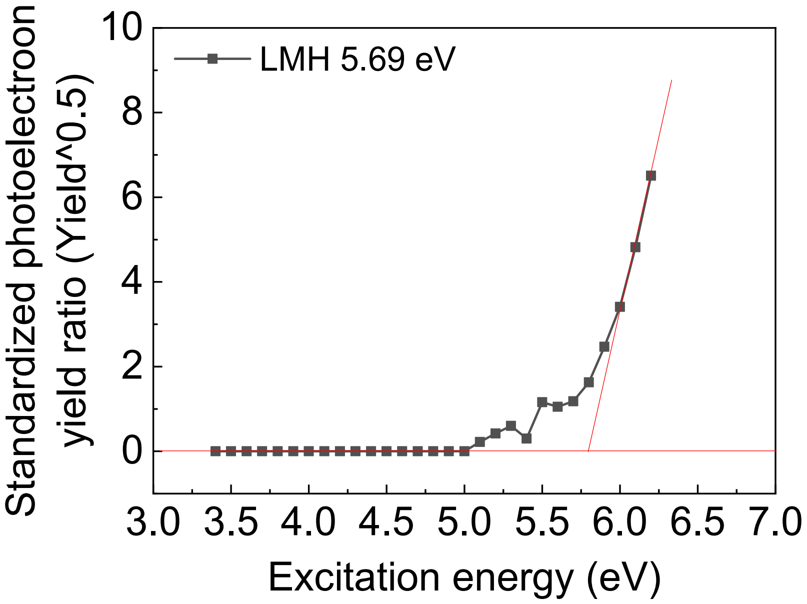

(e)

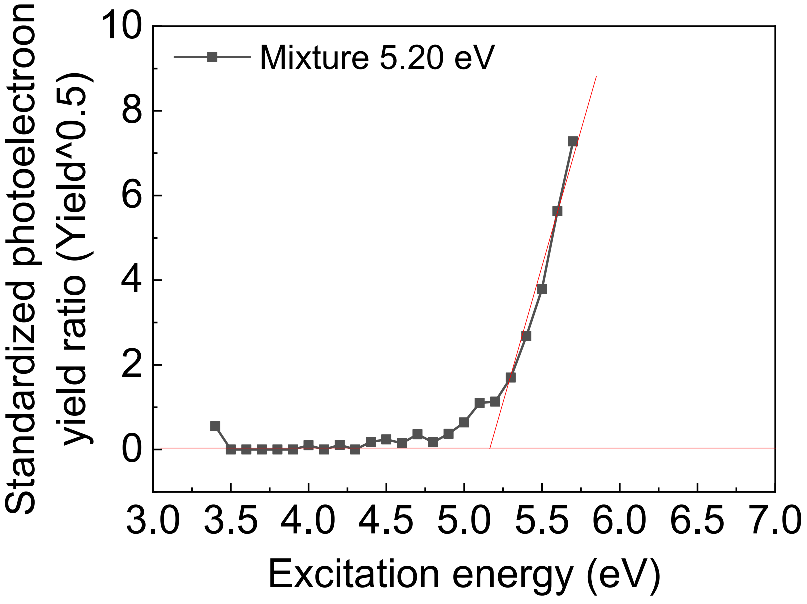

(f)

Figure C.3 Work function of the pharmaceutical powders (a) CCS, (b) APAP, (c) MCC, (d) HPMC, (e) LMH, (f) placebo mixture.

The work function of the pharmaceutical powders is shown in Table C.1 It was found that the pharmaceutical powder mixture has the lowest work function, 5.20 eV. This is consistent with the tribocharging study using binary mixture [186]. Compared with using a single component, the pharmaceutical mixture can gain charge more easily due to the enhanced charge mitigation between particles. The geometrical arrangements of particles within a mixture may also contribute to the change of overall charge behaviour [187, 188]. These factors lead to the lower work function of the pharmaceutical mixture compared with individual components.

Table C.1 Work function of the pharmaceutical powders

Component	Work function (eV)
CCS	5.75
APAP	5.88
MCC	5.66
HPMC	5.58
LMH	5.69
Pharmaceutical granules	5.20

The influence of the operating time on tribocharging behaviour in the copper container is shown in Figure C.4. The copper container was electrically grounded during the test. In general, the negative charge was observed when the granules were contacted with the copper container. The work function of copper is 4.53-5.10 eV [43], which is lower than that of the pharmaceutical powders used. When in contact with the cooper wall, the electrons are transferred from the cooper wall to pharmaceutical powders. Thus, pharmaceutical powders can carry a negative charge.

The results show that pharmaceutical placebo granules tend to accumulate charge gradually at the initial contacting period with the wall. Then, the charge accumulation rate of particles decreased after 120 s. The negative specific charge on particles continued to decrease after 120 s.

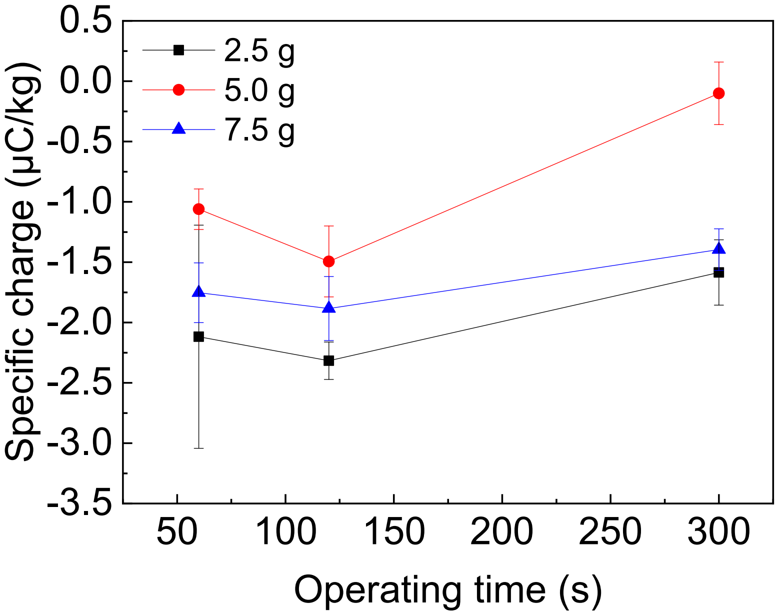

Figure C.4 Effect of operating time on specific charge in the copper container (*T*=23.6℃, *RH*=10.6%).

The influence of the granule loading weight is shown in Figure C.5. In general, the specific charge decreases with increasing the particle loading weight regardless of the polarity of the specific charge, as particle-wall contacts frequency per unit mass decreases with increasing the particle loading mass. The specific charge resulted from contacts between pharmaceutical granules, and the copper wall is lower than that measured with the PTFE and PMMA walls. In general, the granules were negatively charged when copper was used as the contact surface, while granules were positively charged with the contact surfaces of PTFE and PMMA. This result relates to the work functions (or ionization potential) on each material and can be used in creating an assumption such as the triboelectric series. The work functions of PTFE, PMMA, and copper are 5.75 eV, 4.68 eV, and 4.53-5.10 eV, respectively [43]. This implied that the work function of pharmaceutical granules without API (placebo) should be within 4.53-4.68 eV.

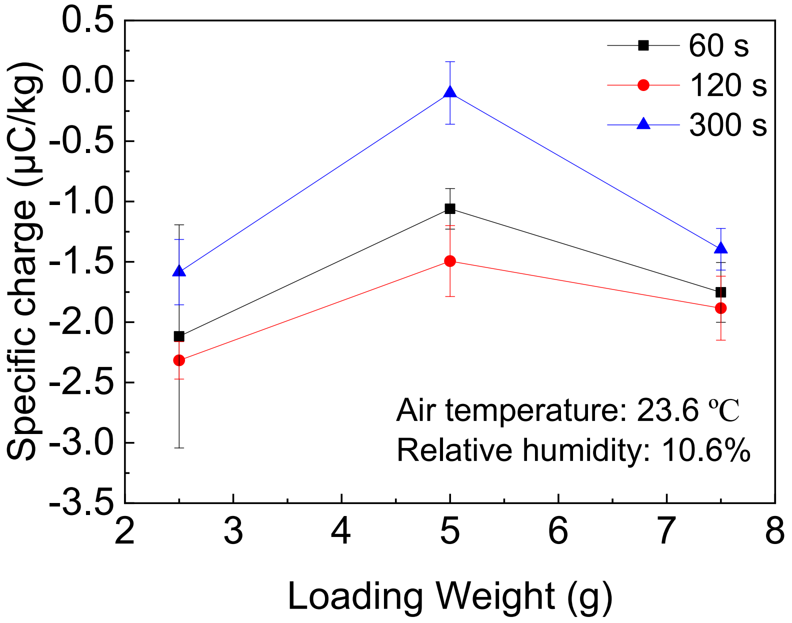
0.5
0.0
-0.5
-1.0
-1.5
-2.0
-2.5
-3.0
-3.5
Specific charge (μC/kg)
2
3
4
5
6
7
8
Loading Weight (g)
60 s
120 s
300 s
Air temperature: 23.6 ºC
Relative humidity: 10.6%

(a)

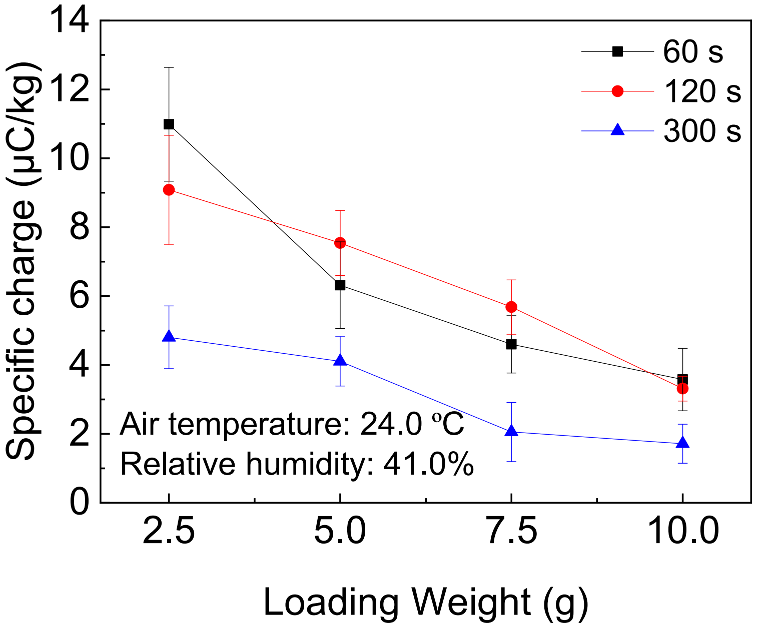
14
12
10
8
6
4
2
0
Specific charge (μC/kg)
2.5
5.0
7.5
10.0
Loading Weight (g)
60 s
120 s
300 s
Air temperature: 24.0 ºC
Relative humidity: 41.0%

(b)

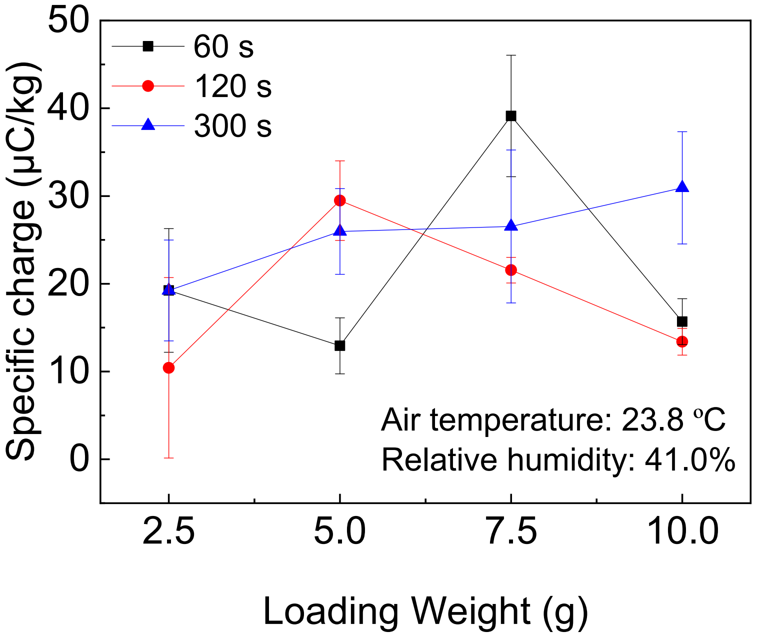

(c)

Figure C.5 Influence of granule loading weight on specific charge in different containers (a) copper (b) PMMA (c) PTFE.